

Acknowledgements

We, of Group Design Project 45, would like to acknowledge and express our gratitude to Dr. Lasagna and Professor Shrimpton for their guidance and advice as project supervisors. We would also like to express gratitude to Mr. Kevin Smith for help with advice regarding the prototype manufacture and Dr. Tim Woolman for his advice on design for manufacture. Moreover, we also appreciate the help with setting up experimentation provided by university technicians Mr. Jack Monahan and Mr. Gus Gillam.

Abbreviations

CFD	Computational Fluid Dynamics
EDMC	Engineering, Design & Manufacturing Centre
CAD	Computer-Aided Design
CAPEX	Capital Expenditure
OPEX	Operational Expenditure
ORC	Organic Rankine Cycle
NS	Navier-Stokes
RPM	Revolutions per Minute
INDC	Intended Nationally Determined Contribution
FiT	Feed-in Tariff

Design Report

FEEG6013 Group Design Project

45

Tesla Turbine Design

Pico-hydro for reliable and clean hydropower

Project Summary:

Our project features the design of a 100 W, 8 kg Tesla Turbine for pico-hydro applications, made to address the challenge of rural electrification by providing clean, reliable power to rural communities. Their needs and interests were identified and addressed in the design specification for the Tesla Turbine to ensure its effective implementation.

A large spectrum of component designs were reviewed and the most suitable features were integrated into a single proposal.

Our methodology was documented for both the analytical and CFD simulations, demonstrating technical expertise in honing the final design. Initialisation was done analytically to characterise flow between discs, yielding an optimal point (disc number = 5, scaling down factor = 2.25 and working RPM of 2000) showing an estimated power output of 148 W and 44 % thermal efficiency. Comparing results, we found higher predicted velocities for the analytical case. CFD plots indicate higher shearing forces and higher power output (216.37 W at 2000 RPM).

CFD was also used to inform geometric changes for the implementation of a novel volute casing using a high level overview of the flow field. Improvements were made to account for recirculation and angle of attack, leading to improved turbine performance.

The final assembly yielded a design that was novel and not previously explored in the literature (e.g. taper region within the volute). The materials were designated based on specifications for weight and durability, whilst still maintaining minimal impact on the local environment and ecology. This also aided in manufacturing a case for turbine's market viability where it was assessed against other renewable competitors.

Group Members:

ID Number	Name	ID Number	Name
29204461	Frederick Wong	29853818	Nicholas Khor
29127076	Shawn Navarednam	29859689	Jerry Ong Jun Wey
29070651	Chow Kai Jie		

Primary Supervisor: Dr. Davide Lasagna

Co-Supervisor: Professor John Shrimpton

Submitted on: 20/05/2021



Contents

1 Introduction

- 1.1 Background
- 1.2 Literature Review

2 Design Brief

- 2.1 Aims and Objectives
- 2.2 Stakeholder Analysis
- 2.3 Design Specifications

3 Design Process

- 3.1 Concept Designs
- 3.2 Design Selection Process

4 Analytical Modelling of Tesla Turbine Performance

- 4.1 Model Assumptions
- 4.2 Equations
- 4.3 Volute Casing Incorporation
- 4.4 Results

5 CFD Model

- 5.1 Background
- 5.2 Goals
- 5.3 Methodology
 - 5.3.1 Pre-processing
 - 5.3.2 Mesh
 - 5.3.3 Mesh convergence methodology
 - 5.3.4 Outer volute casing mesh
 - 5.3.5 Inner disc region (inter-disc) mesh
 - 5.3.6 Processing
 - 5.3.7 Solution parameters and boundary conditions
- 5.4 Results
 - 5.4.1 Mesh convergence analysis
 - 5.4.2 Performance evaluation using CFD
 - 5.4.3 Flow characteristics at the inter-disc region

6 Final Design Description and Component Selection

- 6.1 Inlet
- 6.2 Casing and Volute Channel
- 6.3 Disc Inlet (Taper)
- 6.4 Disc Stack
- 6.5 Discs
- 6.6 Outlet
- 6.7 Shaft
- 6.8 Alternator

7 Production & Commercialisation

- 7.1 Prototype Manufacture
- 7.2 Experimentation
- 7.2 Material Selection
- 7.3 Market Analysis & Financial Aspects
- 7.4 Environmental Impact and End-of-Life

8 Further Work

9 Conclusion

References

Appendices

1 Introduction

1.1 Background

Rural electrification

As part of the concentrated global effort towards sustainability, the United Nations' Sustainable Development Goal No. 7 details the target of affordable, reliable, sustainable, and modern energy for all. Efforts in this regard have accelerated in the past decade with 89 percent of people in the world having access to electricity as of 2017. Nevertheless, approximately 840 million people around the world still lack this access, with Sub-Saharan Africa accounting for a majority of the deficit. In Eastern and South-Eastern Asia, approximately 2% of the population still lack access to electricity [1].

Rural electrification is the process of supplying electrical power to rural and remote areas. In many cases, the implementation of conventional grid infrastructure in these areas is deemed infeasible due to reasons spanning economic, social and political factors. Sources such as World Bank Group [2] and Index Mundi [3] report that 100 percent of the Malaysian populace has access to electricity, whereas it can be argued that these numbers are only reflective of Peninsular Malaysia and do not account for the entire population of Malaysia due to the lacking scope of household surveys and other tools used. Instead, Ngah *et al.* quotes a lower coverage of 77 percent in Sabah and 67 percent in Sarawak [4].

Rural electrification harbours the possibility of improving the residents' overall quality of life by increasing productivity and enabling the use of specialised electrical appliances in industry and healthcare services. Furthermore, the introduction of a mini-grid reliant on hydropower can make services more affordable for the residents of as compared to electricity from portable diesel generators [5].

Pico hydro

Hydropower is driven by extracting the potential energy of falling water over a difference in height. A basic formula for potential hydropower yield [6], P , is

$$P = \eta Q_t H \rho g, \quad (1)$$

where η is efficiency, Q_t is total volumetric flow, ρ is density, H is head and g is the acceleration of gravity.

Depending on the region, the availability and access to certain hydropower sources may be less or more accessible as a result of the head and flow parameters. For instance, Giddings and Underwood have shown that within certain remote communities in the Great Britain, the potential for small-scale hydro power was low [7]. But in countries like Malaysia for example, hydropower can be generated on a small (1 – 10 MW), medium (10 – 100 MW), and large (> 100 MW) scale due to the abundance of free streams [8]. Annual surface run-off in Malaysia total to approximately 566 billion m³, this combined with the country's hilly areas and river networks gives it huge hydropower potential.

Nevertheless, the current challenges against hydropower development in Malaysia are economic, as hydroelectricity plants have higher upfront cost as compared to thermal power plants. Rising interest rates further enforce this cost factor as a barrier. Moreover, large hydroelectric installations and their corresponding reservoir affect the surrounding area significantly. For populated regions, relocation and resettlement of people in the reservoir area is necessary, which inadvertently affects local culture, religious beliefs, and burial sites. Large reservoirs may also restrict livelihood of the locals as they are dependent on the local ecology of forest and river [6].

Smaller scale hydro schemes such as micro and pico-hydro seek to alleviate this issue by utilising little to no storage in the form of run-of-the river schemes. In Malaysia, about 500 MW of small hydropower potential has been identified, with abundant low head site for potential micro-hydropower development [9] [10]. This revelation is not new as it has led to a growing emphasis on the development of mini-hydro projects under the 4th to 11th Malaysian Plans as part of the rural electrification initiative [11].

Pico-hydro are hydropower devices rated for less than 5kW scale devices and have been in use around the world for the past 30 years, mostly for rural electrification in developing countries [12]. In Malaysia, local



institutions have conducted their own research [8] including a Pelton turbine implementation at University Malaysia Pahang [13].

The majority of devices used in hydropower generation can be categorised as either impulse turbines or reaction turbines. Impulse turbines function via pressurised water transferring their kinetic energy by impacting turbine blades or buckets and causing them to rotate. Examples include the Pelton wheel, Turgo wheel and crossflow turbines. Meanwhile, the working principle of reaction turbines relies on directed water flow creating a pressure difference across the turbine blades, creating a differential to rotate the turbine. Examples include Kaplan and Francis turbines [14].

Tesla Turbine

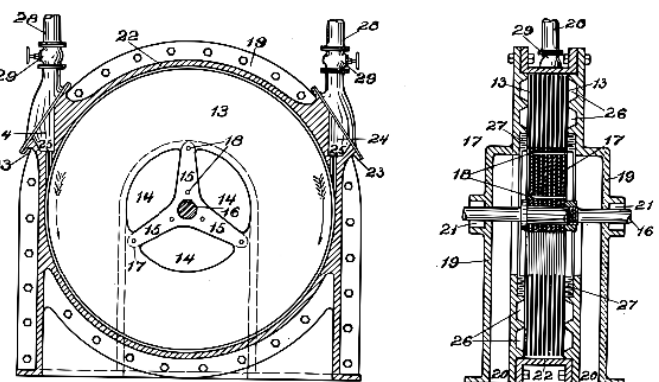


Figure 1 Schematic of the Tesla Turbine from the 1913 patent.

to further restrict fluid flow such that all fluid is forced to exit through the outlet. Fluid enters the main chamber through a diverging nozzle which works to jet it onto the discs.

The mechanics of the Tesla Turbine begins with fluid entering the main chamber through the inlet. The fluid is jetted in the tangential direction along the surfaces between the disc spacings. Due to viscosity, the fluid directly adjacent to the surface experiences the no-slip condition, creating a velocity gradient in the perpendicular direction away from the surface of the disc. As the fluid energy is converted into mechanical work, the flow spirals towards the centre of the disc and exits axially through the orifices and outlet.

The reason for our investigation into the Tesla Turbine is its potential benefits over conventional pico-hydro devices in resistance to wear and manufacturing ease of its components.

1.2 Literature Review

The field of Tesla Turbine study has seen significant growth over the years with contributions in different applications and design aspects. The most relevant of which to pico-hydro was presented by Ho-Yan in their proposed 300W design. They view Tesla Turbines as feasible for use in pico-hydro power generation because of its simple, easily manufacturable components, allowing for communities with basic workshop capabilities to craft replacements easily. They also note the challenges against Tesla Turbines such as size and cost-effectiveness. However, they concluded that their approach was preliminary and only useful as a comparative tool to future Tesla Turbine designs [16].

Other modern works on Tesla Turbines use air as the working fluid rather water. Krishnan *et al.* features the design and testing of microscale Tesla Turbines featuring 1 cm rotors. Their work characterises the non-dimensional rotor behaviour within the turbine and discusses on the effect of scaling on power density and inter-disc space [17]. One of the key differences in operating design is the turbine speed whereby air-based studies report RPMs of greater than 5000 whereas our proposed design foresees operational speeds of less than 3000 rpm. Of the main challenges surrounding Tesla Turbines is the undesired warping of discs due to the lack of robustness of disks and high rotational speeds induced [16].

Tesla Turbines have been used in a large spectrum of low power applications with different types of fluid medium, one of which are organic fluids. The Organic Rankine Cycle (ORC) has shown to be effective in producing energy for low grade utilization [18]–[20]. A thermodynamic model has been developed by Song

et al., adopting non-dimensional parameters to validate relationships between turbine parameters and efficiency. The study showed that inlet velocities have a profound effect on the turbine performance, and that R245ca as a working fluid yielded the highest power output [21]. Ciappi *et al.* investigated the performance of a Tesla Turbine operating with various organic working fluids (R404a, R134a and R245fa) under different temperatures, pressures, and RPM. The results showed that Tesla Turbines could potentially be used for micro and small power expanders [22]. 3D computational fluid dynamics for ORC Tesla Turbines were compared with analytical 2D code to assess the effects derived by the interaction between the admission nozzles and rotor when using refrigerants, showing that flow field distribution at the inlet were affected by partial admission effects [23].

Table 1 summarises the past studies done in Tesla Turbines. It infers that many prior studies involving Tesla Turbines are focused onto working mediums of air and steam, with limited depth into its applications in water. Nevertheless, previous studies give a good indication of the physical scale in the form of rotor sizes to power output expected. The Tesla Turbines by Romanin *et al.* and Ho-Yan *et al.* were considered for direct adaptation because of their water-based medium. However, both presented their own hurdles which made them unsuited to our design specifications, with Romanin's too low of a power output and Ho-Yan's being too heavy.

Table 1 Summary of past Tesla Turbine studies.

Study	Rotor diameter, mm	No. of discs	Disc spacing, mm	Working Fluid	Rotor Speed, rpm	Power, W
Armstrong	177.8	10	Variable	Steam	6000	530
Beans	152.4	6	12.7	Air	17000	5600
Rice	177.8	9	1.6	Air	11800	1800
Leaman	126	4	3.2	Air	9000	87
Lemma	50	6	-	Air	96000	220
Tesla	457	25	-	Steam	9000	150'000
Emran	37.6	4	-	Air	50000	-
Peshlakai	150	12	1.3	Air	-	12
Bloudichek	200	13	-	Air	-	58.3
Romanin [24]	5	4	0.5	Water	-	35
Shah, 2017 [25]	47.5	8	1	Air	4500	137.83
Hoya & Guha [27]	46	8	0.2	Air	25000	140
Ho-Yan [16]	250	31	5	Water	500	300

2 Design Brief

2.1 Aims and Objectives

The goal of this project is to design and optimise a Tesla Turbine for pico-hydro applications capable of providing a useful and reliable source of power at an affordable price. To meet this goal, the following objectives were outlined:

- Identifying with justification the niche for pico-hydro Tesla Turbine implementations.
- Reviewing the current state of hydro and smaller scale hydro in the aforementioned region.
- Design the entire Tesla Turbine assembly and its supporting components.
- Sizing optimisation of the turbine design based on target power output via analytical solutions.
- Validate analytical results with that from CFD simulations.



2.2 Stakeholder Analysis

Table 2 Stakeholder analysis.

Stakeholder	Needs and Interests	Actions Taken
Supervisors	<ul style="list-style-type: none"> The original idea for the application of the Tesla Turbine in a hydropower setting stems from Dr. Lasagna. Alongside with the technical advisory provided by Professor Shrimpton, both parties are invested in the development and outcomes of the present work. 	<ul style="list-style-type: none"> Weekly meetings for general progress and queries. Open channel of communication via Microsoft Team and/or email to address specific queries.
Team Members	<ul style="list-style-type: none"> Communication between members in lieu of the collaborative effort required to complete this work. Cooperation between members in contributing and improving the present work 	<ul style="list-style-type: none"> Meetings thrice a week, separate from aforementioned supervisor meeting. Open channel of communication via Microsoft Team and/or WhatsApp group chat.
Rural communities	<ul style="list-style-type: none"> Preservation of local environment and ecosystems. Cost-effective solution 	<ul style="list-style-type: none"> Product footprint as key factor in design process. Product cost as key factor in design process.
Wider Hydropower Devices Market	<ul style="list-style-type: none"> Respecting market competition and fair play 	<ul style="list-style-type: none"> Acknowledgements of copyright and existing products
Suppliers	<ul style="list-style-type: none"> Proper etiquette and respectful demeanor in communication. Adherence to local and national laws and tax rates when conducting business. 	<ul style="list-style-type: none"> Proper documentation presented when needed.
Academia	<ul style="list-style-type: none"> Academic integrity must be adhered to in the best interest of the wider academic scene. This is to ensure that the ideas and knowledge presented is credible and respectful of past work done. 	<ul style="list-style-type: none"> Quality and transparency in present work with sufficient details to ensure replicability. Fairness in declaration of conflicts of interest and other necessary information. Proper citations in respect to past work done.

2.3 Design Specifications

The design specifications for our Tesla Turbine in *Table 3* are based on the needs of the target market as detailed in 2.2 Stakeholder Analysis. Other external factors affecting our design specifications are the testing conditions available to us in the University of Southampton campus.

100 W was determined as a compromise between usability and portability. Higher ratings would demand greater scale in dimension and weight whilst lower ratings would limit use of the turbine to low power use cases. In consideration of the target rural communities' need for preservation of the local environment and its surroundings, the turbine specification is also limited to 30 cm in each dimension. To maintain portability, 30 kg was deemed the limit and intended as the carry weight of two adults. Finally, a cost limit of £200 was set to make it affordable.

Based on laboratory and experimental settings provided by technicians Mr. Jack Monahan, mass flow rate was set to a constant of 1 kg s^{-1} .

Table 3 Design specifications for the Tesla Turbine.

Feature	Target
Power Output, W	100
Physical footprint, cm ³	Less than $30 \times 30 \times 30$
Weight	Less than 30 kg
Cost	Less than £200 (commercial manufacturing)
Inlet Conditions	$< 1 \text{ kgs}^{-1}$

3 Design Process

Our project timeline is represented by the flowchart in Figure 2. Our design process can be summarised as below:

- Exploration and scoping present work related to Tesla Turbines.
- Direct and indirect stakeholder analysis and setting design specifications.
- Quantifying external parameters and performance targets.
- Initialise rotor parameters using analytical solutions.
- Forming the preliminary design of the turbine exterior and supporting components based on rotor.
- Cross-validation of analytical solutions and CFD results.
- Further component design optimisation using CFD.

Roles

Shawn Navarednam	CFD Lead
Nicholas Khor	Logistics Lead
Frederick Wong	Design Lead
Chow Kai Jie	Analytical Modelling Lead
Jerry Ong	Materials Lead

3.1 Concept Designs

In the preliminary stages, we investigated the key features and characteristics of the Tesla Turbine to determine their importance and effects on overall performance of the turbine. From the schematics in the original patent and past Tesla Turbine work, we identified several important components

Inlet nozzle: We investigated various nozzle geometries for commercial implementation.

Disc stack: as the primary energy harvesting component. We started to research on its geometry such as the inter-disc spacing, disc thickness, disc outer and inner radius.

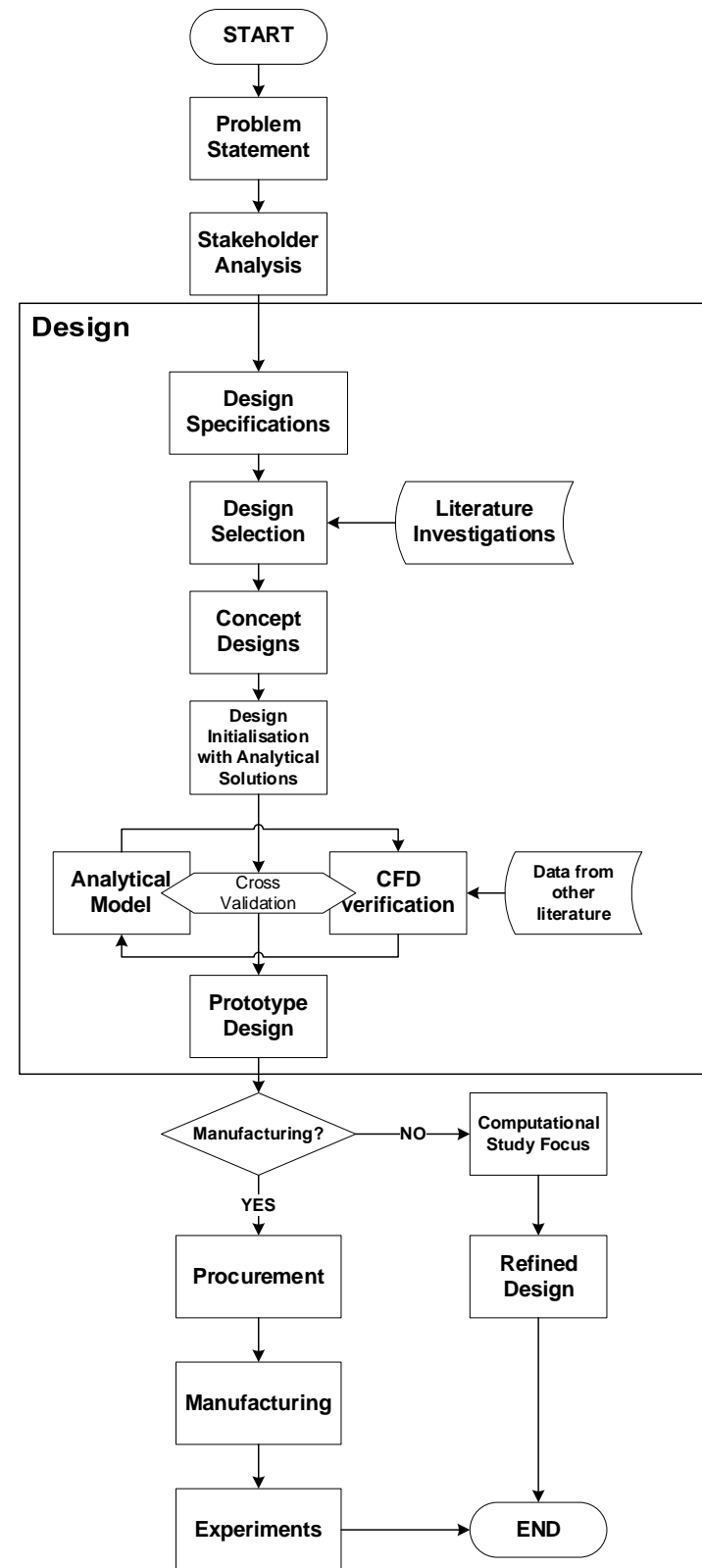


Figure 2 Project timeline.



Outlet system: We studied the types of orifices or hub that can be used and their effect on the turbine performance.

Casing design considerations

The casing largely dictates the flow conditions into and out of the discs. From the literature, two major forms of losses were identified: 1. Expansion at the nozzle and therefore pressure losses; 2. Outlet conditions/geometries that cause a sudden change in flow direction. Nozzle losses were more significant when dealing with compressible fluids while outlet losses were more dominant for incompressible fluid [17], [27], [28]. For this reason, much time was spent on selecting the optimal design. Shown below are among the many design aspects considered when choosing the final design.

3.2 Design Selection Process

For multichannel Tesla Turbines, geometric parameters such as nozzle geometry, disc outer spacing, disc outer diameter, disc spacing distance, and disc thickness are geometrical parameters that have significant effect on the performance and flow field of the turbine [29], [30]. Similar results were reported by Bean after exploring the influence of rotor speed, turbine inlet pressure and disc spacing in Tesla Turbine, showing that these parameters largely govern the overall performance [31]. However, there have been limited studies looking into the impacts of disc thickness and spacing on multichannel Tesla Turbine performance [32].

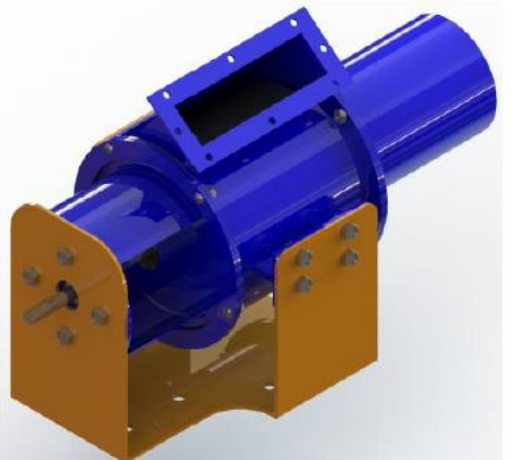


Figure 3 Open flow Tesla Turbine casing designed by Andres and Loretero. The inlet was made especially large to account for larger flow rates [34].

Open Flow Turbines

We found that open flow Tesla Turbines often incorporate features from the more traditional Pelton wheel. For instance, Khan *et al.* suggested a Tesla Pelton turbine to enhance the torque. Many of these turbines could also be placed in series along open sources such as canals and rivers to generate more power [33]. Andres and Loretero evaluated the performance of the Tesla Turbine with an adapted casing for implementation in irrigation canals as shown in Figure 3. Despite being able to handle larger mass flow rates (7.55 kgs^{-1}), the maximum power output was only 10.73 W with an efficiency of 26.34% [34].

Plenum Chambers

The overall efficiency of disc turbines is largely influenced by losses experienced in the inlet and nozzle. However, Guha and Smiley designed a plenum chamber integrated nozzle, demonstrating less than 1% loss in total pressure can be achieved. Within the plenum tube, a near stagnant flow is developed, eliminating large pressure gradients. Furthermore, the use of plenum tube was observed to provide more uniform jet, leading to enhanced overall efficiency [35]. When incorporating a plenum chamber, a diffuser should be used at the inlet of the plenum chamber. This would allow the majority of the flow kinetic energy to be conserved and converted into static pressure [36]. Figure 4 shows an initial plenum nozzle design.

For effective implementation of a plenum chamber, chamber length, divergence angle, and Reynolds number are among the factors that have to be considered. The natural tendency of fluid in a diffusion process is to break away from the walls of the diverging passage, reverse its direction and flow back in the direction of the pressure gradient. When an abrupt enlargement in duct section occurs, the flow cannot follow the contour of the duct causing separation. Chandavari and Palekar used CFD to show that optimal diffuser taper was below 7° , tapers above this angle are likely to

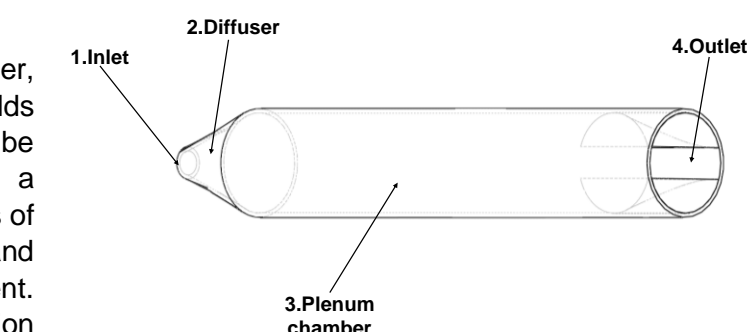


Figure 4 Initial plenum chamber design. A rectangular outlet was fashioned to channel fluid into the inter-disc region more uniformly. Plenum length and diffuser angle were designed to prevent the formation of recirculatory regions while allowing the boundary layer to reattach before reaching the outlet.

observe recirculation [37]. Sparrow *et al.* investigated the relationship between Reynolds number and separation, showing that at high Reynolds number flows are less sensitive to diffuser angle while low Reynolds number flows exhibit recirculation even for taper angles below 7° [38]. Lastly, taking recirculation into account, the plenum chamber has to be long enough to allow flow reattachment to the plenum chamber wall before reaching the converging nozzle. The reattachment length can be estimated through empirical data obtained from previous research, taking into account the inlet and outlet geometry, diameter, Reynolds number, centerline turbulence level, and inlet Mach number [39].

Plenum and Vaned

In ORCs, the Tesla Turbine is used for high pressure and temperature applications. Two critical design concepts were adopted from these turbines. The stator and rotor are important components for energy conversion. In axial turbines, stator rings are used to receive air from an inlet duct and deliver it to the next stage at the correct velocity and pressure [40]. Talluri *et al.* studied the performance of a plenum chamber and rotor-stator integrated Tesla Turbine as shown in Figure 5 [41]. This combination allowed for decreased pressure losses while enabling improved angle of attack control. The design also allows integration of multiple nozzles with the plenum chamber acting as a buffer before being channeled into the discs. It was found that the total efficiency increased almost linearly with decreasing throat width ratio (ratio between stator outlet area and rotor inlet area).

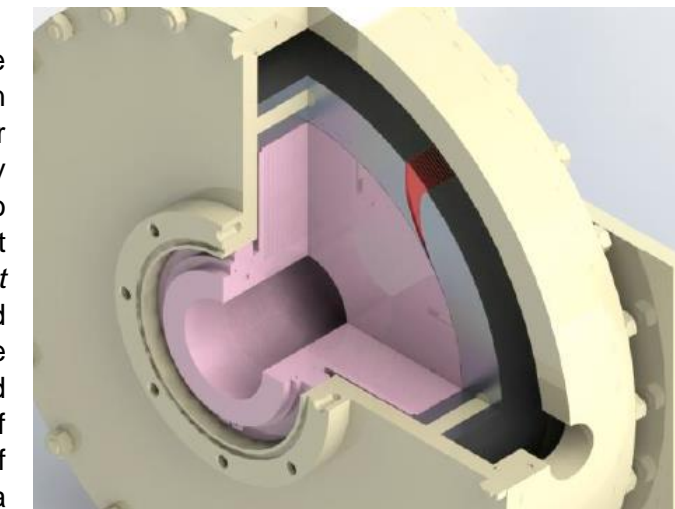


Figure 5 Tesla Turbine design for high pressure applications suggested by Manfrida *et al.* [115] showing the implementation of turbine blades (pink) and stator ring (silver) within a radial plenum chamber (yellow). The nozzle geometry is defined by the stator ring and is highlighted in red.

Concerns pertaining to this turbine type include high manufacturing difficulty up to a sufficient degree of accuracy. Similarly, this turbine type is usually coupled with the use of refrigerants for higher power generation (as compared to using water as the fluid medium), the fluid medium contains minimal impurities that could result in turbine damage. For commercial power generation (100 – 200 W), to be adaptable for open source applications, the turbine has to be robust, durable, and require low maintenance. A smaller throat width ratio may increase efficiency but also worsen the chances of blockage.

Outlet Geometry

We found limited research pertaining to investigating the influence of Tesla Turbine outlet geometries on the overall turbine performance. Despite the lack of research, Rice has shown that outlet system geometry can

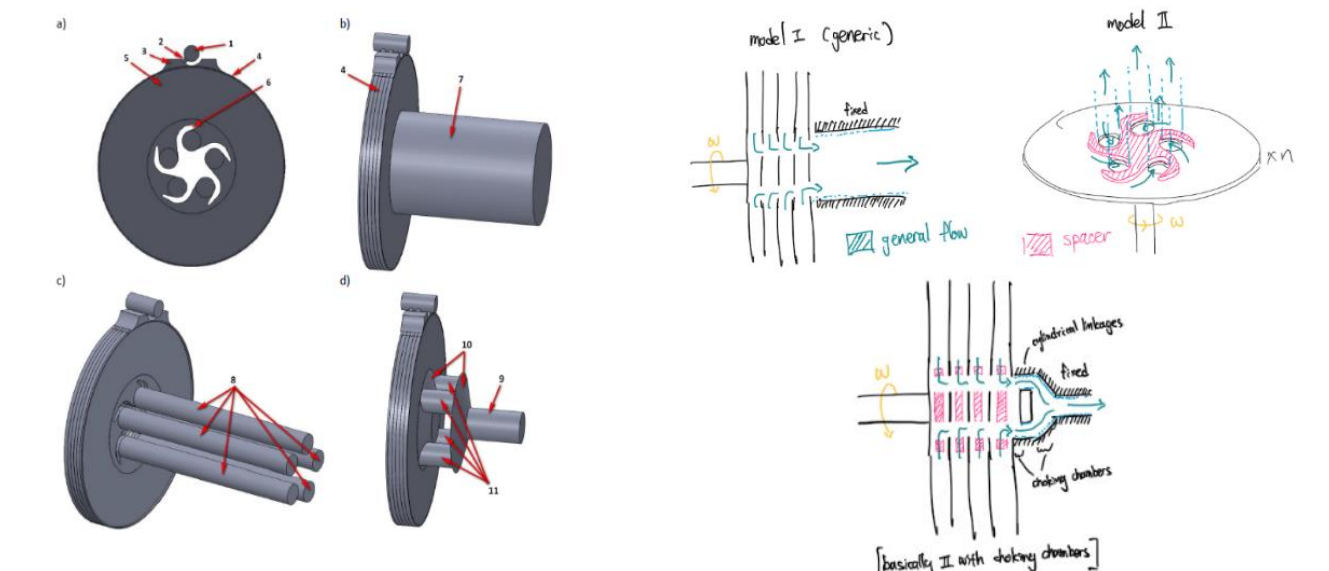


Figure 6 (Left) Computational domains: a) front view of models with spacers, b) model I, c) model II, d) model III; (Right) Personal hand-drawn illustrations



contribute to turbine efficiency losses [42]. A computational study by Rusin analysed three different kinds of outlets, looking into the flow phenomena caused by the outlet system. Results suggested that differences between the models and power generated were mainly attributed by swirl regions, where backflows and swirls were shown to decrease generated power [43]. In a turbine equipped with an axial outlet, the working fluid flows spirally in disc channels and then axially through the exhaust vent. This forces a change in flow direction, causing energy losses. Compared to radial outlets, isentropic efficiency of turbines with an axial outlets were lower, while the flow coefficient was larger [44].

The following three main outlet systems such as choking chamber (Model III), main orifice (Model I) and, individual separated orifices (Model II) are analysed. Although the working medium used in the research was air, it still provides some insights on how fluid might behave in the turbine.

Their study has also shown that the model with separated orifices yields the highest power compared to the other two. It was observed that the larger the swirled region, the lower the power extracted which was consistent with the results obtained by the author. This is also in line with the concept of excessive space which may cause fluid recirculation.

Turbine blade design considerations

The disc geometry and operating conditions largely determine the power generated. Overall scale of the turbine was dictated by geometric requirements by the disc. Effects of factors such as disc spacing, thickness, rotational speed etc. were thoroughly analysed to determine the optimal operating conditions. Final disc parameters were chosen following from the analytical study carried out in Section 4, and justified using previous experiments in the literature.

Impact of number of discs

The Tesla Turbine is capable of reaching efficiencies close to that of 95%, but the flow has to be laminar. This can be achieved by reducing the flow rate and increase the number of discs used [42]. Tesla Turbine torque is directly proportional to the number of discs. Tan calculated for the optimal number of discs using the dimensionless parameter deduced by Hasinger and Kehrt [45], the number discs required was back-calculated using a specified flow rate. The number of discs were decreased from 21 to 13, showing a reduction in head losses (which occur mainly for axially placed outlets) [46]. A similar study was conducted by Krishnan, analysing the effects of 8, 13, and 20 discs. Maximum efficiency was achieved using 13 discs, efficiency observes a slight decrease after this point [47]. Hoya and Guha reported an increase in turbine efficiency with more discs as well but were meet with excessive test rig vibrations at high angular speeds when a larger number of discs were used [27].

Impact of disc spacing

Bean reported on the increase in turbine performance with an increase in supply pressure or inlet velocity and decrease in spacing ratio as both parameters increase the fictional effects on the turbine [31]. Rice reported peak Tesla Turbine performance when disc spacing is approximately equal to twice the boundary layer thickness. If the spacing is too small, the boundary layers of two disc surfaces might interfere with each other, decreasing turbine performance. Alternatively, if the spacing is too large, momentum exchange is

Area	Power [W]		
	Model I	Model II	Model III
Disc 1	10,68	13,04	11,36
Disc 2	7,10	8,06	7,83
Disc 0	5,27	6,93	6,07
Rim 1	0,69	0,86	0,67
Rim 2	0,71	0,67	0,69
Rim 0	0,06	0,02	-0,04
Spacer 1	-	0,99	0,33
Spacer 2	-	1,17	0,19
Total	24,51	31,74	27,10

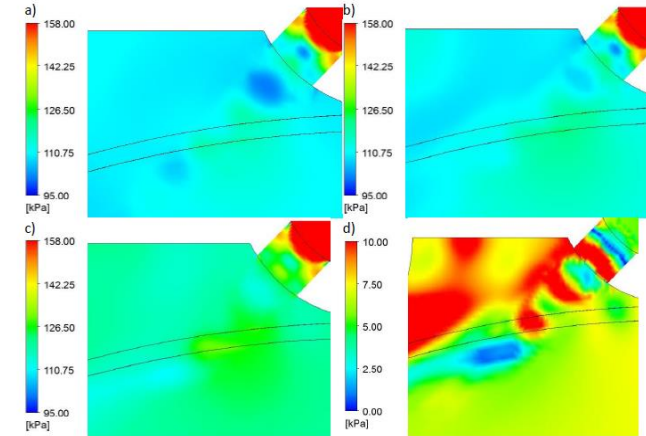


Figure 7 (Left) Static pressure distribution a) in model I, b) in model II, c) in model III and d) difference between models II and III; (Right) Power obtained from numerical models.

limited between the fluid and disc, also decreasing performance [42]. Galindo *et al.* also show that if the disc spacing is too small, viscous forces resist fluids from entering the inter-disc region, and when too large, the fluid losses adhesion and its kinetic energy is not transmitted as efficiently to the discs [48]. Qi *et al.* investigated the influence of seven disc spacing distances on turbine performance using CFD, validating a decrease in isentropic efficiency with disc spacing increase and decrease from the optimal value, also showing that the Ekman number can be used to calculate for optimal disc spacing [29]. Similar results were reported by Sengupta and Guha, showing that changes in the disc spacing significantly affect the velocity field near the inlet, therefore affecting the turbine performance [49].

Impact of surface roughness

Disc surface roughness is significant in improving Tesla Turbine performance, shear stresses on the disc walls may be increased by increased turbulence in the boundary layer. Rusin *et al* quantified the influence of disc roughness on performance characteristics of the Tesla Turbine, showing that even a small increase in roughness can result in a significant rise in simulated power. Generated power rose by 35% when roughness was introduced, however, the effect tapered off as roughness was increased [50]. Borate and Misal reported similar results, showing a possible increase in turbine efficiency up to 45% using discs with higher surface roughness [30].

Impact of disc thickness

The original Tesla Turbine has tapered edges, this was believed to increase efficiency and reduce tip losses. Hasinger and Kehrt investigated the use of Tesla Turbine discs in shear force pump applications, where instead of flat - cylindrical discs, cones or concentric cylinders were implemented. However, no performance advantages were observed [45]. Losses that occur at the tip are mainly due to fluid contact with the discs and trying to flow into the inter-disc space, suggesting an improvement in flow dynamics with thinner disc geometries. At the same time, discs with lower thicknesses are susceptible to warping until high RPM conditions, as shown by Tesla in his initial experiments [51]. Disc thickness was shown to be a less significant factor under sub-sonic, incompressible conditions. Li *et al.* showed a reduction in shock losses when disc thickness was minimized, by specifying lower thicknesses, these losses could be neglected [28].

Inlet angle

A study comparing inlet angle of 10° and 15° found that the increased slope angle of the inlet supply nozzles cause a small decrease in the isentropic efficiency (6 – 8 %) and output power of the turbine [52]. Holland tested for inlet angles ranging from 2.5° to 45° from tangential, contrary to that reported in previous literature, nozzle angle of 45° was found to achieve maximum power. However, this may be due to a disc pack variant that was used for experimental tests [26]. Lampart *et al.* investigated turbine performance for nozzle angles of 10°, 15°, and 20° using air as the medium. Nozzle angle of 20° was shown to give the highest efficiency, but other variables were not kept constant throughout the experiment, therefore a direct comparison cannot be made [53].

Rotational speed

Power output by Tesla Turbines vs rotational speed largely follow a quadratic curve, reaching a maximum and then decrease steadily with higher angular velocities. Most experimental results show a parabolic relationship between turbine efficiency and rotor RPM [31], [52], [54]. The literature suggests maximum theoretical efficiency when the rotational speed of the discs was equal to that of the inlet velocity of the fluid [55], [56], further emphasizing the need for a well-designed inlet. The torque approaches a steady state value as the disc tip speed approaches fluid velocity [26] In general, higher RPM results in greater centrifugal forces and longer streamlines, which is desirable as it increase momentum transfer and hence efficiency [57]. A study by Lampart *et al.* comparing RPM at 9000 and 18000 showed the RPM affects the shape of the streamlines and time spent by the fluid in the inter-disc space [52].

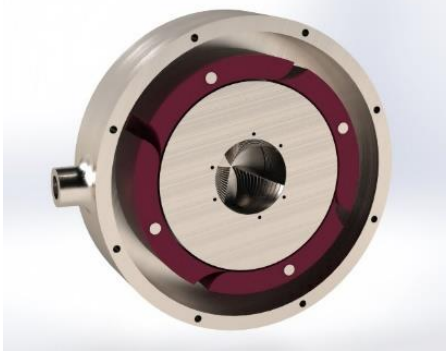
Number of nozzles

Previous studies have considered the axisymmetric nature of the flow field within the inter-disc spacing of the Tesla Turbine, which may be improved by increasing the number of inlet nozzles or by implementing a plenum chamber near the rotor inlet [58]–[61]. Arrangements that employ one to four nozzles always produce non-axisymmetric, three dimensional flow patterns within the microchannels of the disc [26], [62]. Sengupta and Guha show more uniform flow conditions when the number of nozzles were increased, assisting in the



attainment of more axisymmetric conditions. Nozzle increase was also linked to a decrease in the operable range of the disc rotation speed, increase the maximum possible efficiency. Establishing axisymmetric boundary conditions provide the highest possible efficiency. [49]. That being said, a study comparing 2, 4, 6, and 8 nozzles found output power and isentropic efficiency to be the highest for the 4 nozzle case, further increase of the number of nozzles has an adverse impact on flow efficiency [52]. The impacts of multiple nozzles with varying geometries was evaluated with Krishnan, exploring the effects of different nozzle inlet and outlet geometries (circular inlet + slit/ oblong outlet, circular inlet + split outlet and funnel shaped), finding

Table 4 The three main designs considered in this study is shown below. These designs were put forward after in depth analysis of the literature, accounting for casing and disc performance. The turbine size was estimated according to the 100 W power generation.

Concept design	Description	Advantages	Disadvantages
Axial turbine casing coupled with Tesla Turbine discs	 <p>This design was to facilitate for a more robust method to channel a large volume of fluid from a large open source into the inter-disc gaps. Multiple vanes at the end of the turbine would gradually change the fluid angle until a specific angle of attack was achieved. The discs spin a shaft that is placed within the turbine casing, which in turn is connected to an alternator. The outer case is not shown in the Figure to the left.</p>	<ul style="list-style-type: none"> Less dependent on water source angle of attack. Able to handle large mass flow rates. Easy to implement in open water sources. Flow outlet would be oriented downstream of the flow, the probability of backflow is lower. 	<ul style="list-style-type: none"> Challenging to manufacture. It is expected that the lead time required would be too long and manufacturing costs will be high. Requires the use of gears, linking the Tesla Turbine discs with the alternator shaft. This brings about durability issues. Flow angle is changed abruptly, resulting in losses. Using CFD, pressure losses were prominent within the case, especially nearing the vane region. Gear system had to be waterproof and sealed with a labyrinth seal to ensure durability
Tesla Turbine disc integrated within a plenum chamber	 <p>Inspired from Organic Rankine Cycle (ORC) turbines, a stator nozzle was implemented to direct the flow at a tangential angle of attack into the inter-disc spacing. The disc and stator nozzle system were placed within a plenum chamber with one or more inlets, alleviating pressure losses while ensuring equal uniform pressure distribution. Triple spiral patterned at the disc core were designed to aid fluid flow out from the system. Stator nozzles can easily be 3D printed.</p>	<ul style="list-style-type: none"> Lower pressure losses (CFD validated) Multiple inlets can be connected to the plenum chamber system to increases the mass flow rate and therefore power output. Angle of attack can be easily varied using 3D printing with a short lead time for in-lab testing. Thickness and material of outer casing could be changed to accommodate for high pressure fluids in various applications. Less sensitive to pulsating flows 	<ul style="list-style-type: none"> Outer plenum chamber manufacture expected to have a long lead time and have high costs. Triple spiral patterns proved to be too difficult to manufacture, mainly due to being too thin. Challenging to implement in open water sources. Challenging to 3D print stator nozzle with sufficient precision given the facilities. Nozzle exit point must have a ultra-small area for significant flow acceleration. Flow angle is changed abruptly, resulting in losses.
Tesla Turbine disc integrated within a volute casing	 <p>Inspired from a turbocharger, the discs were placed within a volute casing. The volute casing was designed to accelerate the flow into the discs while distributing pressure uniformly. This was the final concept chosen with minor changes to the nozzle, disc and outlet region after consulting CFD and analytical results.</p>	<ul style="list-style-type: none"> Angle of attack can be easily varied using 3D printing with a short lead time for in-lab testing. Low manufacturing cost. Using CFD, the casing was shown to distribute pressure uniformly. Smooth flow transition throughout. Size is much smaller, more portable. Most robust and durable, has the least components to be manufactured. 	<ul style="list-style-type: none"> Challenging to implement in open water sources. Lower maximum power output as compared to other designs A lighter turbine may be more susceptible to vibrations at high RPM.



4 Analytical Modelling of Tesla Turbine Performance

In the Tesla Turbine, the principal mechanism for power generation occurs at the disc stack where fluid rotates the discs through adhesive effects. Therefore, many studies were done to characterise the flow within the disc stack as to better understand the influence of disc parameters and hence, evaluate optimal designs for maximum performance.

Goals of Analytical Model:

- Optimising Tesla Turbine's design via simple analytical numerical schemes.
- Characterising flow behaviour between two rotating discs and its impacts on power generation.
- Determining the impacts of design scaling on the overall turbine performance.
- Analytical validation of flow assumptions with that obtained from CFD and past work.

With the objective of peak efficiency, numerical flow analysis was included in this study to capture key design factors impacting the turbine's flow. In past literature, one of the earliest numerical investigations working on this front was published in 1965 by Warren Rice [63]. In their study, a crude analytical idealisation was devised such that it captured the flow profile with relative accuracy without requiring heavy mathematical complexity. Rice's methodology has since been attracting much attention in the field of Tesla Turbine analysis due to its simplicity and range of applicability.

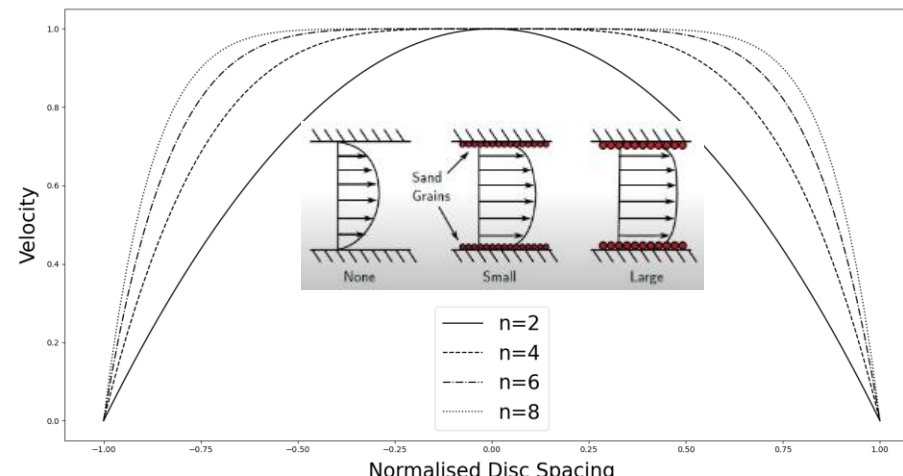


Figure 8 Microstructure Velocity Modifier

Following up on this, Sengupta *et al.* investigated a formulation for the inter-disc flow field in a three-dimensional setting under a fixed pressure drop. They found that efficiency decreases with increasing flow rate [64]. It was also noted that the experimental efficiencies were consistently lower than their analytical counterpart due to the omission of losses from bearings, nozzles and seals.

Similarly, Romanin and Carey developed a three-dimensional integral perturbation model with surface micro-structuring incorporated (Figure 8), generalising upon the conventional Poiseuille flow assumption [65]. Dimensionless parameters were highlighted throughout the study to provide a direct assessment of their relative impacts on fluid pressure, viscosity and momentum. All of which ultimately affected turbine performance. In addition to Carey's work, Krishnan *et al.* applied a similar model with the inclusion of parameter-scaling and loss mechanisms as to practically correlate theoretical efficiency and thus design optimisation [17]. It was shown that the turbine was able to put out near 40% efficiency when scaled down to the millimetre regime for incompressible flow (water).

For this study, Carey and Romanin's mathematical model was recreated to analyse inter-disc flow field characteristics in combination with a novel volute casing design integration. This was followed by design optimisation in accordance to maximum power efficiency as well as practical manufacturing limitations.

4.1 Model Assumptions

The following section of the study presents the building blocks leading up to the derivation of the analytical solutions used to initialise the parameters of the disc stack. An illustration of the cylindrical coordinates used are shown in Figure 9, where r , θ

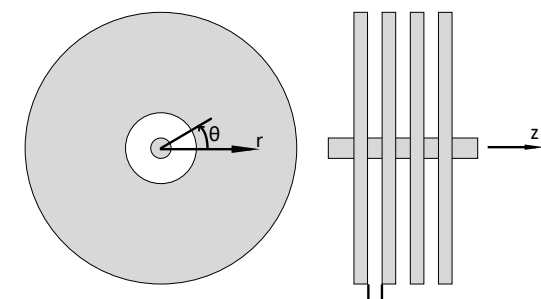


Figure 9 Schematic of Turbine rotor discs.

and z represent the radial, tangential and axial direction of the rotor disc, respectively. The immediate section below shows the annotations used for equations & derivations throughout this study.

Annotations

\bar{v}	Axially Averaged Velocity	n	Profile modifier
v_r	Radial Velocity	b	Inter-disc space
v_θ	Tangential Velocity	μ	Dynamic Viscosity
v_z	Axial Velocity	ν	Kinematic Viscosity
P	Pressure	ρ	Density
r	Radial Value	ω	Angular Velocity
r_0	Disc Outer Radius	f	Friction factor
θ	Azimuthal Direction	U	Disc Velocity
z	Axial Direction	U_0	Tip Disc Velocity
ξ	Radius Ratio	U_i	Inner Radius Disc Velocity
P_{total}	Total Power	τ_w	Wall Shear
D_H	Hydraulic diameter	Po	Poisseuille number
F_{Po}	Enhancement Number	\dot{m}_c	Mass Flow Rate
η_i	Isentropic Efficiency	Re_c	Reynolds number
V_{r0}	Dimensionless Radial Velocity	\hat{W}	Dimensionless Tangential Velocity Difference
ε	Disc Gap Aspect Ratio	\hat{P}	Dimensionless Pressure Difference
T	Torque	Re_m^*	Modified Reynolds Number
η_{rm}	Mechanical Efficiency	n_d	Disc Number
Δh_{isen}	Isentropic Enthalpy Drop		

Assumptions

- Steady, incompressible laminar (Poiseuille) flow.
- Negligible entrance effects and axial flow velocity ($v_z = 0$).
- The flow field is radially symmetric. The inlet flow at the rotor outer edge is assumed uniform, resulting in a flow field that is constant at any angle, θ .
- Constant friction factor characteristics within the flow passage.



4.2 Equations

Navier-Stokes (NS) equation in cylindrical coordinates

The model begins with the following NS equations for describing flow based on cylindrical coordinates system.

- Continuity:

$$\frac{1}{r} \frac{\partial(rv_r)}{\partial r} + \frac{1}{r} \frac{\partial v_\theta}{\partial \theta} + \frac{\partial v_z}{\partial z} = 0$$

- Radial direction momentum:

$$v_r \frac{\partial v_r}{\partial r} + \frac{v_\theta}{r} \frac{\partial v_r}{\partial \theta} + v_z \frac{\partial v_r}{\partial z} - \frac{v_\theta^2}{r} = -\frac{1}{\rho} \left(\frac{\partial P}{\partial r} \right) + \nu \left\{ \frac{1}{r} \frac{\partial}{\partial r} \left(r \frac{\partial v_r}{\partial r} \right) + \frac{1}{r^2} \frac{\partial^2 v_r}{\partial \theta^2} + \frac{\partial^2 v_r}{\partial z^2} - \frac{v_r}{r^2} - \frac{2}{r^2} \frac{\partial v_\theta}{\partial \theta} \right\}$$

- Theta direction momentum:

$$v_r \frac{\partial v_\theta}{\partial r} + \frac{v_\theta}{r} \frac{\partial v_\theta}{\partial \theta} + v_z \frac{\partial v_\theta}{\partial z} + \frac{v_\theta v_r}{r} = -\frac{1}{\rho r} \left(\frac{\partial P}{\partial \theta} \right) + \nu \left\{ \frac{1}{r} \frac{\partial}{\partial r} \left(r \frac{\partial v_\theta}{\partial r} \right) + \frac{1}{r^2} \frac{\partial^2 v_\theta}{\partial \theta^2} + \frac{\partial^2 v_\theta}{\partial z^2} - \frac{v_\theta}{r^2} - \frac{2}{r^2} \frac{\partial v_r}{\partial \theta} \right\} + f_\theta$$

- Z direction momentum:

$$v_r \frac{\partial v_z}{\partial r} + \frac{v_\theta}{r} \frac{\partial v_z}{\partial \theta} + v_z \frac{\partial v_z}{\partial z} = -\frac{1}{\rho} \left(\frac{\partial P}{\partial z} \right) + \nu \left\{ \frac{1}{r} \frac{\partial}{\partial r} \left(r \frac{\partial v_z}{\partial r} \right) + \frac{1}{r^2} \frac{\partial^2 v_z}{\partial \theta^2} + \frac{\partial^2 v_z}{\partial z^2} \right\} + f_z$$

Appling the assumptions stated above, the NS equation can be further simplified as follows,

- Continuity:

$$\frac{1}{r} \frac{\partial(rv_r)}{\partial r} = 0 \quad (1)$$

- Radial direction momentum:

$$v_r \frac{\partial v_r}{\partial r} - \frac{v_\theta^2}{r} = -\frac{1}{\rho} \left(\frac{\partial P}{\partial r} \right) + \nu \left\{ \frac{\partial^2 v_r}{\partial z^2} + \frac{1}{r} \frac{\partial}{\partial r} \left(r \frac{\partial v_r}{\partial r} \right) - \frac{v_r}{r^2} \right\} \quad (2)$$

- Theta direction momentum:

$$v_r \frac{\partial v_\theta}{\partial r} + \frac{v_\theta}{r} \frac{\partial v_\theta}{\partial \theta} = f_\theta \quad (3)$$

- Z direction momentum:

$$-\frac{1}{\rho} \left(\frac{\partial P}{\partial z} \right) = 0 \quad (4)$$

Velocity & Separation of Variables

$$v_r(r, z) = \bar{v}_r(r) \phi(z) \quad (5)$$

$$v_\theta(r, z) = \bar{v}_\theta(r) \phi(z) + U(r) \quad (6)$$

where:

$$\phi(z) = \left(\frac{n+1}{n} \right) \left[1 - \left(\frac{2z}{b} \right)^n \right] \quad (7)$$

$$\bar{v}_r(r) = \frac{1}{b} \int_{-\frac{b}{2}}^{\frac{b}{2}} v_r(r, z) dz \quad (8)$$

Group 45 – Tesla Turbine Design

$$\bar{v}_\theta(r) = \frac{1}{b} \int_{-\frac{b}{2}}^{\frac{b}{2}} (v_\theta(r, z) - U(r)) dz \quad (9)$$

$$U(r) = \frac{r}{r_0} U_0 \quad (10)$$

Equation 1 yields that $r v_r = C_r$, and integrating it over the channel:

$$\int_{-\frac{b}{2}}^{\frac{b}{2}} r v_r dz = b C_r \quad (11)$$

Mass conservation requires that $-2\pi r_0 \rho \int_{-b/2}^{b/2} v_r dz = \dot{m}_c$, where \dot{m}_c is the mass flow rate per channel:

$$\dot{m}_c = -2\pi r_0 \rho \bar{v}_r(r_0) b \quad (12)$$

(Note: $\bar{v}_r(r_0) = \bar{v}_{r0}$)

$$\bar{v}_{r0} = \frac{\dot{m}_c}{2\pi r_0 b \rho} \quad (13)$$

Hence:

$$\bar{v}_r = -\frac{r_0}{r} \bar{v}_{r0} \quad (14)$$

Wall friction

Theta direction wall friction force for fluid element in channel between rotors with volume V_e is typically given by:

$$F_\theta = \tau_w A_w = \frac{4\tau_w V_e}{D_H} \quad (15)$$

where D_H is the hydraulic diameter of the channel ($D_H = 4V_e/A_w$). For parallel plates, $D_H = 2b$. In Newtonian fluid medium, it follows that:

$$\tau_w = f \frac{\rho \bar{v}_\theta^2}{2} \quad (16)$$

$$f = \frac{\tau_w}{\rho \bar{v}_\theta^2 / 2} = \frac{2\mu \left[\frac{\partial(v_\theta(r, z) - U)}{\partial z} \right]_{z=\frac{b}{2}}}{\rho \bar{v}_\theta^2} \quad (17)$$

For the purpose of this analysis, tangential shear interaction of the flow within the disk surface is postulated

$$f = \frac{Po}{Re_c} \quad (18)$$

where:

$$Re_c = \frac{\rho \bar{v}_\theta D_H}{\mu} \quad (19)$$

For laminar flow, $Po = 24$. To account for flow with roughened surface, an enhancement number F_{Po} was defined as such:

$$F_{Po} = \frac{Po}{24} \quad (20)$$

From the above equations, it follows that,

$$Po/8 = (n+1) = 3F_{Po} \quad (21)$$

$$\tau_w = -\frac{2\mu(n+1)\bar{v}_\theta}{b} \quad (22)$$

From the definition of wall friction term in Equation 3,

$$f_\theta = \frac{4\tau_w}{\rho D_H} = -\frac{16\mu(n+1)\bar{v}_\theta}{\rho D_H^2} \quad (23)$$

Dimensionless Variables Definition

$$\xi = \frac{r}{r_0}$$

$$\hat{W} = \frac{\bar{v}_\theta}{U_0}$$

$$\hat{P} = \frac{P - P_0}{\rho U_0^2 / 2}$$

$$V_{r0} = \frac{\bar{v}_{r0}}{U_0}$$

$$\varepsilon = 2b/r_0$$

$$Re_m^* = \frac{D_H}{r_0} \frac{\dot{m}_c D_H}{2\pi r_0 b \mu} = \frac{\dot{m}_c D_H}{r_0^2 \mu} = 4V_{r0} \frac{b^2 U_0}{r_0 \nu}$$

Applying the above definitions back to the NS equation,

Tangential ODE

$$-\frac{2n+1}{n+1} = \left[\frac{1}{\xi} - \frac{8(2n+1)\xi}{Re_m^*} \right] \hat{W} + \frac{\partial \hat{W}}{\partial \xi} \quad (24)$$

Radial ODE

$$\frac{\partial \hat{P}}{\partial \xi} = \frac{4(n+1)}{(2n+1)\xi^3} [V_{r0}^2 + \xi^2 \hat{W}^2] + 4\hat{W} + 2\xi + \left(\frac{32(n+1)V_{r0}^2}{Re_m^* \xi} \right) \quad (25)$$

Power Generation

$$T = 2\pi \int_{r_i}^{r_o} \tau_w r^2 dr$$

$$T = \left(\frac{4\pi U_0 \mu r_0^3 (n+1)}{b} \right) \int_{\xi_i}^1 \hat{W} \xi^2 d\xi \quad (26)$$

$$P_{total} = 2\omega(n_d - 1)T \quad (27)$$

Mechanical Efficiency

$$\eta_{rm} = \frac{v_{\theta 0} U_0 - v_{\theta i} U_i}{v_{\theta 0} U_0} = 1 - \frac{(\hat{W}_i + \xi_i)\xi_i}{(\hat{W}_0 + 1)} \quad (28)$$

Ideal Efficiency

$$\eta_i = \frac{v_{\theta 0} U_0 - v_{\theta i} U_i}{\Delta h_{isen}} = \frac{(\hat{W}_0 + 1) - \xi_i(\hat{W}_i + \xi_i)}{\frac{\Delta h_{isen}}{U_0^2}} \quad (29)$$

where:

$$\Delta h_{isen} = \frac{P_0 - P}{\rho} + \frac{1}{2} (\bar{v}_0^2 - \bar{v}_i^2) \quad (30)$$



4.3 Volute Casing Incorporation

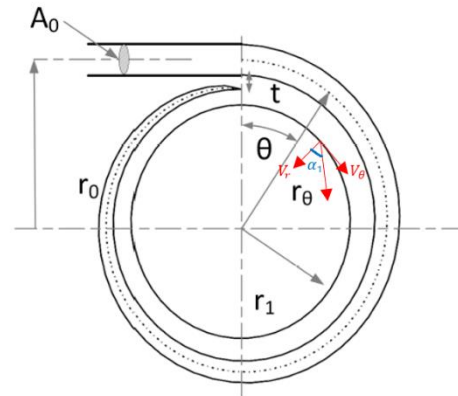


Figure 10 Schematic of volute casing cross-section.

To solve the flow ODE equations given in Section 4.2, the inlet flow velocity components must first be specified. Subsequently, the flow rate and flow velocity can be determined from casing inlet cross-sectional area. For flow components distinction at the discs' inlet, much attention has to be directed into volute geometry and size for that it governs the fluid's momentum and angle of attack.

According to Keep and Jahn's presented work, the volute geometry, shown in Figure 10 and Figure 11 was developed based on the conservation of angular momentum assumption as such, the following relationship exists for exit flow angle [66],

$$\tan(\alpha_1) = \frac{\rho_1(A_1/r_1)}{\rho_0(A_0/r_0)} \quad (31)$$

Where A_0 and A_1 represent the volute inlet area and disc side area, respectively. In incompressible flow,

$$\tan(\alpha_1) = \frac{(A_1/r_1)}{(A_0/r_0)} \quad (32)$$

Through further simplifications for this project's design geometry, the following relationship was obtained:

$$\tan(\alpha_1) = 2 \frac{wr_0}{h^2} \quad (33)$$

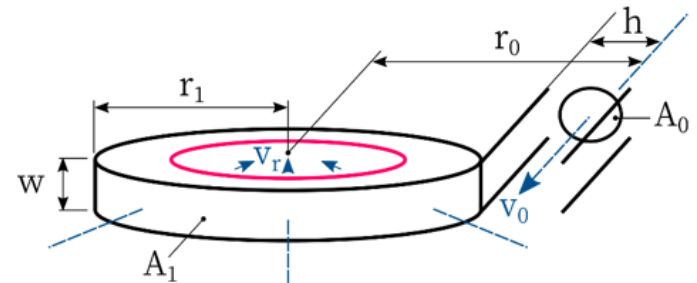


Figure 11 Isometric view of volute casing schematic.

With the above formulae, the flow angle at the tip of the discs can be determined. With the radial velocity component set following Equation 13, the flow's tangential component can then be quantified which thereafter, fully establishing the ODEs' boundary conditions.

4.4 Results

Validation Plots

Figure 12 and Figure 13 shows the flow solutions corresponding to the varying cases and initial conditions. The profiles shown are in good agreement with the analytical solutions obtained by Carey [24] and thus, validating the equations and codebase formulated in this study. One interesting observation worth noting is the dimensionless pressure drop trend as shown in Figure 12. It is apparent that rougher microstructure surface (higher F_{po}) leads to lesser pressure drop, which may seem to contradict most of what the literature has found. However, this is mainly attributed to the decreasing centripetal force as surface roughness increases, bringing about the lesser required pressure field to balance this term. Additionally, the pressure drop described here is only representative of the radial direction, whereas fluid flow has both tangential and radial components to be considered [24].

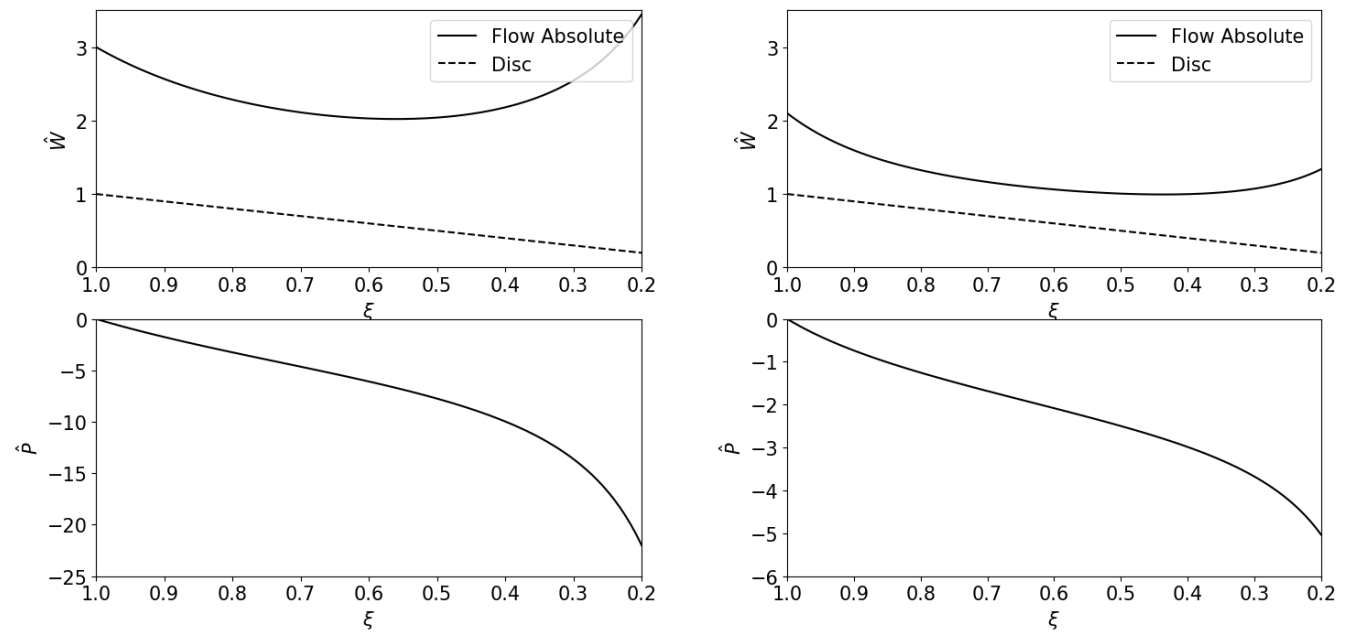


Figure 12 Solutions validation using the model developed by Carey [24]. (a) Case 1: $\hat{W}_0 = 2$, $Re_m^* = 10$, $\xi_i = 0.2$, $V_{r0} = 0.05$.
(b) Case 2: $\hat{W}_0 = 1.1$, $Re_m^* = 5$, $\xi_i = 0.2$, $V_{r0} = 0.05$.

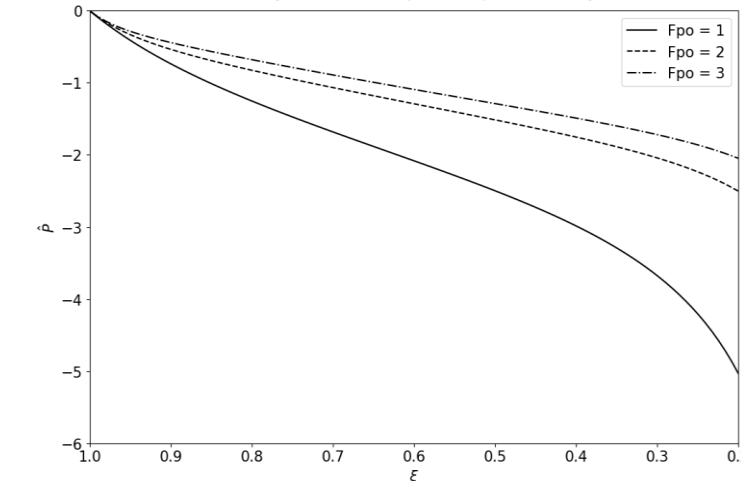


Figure 13 Dimensionless Pressure (\hat{P}) against radius ratio (ξ) under varying microstructure surfaces.
Case: $\hat{W}_0 = 1.1$, $Re_m^* = 5$, $\xi_i = 0.2$, $V_{r0} = 0.05$.



Figure 14 Basic design layout alongside variable annotations.

Model Design Optimisation

A basic structure for the Tesla Turbine was first constructed as depicted in Figure 14 to layout core design parameters for optimisation purposes. Table 5 outlines a list of variables associated with the design structure.



Table 5 Design parameters and values.

Variables	Values	Variables	Values
Mass Flow Rate, \dot{m}	1 kg/s	Inter-Disc Spacing, b	0.2 mm
Volute Outer Radius, R_0	286 mm	Disc Thickness, t_d	0.8 mm
Volute Inlet Radius, h	8.6 mm	Disc Space, w_d	7.2 mm
Volute Thickness, t	5 mm	Wall Clearance, w_c	4 mm
Disc Outer Radius, r_0	164 mm	Disc Holder Width, W	10.8 mm
Disc Inner Radius, r_i	49.2 mm	Disc Number, n_d	9
Radius Ratio, ξ_i	0.3	Flow Profile, n	2

Additionally, several design variables were bound together via the following set of relationships:

$$w_d = (n_d - 2)t_d + (n_d - 1)b \quad (34)$$

$$W = w_d + 2t_d + 2w_c \quad (35)$$

$$h = \sqrt{\frac{2}{\pi}} W \quad (36)$$

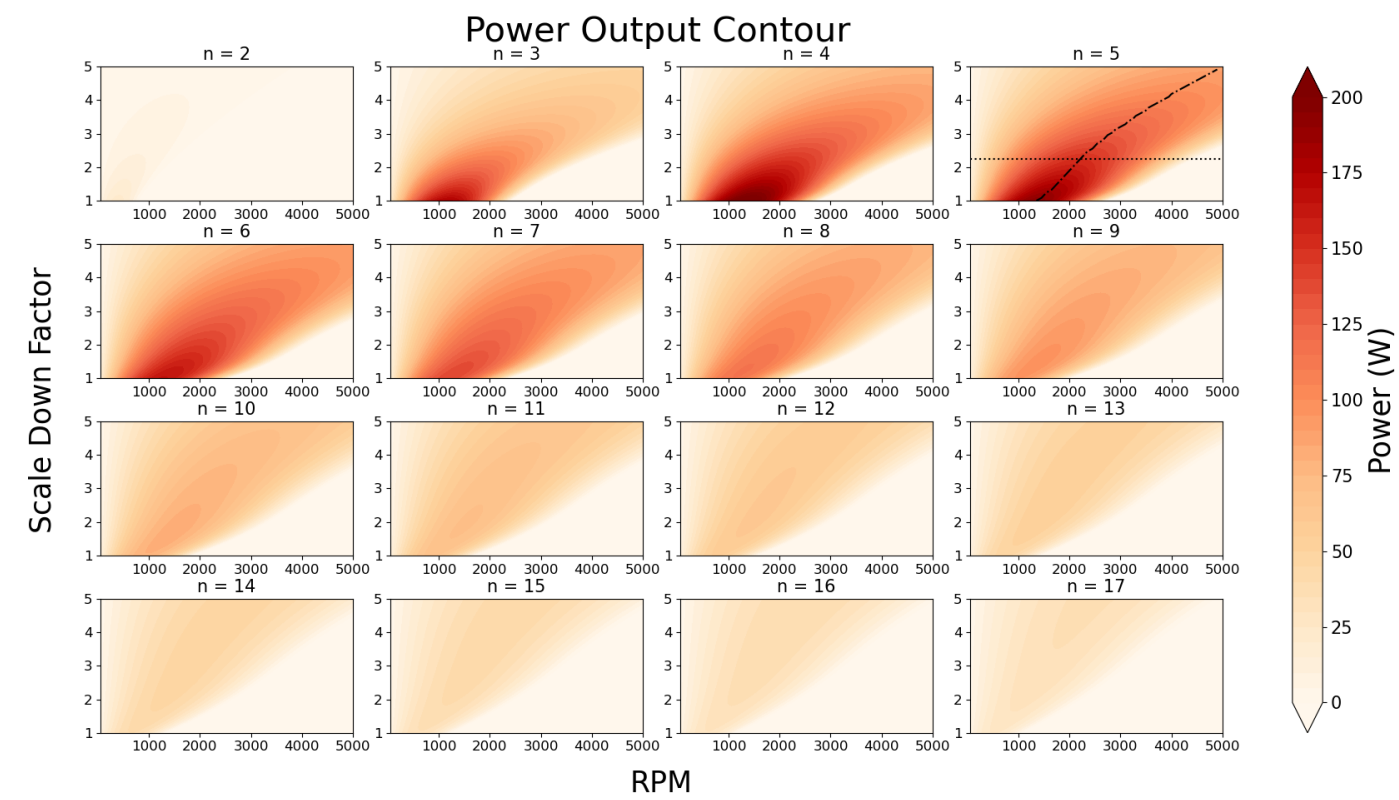
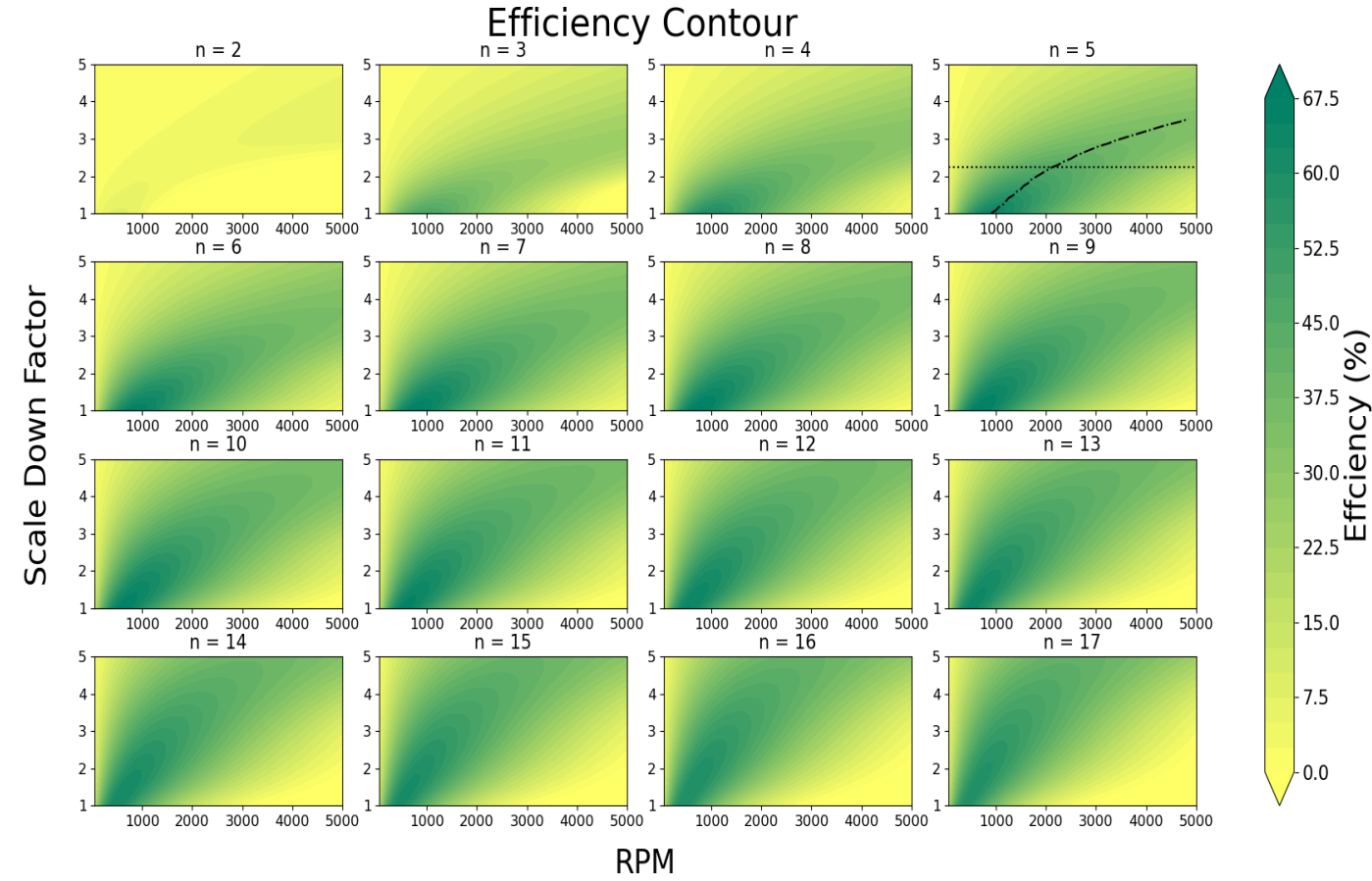
$$R_0 = r_0 + \frac{W}{2} + t + \sqrt{2Wh - W^2} \quad (37)$$

$$r_i = 0.3r_0 \quad (38)$$

These were established as a means of retaining the original design plan on top of simplifying the simulations considerably by reducing number of free variables. Using the above set of equations, the design ultimately relies on just 3 distinct parameters, namely r_0 , b and n_d . Based on previous research and analysis, turbine performance increases significantly with smaller inter-disc spacing due to the complete reliance of fluid shear force in driving the device. Therefore, a spacing of 0.2mm was fixed essentially by dint of minimising this variable as much as possible along with considering its manufacturing feasibility. Another key aspect to take note of is the radius ratio parameter, which was finalised to a constant 0.3. This was done in accord with result consistency, given manufacturable size (upper limit $r_0 \sim 164\text{mm}$) and the prevention of choked flow (lower limit: $r_i \sim 10\text{mm}$).

Under the aforementioned justifications, optimisation was carried out using parametric sweeps of n_d , working RPM and design scale-down factor, k . Due to the imposed manufacturing limitations, this study will only consider scaled down design cases.

Based on Figure 15, it is apparent that the power output saturates with increasing disc number until $n_d = 5$, before slowly diminishing off as the disc number continue increasing. This can be explained in terms of the fluid flow's angle of attack, where greater disc numbers will amount to higher casing width, and in turn contribute to the flow's angle orthogonality with reference to Equation 33. This speculation was based on the total width of the inter-disc spacing which is much smaller at lower disc number and henceforth, the radial component of the flow will be greater to fulfil mass conservation. Such occurrence will "force" the flow to be more radial directed, killing off the rotating shear drive in the tangential axis. The effect was seen to be much prominent especially at $n_d = 2$, where flow angle, α_1 was computed to be near 40° as opposed to the $78^\circ - 85^\circ$ regime for $n_d > 2$. On the other hand, the decreasing power trend observed in subsequent disc number increase after $n_d = 5$ was mainly due to the reducing tangential velocity magnitude. As the flow angle increases till a certain degree, the next limiting factor would then be the velocity magnitude per channel. Higher disc number brings about wider fluid path region, and the velocity magnitude per channel was thus, expected to decrease. Therefore, the inlet boundary condition will be lower, causing reduction in tangential shear extractions and decreasing power output.

Figure 15 Power Output Contour at varying disc numbers, RPM and scaling down factor, k .Figure 16 Isentropic Efficiency Contour at varying disc numbers, RPM and scaling down factor, k .

On contrary, the turbine isentropic efficiency does not undergo drastic value changes with disc number variations. As disc number increases, the flow rate per channel will reduce in magnitude, inducing lower momentum transfer which leads to lower pressure drop. Since efficiency is defined as the ratio of power to



the enthalpy drop, both terms will experience reductions, but at different extent in which the denominator (mainly constituted of pressure term) will be more significant. Therefore, the efficiency scale profile will be much more retained throughout as depicted in Figure 16. That aside, the turbine's efficiency contours seem to agree well with its power counterpart, consisting of similar colour-density structures and trends.

In summary, a scale down factor of 2.25 (horizontal dashed line outlined in both contour plots) at $n_d = 5$ was ultimately selected as the final design choice in light of manufacturing and performance aspects. This point was also selected as it was feasible in providing significant power output across a range of working RPM. Further on to that, the optimum rpm under each design scale was also analysed (diagonal line), indicating that the range from ~2000 - 2500 with yield the best results for both turbine output power and efficiency. Table 6 describes the parameters and turbine performance values using this design point.

Figure 17 shows the relative fluid path lines under different rpm configurations. It can be observed that at $RPM = 100$, the flow enters at a much tangential angle, and subsequently diminishes before exiting the rotor with near perpendicular profile. Correspondingly, it can be inferred that most of the fluid energy were transferred at the top half of the rotating disc; whereas at the lower half, the flow's tangential component mostly advanced concurrently with the disc speed and thus, does not contribute much to torque production. This is supported by the torque value obtained from Figure 17, which was only twice as much as that of the $RPM = 2000$ case. Looking into this, one may observe that the fluid first entered perpendicularly, and slowly picking up tangential speed as it converges into the middle section. Although the torque produced was lower as compared to $RPM 100$ case due to the lower half concentrated shear force, power generation was still much significant owing to the higher rotating speed ($\times 20$ greater).

Increasing RPM after this point will start to cause power deterioration. This was especially evident observing Figure 17 (c), where the flow entered adversely to the disc rotating direction. Such occurrence will cause opposing shear and resulting in overall torque reduction as the discs are required to "pump in" energy to account for this negative work.

Base Case Simulation

Table 6 Base Turbine Design Parameters.

Variables	Values	Variables	Values
Power Generated, W	148	Radius Ratio, ξ_i	0.3
Efficiency	44%	Inter-Disc Spacing, b	0.2 mm
Mass Flow Rate, \dot{m}	1 kg/s	Disc Thickness, t_d	0.8 mm
Rev./Min., RPM	2000	Disc Space, w_d	3.2 mm
Volute Outer Radius, R_0	94.3 mm	Wall Clearance, w_c	4 mm
Volute Inlet Radius, h	10.2 mm	Disc Holder Width, W	12.8 mm
Volute Thickness, t	5 mm	Disc Number, n_d	5
Disc Outer Radius, r_o	73 mm	Flow Profile, n	2
Disc Inner Radius, r_i	22 mm		

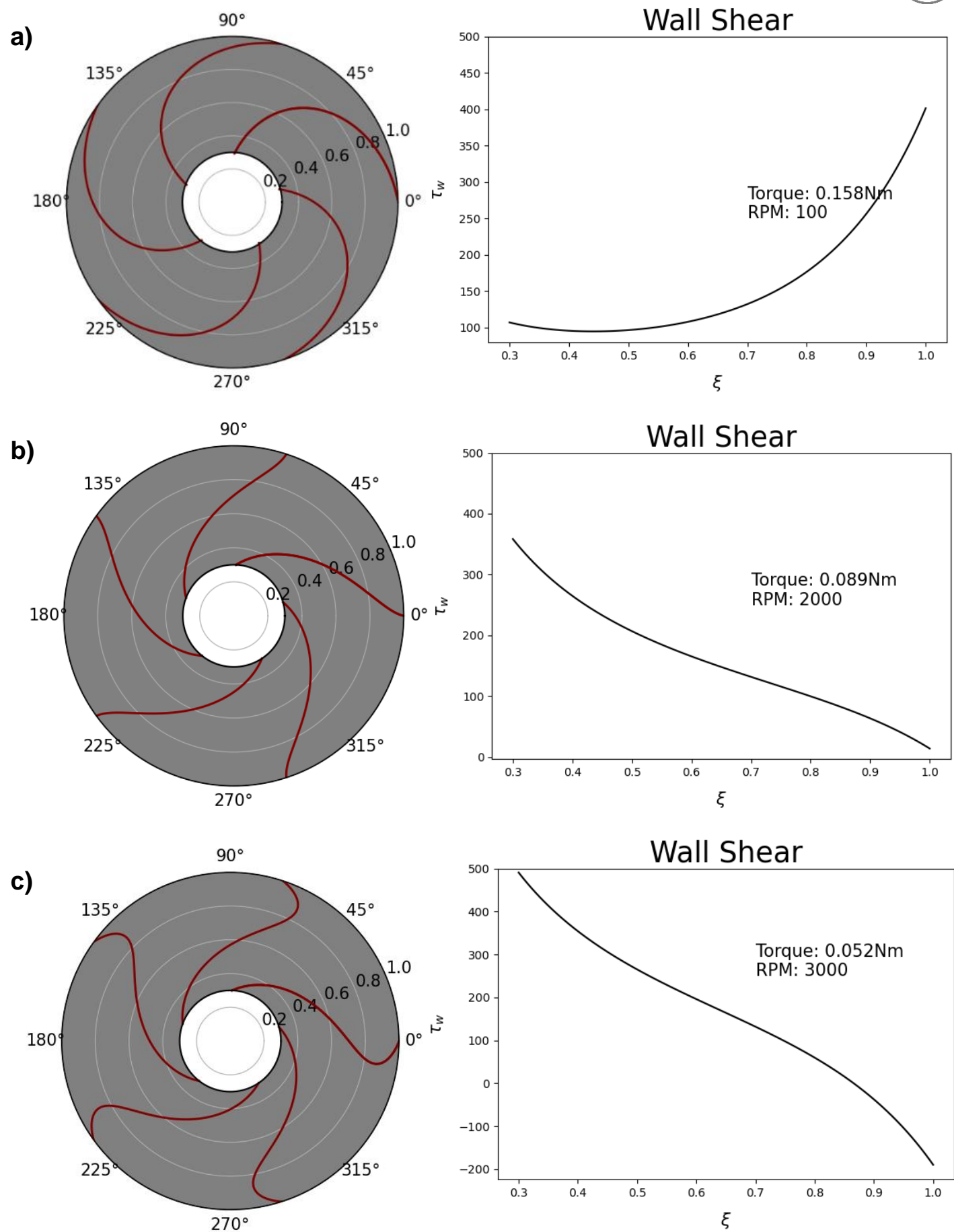


Figure 17 Relative fluid Path Lines and Wall Shear Profile at RPM (a) 100, (b) 2000 and (c) 3000.

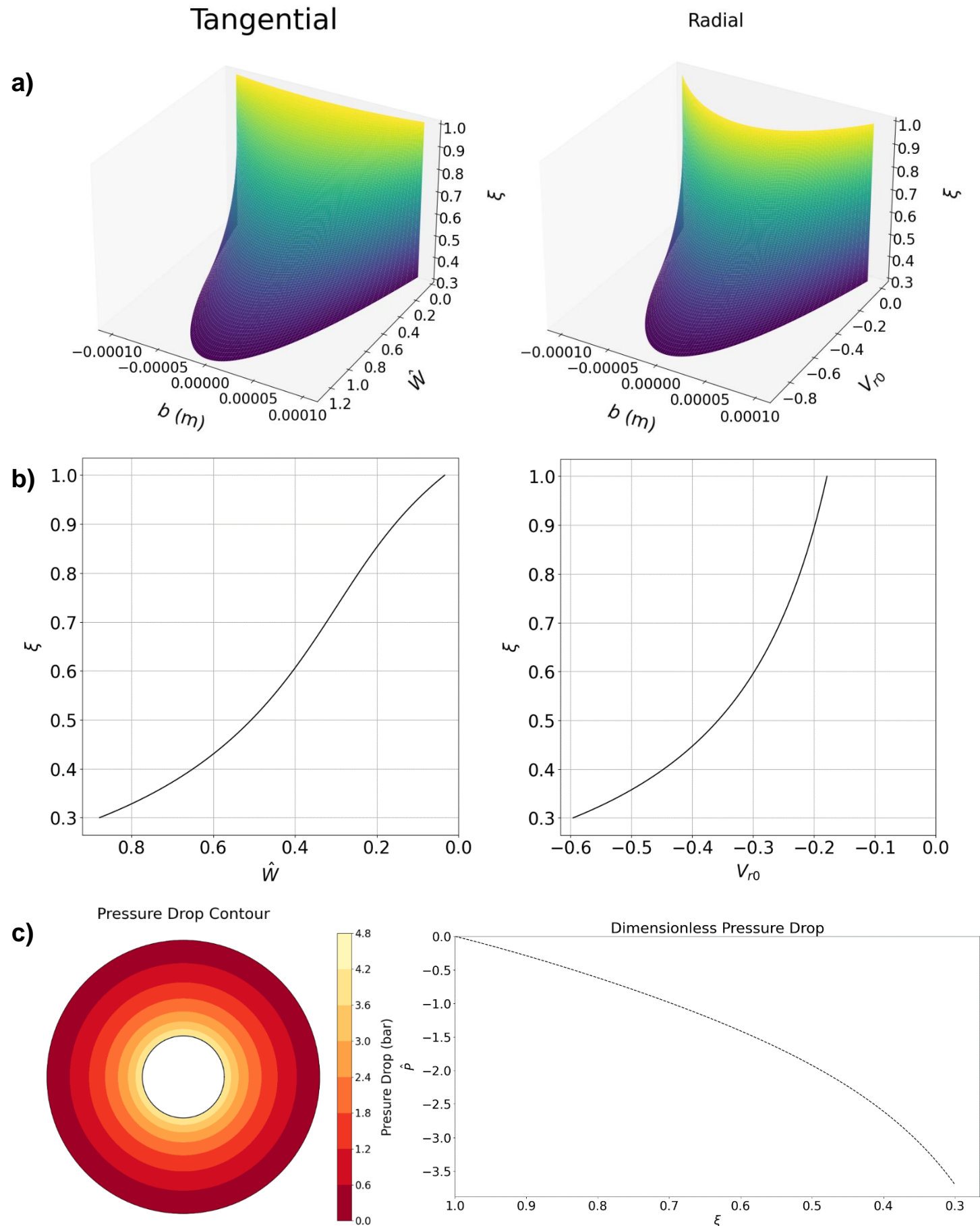


Figure 18 Base design results: (a) 3D dimensionless velocity components (b) ODE solutions and (c) Pressure drop profiles.

Figure 18 illustrates the flow and pressure transition profiles from the rotor inlet to outlet. It is evident that the tangential profile matches that closely with the shear profile depicted in Figure 19(b) since shear generation is dependent on relative motion of the fluid to the disc wall. Besides, one can also spot out the inverse trend present in the radial velocity profile due to mass flow rate conservation at any particular circular-strip area. As n was set to be a constant of 2, both velocity components showed a typical parabolic shape across the inter-disc region.

Using the settings stated in Table 6, a pressure drop of 4.8 bar is expected throughout the rotor discs, where the steepness appeared to be more significant near the disc outlet. This may be due to the increasing velocity magnitude near that area, bringing about greater overall shear and pressure losses.

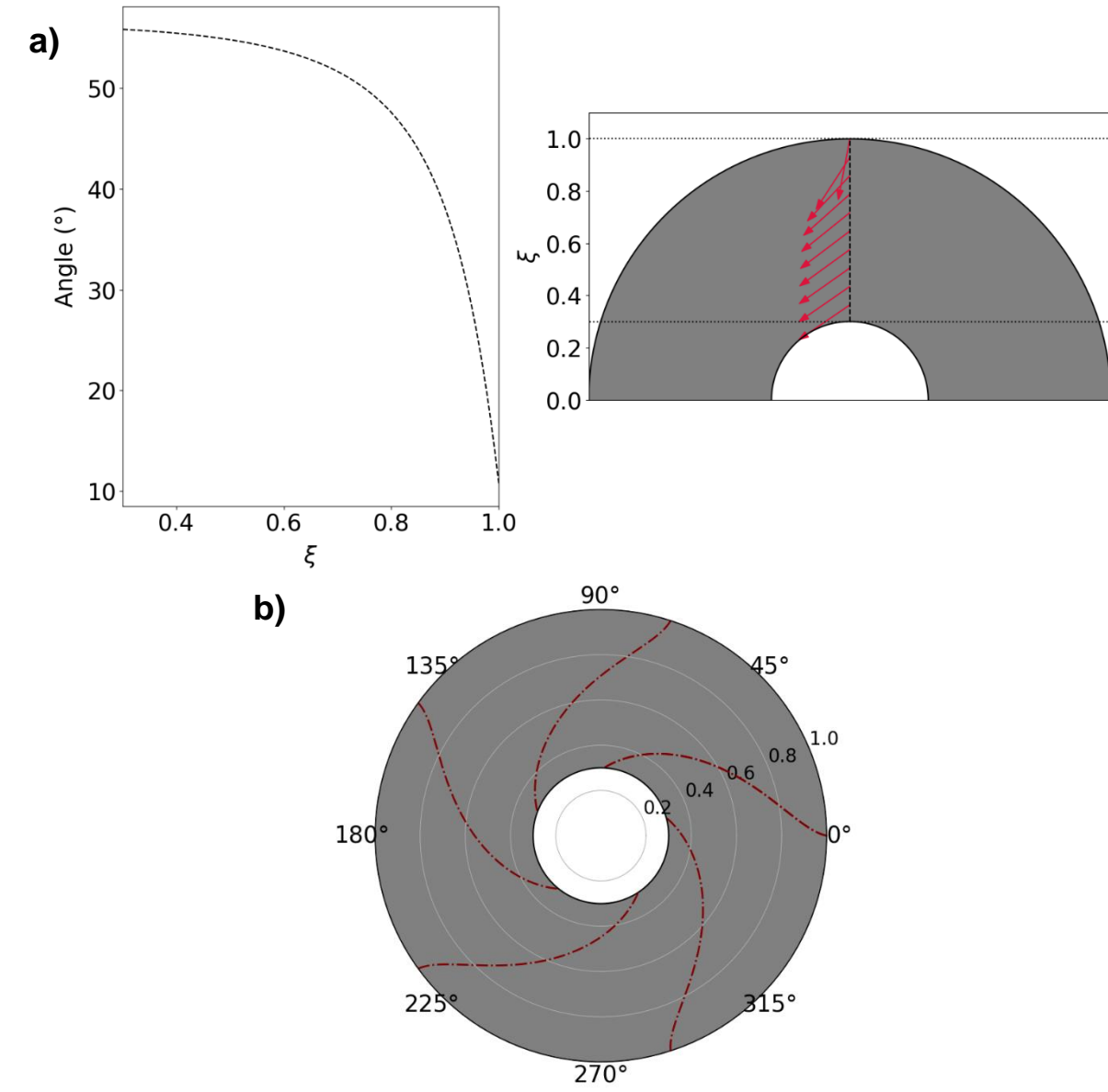


Figure 19 Relative (a) velocity angle and (b) flow path lines plots under base design settings.

K-Exponent Scaling

Further analysis on scaling was investigated, accounting for specifications such as design aspect ratio, available head and desired power density. For that, a scale function such as the following formulation in Equation 39 was derived to perform consecutive evaluations of scaling onto the turbine's overall performance.

$$b_{scale} = r_{scale}^k, 0 < k < 1 \quad (39)$$

where b_{scale} and r_{scale} represent the inter-disc space and radial scaling factors, respectively. Essentially, with the imposed k exponent limits, inter-disc scaling will always be smaller than its radius counterpart and



thus, capping the aspect ratio of the model. For this segment, the inner disc radius, r_i was set as a constant (22 mm) in consideration of choked flow occurrence as mentioned in previous sections.

Figure 20 provides the turbine's power output and density profiles under the scaling equation's effects. Note that the power density definition is given as the ratio of turbine output to its scaled volume. The obtained

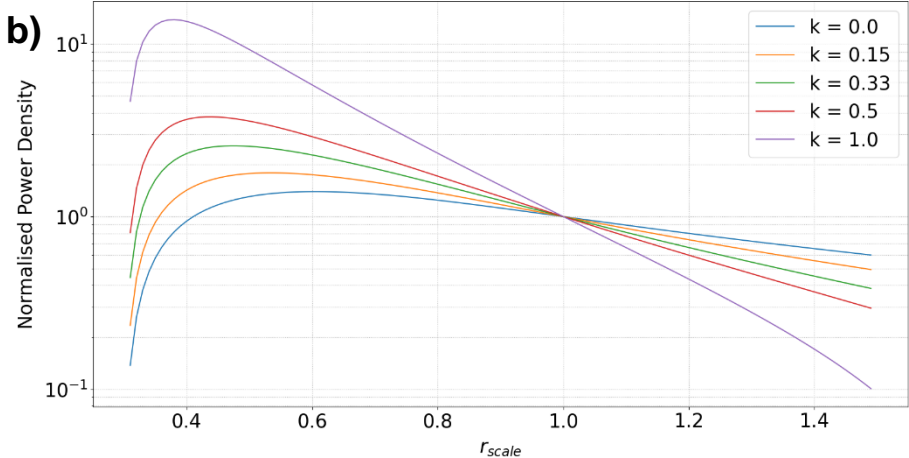
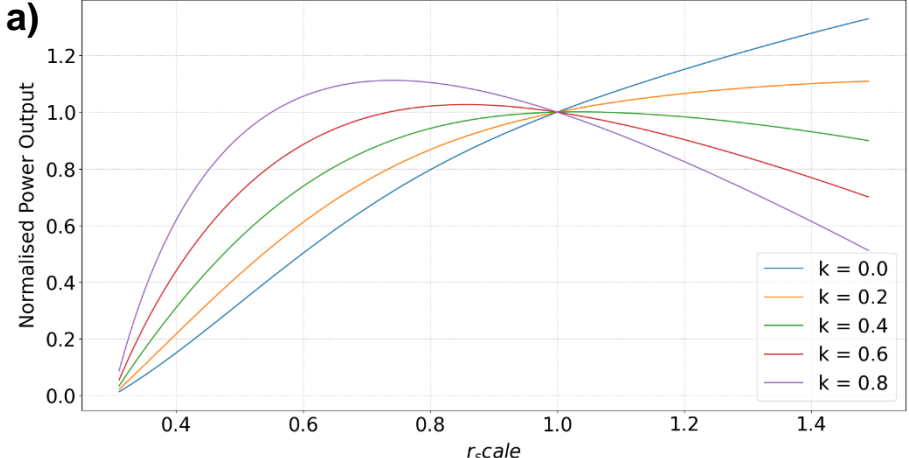


Figure 20 Graphs of (a) Normalised Power Output and (b) Normalised Power Density against Radial Scaling Factor.

results were all normalised using the base case reference output (148W) for better comparison indications. From the above plots, the maximum power curve for each line appears to be more right shifted with every successive decrease in k exponent value. This was mainly due to the inter-disc spacing, which plays a huge role in determining the tangential component contributing for shear output. At higher k exponent, one can expect the disc spacing to be more separated as r_{scale} increases, thus reducing the velocity magnitude per disc channel owing to mass conservation. This in turns affects the tangential component to reduce as well and thus, giving smaller boundary layer to inter-disc space proportion which enables more flow to pass through the middle section area. However, the observed initial increasing trend may be attributed to the area exposure for fluid shear, where higher radial scaling implying higher contact surface area.

The power density profile on the other hand, seemed to exhibit more drastic trend changes, especially so when $r_{scale} < 4$. This was expected because the power outputs were reduced to near 0 value, proving the turbine's infeasibility for power generation due to reducing disc height. Aside from that, the values for all exponent lines were also observed to peak at $r_{scale} \sim (0.4 - 0.6)$, before decreasing steadily as r_{scale} continue to rise. It also apparent that any means of scaling up after the base design point reflects poorly on the density curve graph, suggesting that power output does not scale proportionally with turbine size/manufacturing cost. Using the above plots, the optimal solution for turbine design lies in the region where $r_{scale} < 1$ and $k > 0$. This however, present a practical limitation where inter-disc spacing would have to be smaller than the current value (0.2 mm), and can potentially cause unwanted instances such as adjacent discs rubbing. Therefore, taking the blue line as the main reference bar (constant disc spacing), the value for peak power density take place at $r_{scale} \sim 0.6$ and can be deemed as the optimal setting. Nevertheless, the mentioned point may not be suitable as it compromises a lot on the net power output (~70W). Hence, with these considerations in place, the base design point still emerges as optimum for this project's applications and does not necessitate any changes.

This section provides a comprehensive overview and walkthrough of the model construction, followed by volute incorporation and further on to design optimisation. The optimised design and all its relevant parameters were listed down in Table 6. From the results obtained in further numerical analysis, it is apparent that higher performance turbine may be achieved with smaller inter-disc spacing, indicating a potential design improvement avenue for future studies.

5 CFD Model

5.1 Background

There has been extensive research and the use of CFD analysis into evaluating the performance of turbines and pumps with volute casings designs. For instance, Yang *et al.* studied the effects of geometric changes in the volute throat area, cross-sectional shape, radial gaps etc. on turbine's performance [67]. Flow analysis of multivolute casings using CFD have also shown that radial forces can be minimized using higher volute number, where the triple-volute provides the highest head at low capacity and the lowest radial forces [68]. However, Ojeda *et al.* found that at higher flow rates, turbines with greater volute numbers exhibit decreased performance due to increased boundary layer friction [69]. Similarly, lower flow rates attributed to increased performance as recirculation regions can be controlled better. Fluid behaviour within axial turbine blades were predicted using CFX to show that flow patterns inside the turbine space can be optimized with 3D viscous flow simulation using the SST $k-\omega$ turbulence model [70].

The performance of Tesla Turbines using water as the fluid has also been investigated. Tan *et al.* optimised disc size, disc gap, and number of discs using CFD, discovering that a home based Tesla Turbine (pipe water as inlet) was able to generate a torque of 0.021 Nm with an efficiency of 6.8% [46]. CFD has also been used to evaluate mass flow changes on Tesla Turbine efficiency, showing changes in power and efficiency from inlet flow velocities [71]. Pandey *et al.* studied the Tesla Turbine power output versatility using CFD when water was used as a medium, achieving 777.16 W and efficiency of 77.7% under a mass flow rate of 7.28 kg/s [72]. Furthermore, Rusin also found that the turbine output geometry had a significant influence on the power output. This was shown to be largely due to the presence of swirls and backflow that decreased the generated power [43]. The effects of nozzle design (number of nozzles and angle of each nozzle) was evaluated by Romanin *et al.* and showed that CFD models were able to predict the flow field under varying test configurations. Computational results also verified that lower flow rates and smaller gaps led to higher efficiencies [47]. A hybrid Tesla-Pelton wheel turbine was also put forward by Joshi *et al* and Khan *et al*. It was shown that by combining impulse forces by the Pelton wheel and boundary effects of the Tesla Turbine, a higher power output can be achieved [33], [73].

Tesla Turbines are usually categorized as voluted or nozzled [32], with more limited reports on voluted. Lemma *et al.* studied flow characteristics and loss mechanisms for voluted Tesla Turbines, showing isentropic efficiency of 38.5% if bearing losses, end wall viscous losses, and parasitic losses were minimized [55]. Previous research paid much attention to using CFD as a tool towards improving the efficiency and performance of volute and turbine systems separately, but none have addressed the fluid dynamics when coupling a volute casing to a Tesla Turbine.

5.2 Goals

Initial CFD simulations were carried out to check for the flow field performance within the turbine test models. This would include recirculation regions and pressure drop investigation across both the turbine and disc regions. For every design iteration and concept, CFD was used to consult on design changes to be implemented. In the final design, CFD was employed to refine the volute casing geometry, preventing sudden drops in pressure and recirculation regions. More importantly, the flow variables were compared to that of the analytical model for validation purposes.

5.3 Methodology

5.3.1 Pre-processing

All models were prepared within SOLIDWORKS before exporting them as a .STEP file into ANSYS. Within ANSYS, the DesignModeler volume extract function was used to model the inner flow domain of both the volute casing and disc. Subsequently, the flow domain was then realigned to the origin using SpaceClaim to ensure accurate extraction of relative flow variables later on. For all cases, the central outlet region of the disc was not modelled, this is shown in Figure 22. The new outlet was set to be at the location where the flow directly exits the inter-disc region.



5.3.2 Mesh

Due to high model complexity, the final model was split into two separate parts for CFD modelling – the volute casing and inner disc rotation region. Mesh cell quality was ensured to be higher than the minimum orthogonal quality criterion within FLUENT for all cases. If left-handed mesh was reported, the case was remeshed. ANSYS - FLUENT was used to generate an unstructured mesh grid for the outer casing while a structured grid was used for the discs.

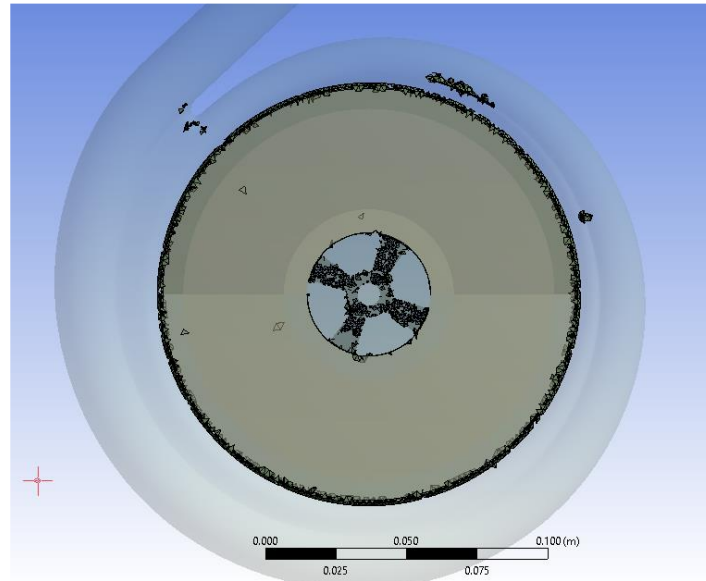


Figure 21 Black shaded cells represent low quality elements due to a disparity in edge length with adjacent cells. Special attention was given rectify this, as simulation results were largely inaccurate.

components together, the process of increasing inter-disc cell number while maintaining cell quality was proven challenging, i.e. orthogonal quality decreased to 3.2 E–10 despite the increased cell number. Due to these reasons, the turbine was simulated as 2 separate cases.

5.3.3 Mesh convergence methodology

A mesh independence study was carried out by evaluating changes in the flow field variables over different element numbers. We estimated changes in the azimuthally averaged absolute pressure, velocity angle, and velocity magnitude across approximately 486733, 892335, 1640699, 1909415, and 2355353 elements for the volute case. For the disc simulation, the number of elements were increased by varying the number of elements in the inter-disc space while fixing the number of cells in the radial direction to 25 elements. Inter-disc mesh convergence analysis was carried out for 244500, 590400, 894600, 1197600, and 2208000 elements, which translates to 5, 12, 18, 24, and 30 cells within the inter-disc space respectively. The azimuthally averaged shear stress across all discs were compared. Shear stress plots were analysed within Matlab for determining the best fit gradient via principle component analysis (linear regression). Finally, the percentage differences for absolute pressure, velocity angle, velocity magnitude, and shear stress gradient were tabulated and compared.

The convergence criteria were set to 10^{-3} for all simulations, including cases used for convergence evaluation. The flow data evolution for all cases were then compared for choosing the optimal mesh settings. As for the volute casing, outlet data was recorded using the profile extraction function within FLUENT. Flow field variables across all outlet nodes were averaged. To evaluate the inter-disc shear stress evolution radially, a command line (plot > circum-avg-radial > wall shear > wall > 25 elements) was used to extract the shear stresses across all 25 elements.

5.3.4 Outer volute casing mesh

Mesh refinements at the volute casing were mainly focused near the outlet region, where flow variables were expected to change drastically upon impinging onto the disc. Mesh independence analysis was conducted

by changing the cell refinement near the outlet. The final mesh used had a minimum cell quality of 0.098. Figure 22 shows the outer volute mesh.

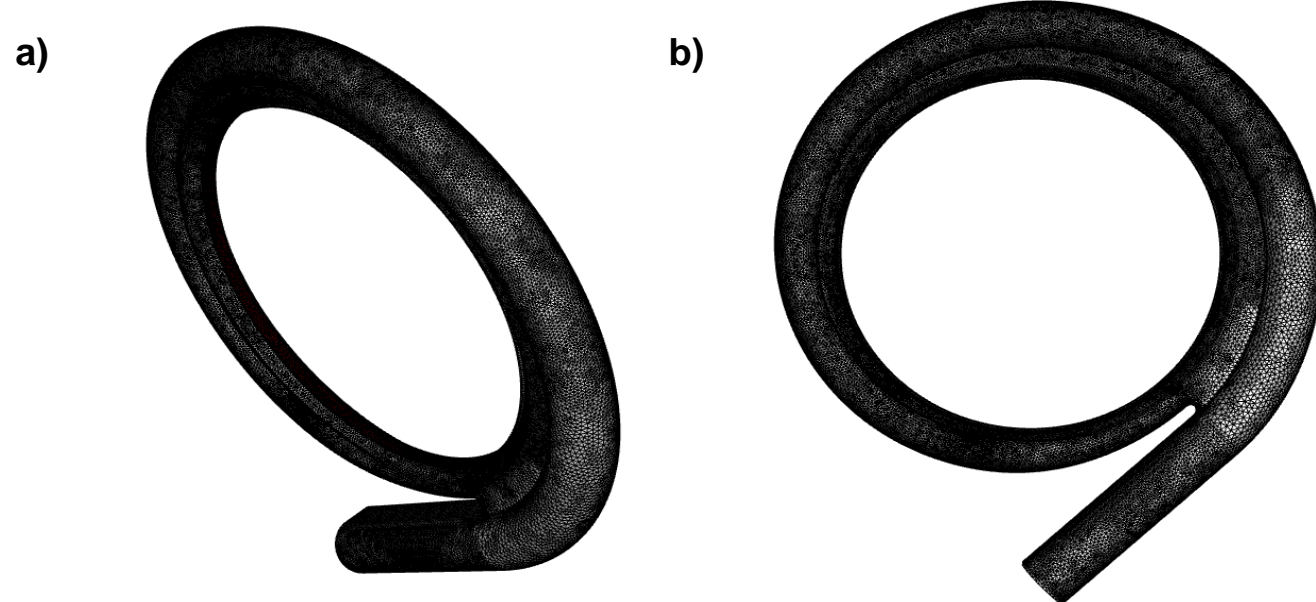


Figure 22 (a) and (b) show the casing mesh from an orthogonal and frontal perspective respectively. The entire domain is comprised of 1,640,699 elements. The mesh was generated from tetrahedral elements.

5.3.5 Inner disc region (inter-disc) mesh

Mesh refinement was carried out in between the discs. 24 cells were modelled in between the discs to ensure sufficient definition of the flow profile. Figure 23 shows the discs' mesh.

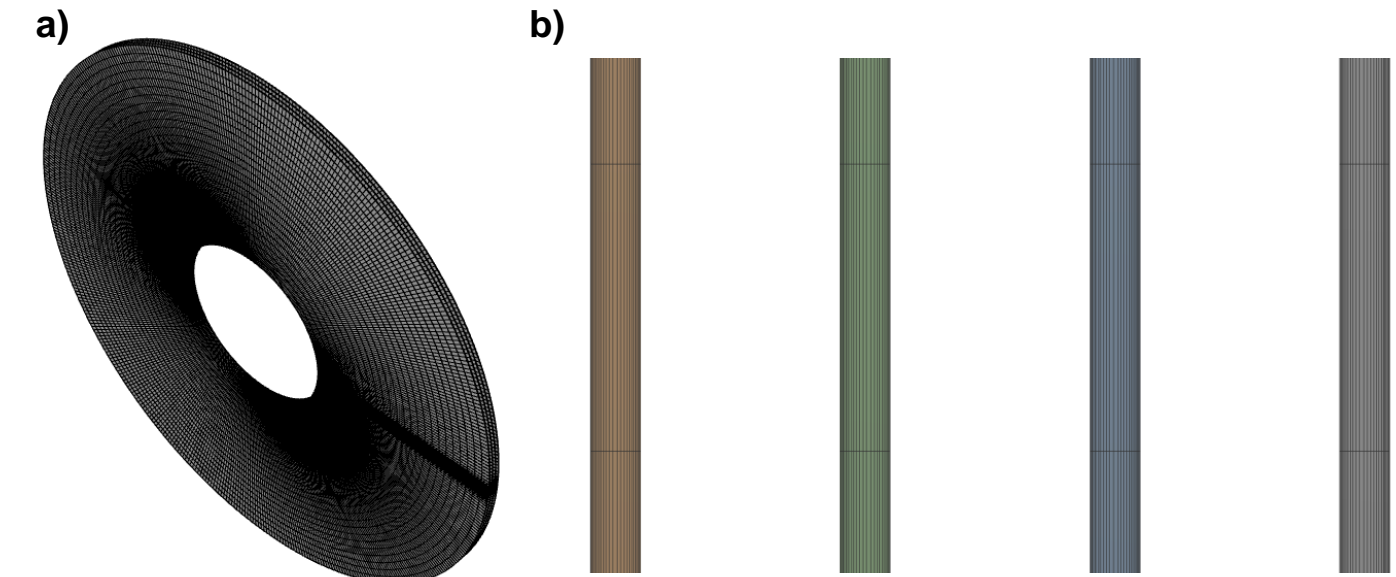


Figure 23 (a) The disc mesh was modelled to be as structured as possible to reduce the number of cells while keeping cell quality high. The structured characteristic simplifies the data extraction process as well. In (b) we observe that a mesh bias was imposed within the inter-disc region, where the cell size is smaller closer to the disc walls. Cell wall refinement ensures that changes in the flow profile due to the no-slip condition is represented as accurately as possible. The thin radial refinement region in (a) was due to a mesh bias implementation, but does not have any quantifiable effects on the flow data.

The cell size was made smaller near the wall to decrease the first cell y^+ and was further refined until the wall y^+ was either below 30 or above 300 as required by the $k-\epsilon$ model. Based off Figure 24, the final y^+ ranged between 0.9 – 2.2 in the simulation, ensuring sufficient resolution of the first cell layer to resolve the flow profile within the viscous sub-layer. It is of vital importance to keep the first node of the mesh within the log-law layer, making it necessary to increase the number of elements near wall. The number of elements



can be reduced outside this boundary layer, ensuring convergence with fewer iterations and reduced computational time [74].

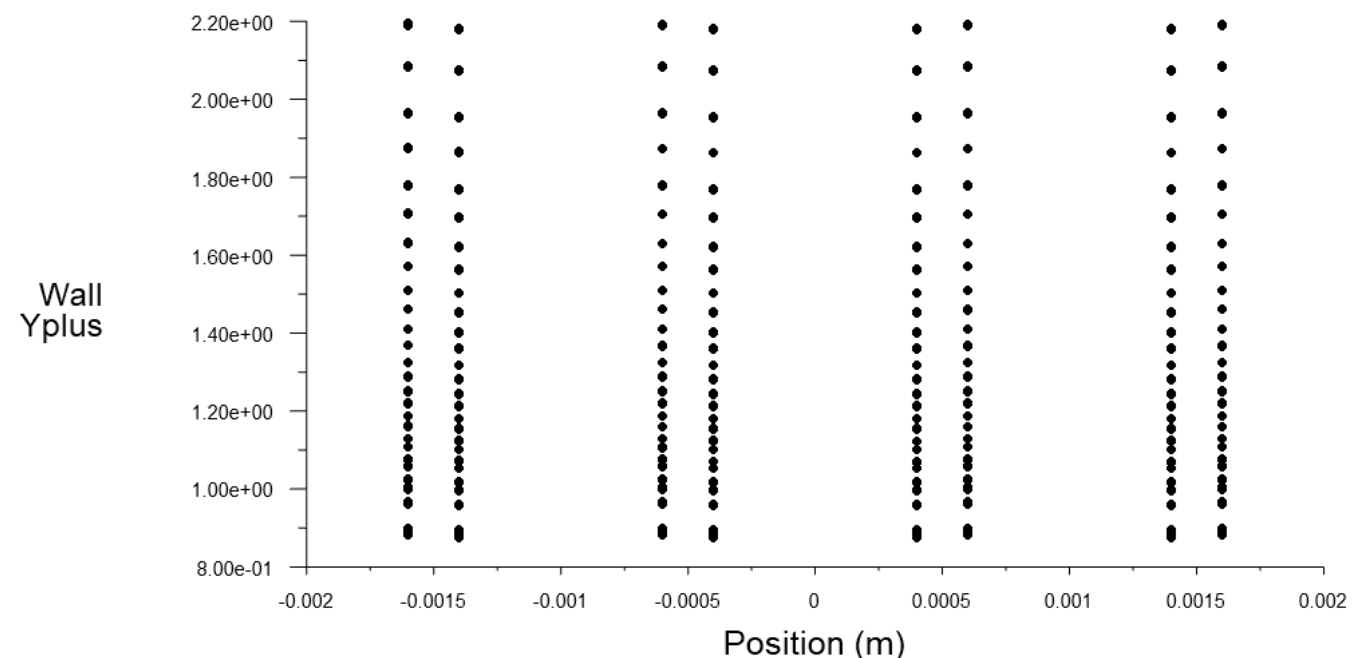


Figure 24 y_1^+ is plotted across all elements in contact with the wall layer. Each vertical line represents a wall region. Because the mesh is a structured one, we observe that the y_1^+ does not exhibit much variation across the discs.

5.3.6 Processing

Because the domain was decoupled into two parts, it was challenging to estimate the initial boundary conditions for both simulations. Therefore, estimates of the boundary variables were determined by first running a simulation of the whole turbine with inlet conditions set to 1 kg/s, outlet set as a pressure outlet at 0 gauge, and disc RPM at 2000. Absolute pressure, velocity magnitude, and velocity angle information were recorded and used as the initial estimate for the separate simulation cases. Table 7 shows the inlet and outlet conditions.

5.3.7 Solution parameters and boundary conditions

Turbulence was simulated using the standard k- ϵ model to ensure sufficient resolution of the flow field while keeping the simulation computationally cheap. Enhanced wall function was turned on for both simulations, blending separate wall models in the two-layer approach by use of a damping function so that the transition between wall models are smoother. Adiabatic, non-slip wall condition was also applied for the solid wall surfaces. The flow field was initialized using hybrid initialization, with a convergence tolerance set to 10^{-6} over 10 instances. For all cases, the final initialization converged to at least 10^{-8} .

The volute casing outlet was set as a mass flow outlet so that pressure and velocity variables can freely evolve. Directly superposing the volute outlet profile as the inter-disc inlet proved to be challenging, therefore absolute pressure, velocity magnitude, velocity angle, and velocity components (radial, axial, and tangential) were recorded for every iteration. Upon convergence, these variables were averaged and used to set the new inlet. A user defined function (UDF) was initialised for setting the new tangential, radial and axial velocity components along with the absolute pressure. Relaxation factors were changed from the default to values in accordance with the FLUENT handbook if mesh refinement were not to yield convergent results.

Table 7 Fluent simulation setup conditions for both the volute casing and disc. Variables not tabulated below were kept at the default value.

	Outer volute casing	Rotating disc region
Turbulent model	Standard k - ϵ	
Wall function	Enhanced	
Fluid type	Water – liquid	
Wall motion	Stationary	Moving wall

Speed (rad/s)	-	209.4395
Rotation Axis	-	Z- Axis
Inlet boundary type	Mass flow inlet	Mass flow inlet
Inlet mass flow (kg/s)	1	1
Inlet gauge pressure (Pa)	100000	99394.01091
Inlet turbulent intensity	-	0.0331
Radial flow component	-	-0.145
Tangential flow component	-	0.89
Axial flow component	-	0.00351
Outlet boundary type	Mass flow outlet	Pressure outlet
Outlet mass flow (kg/s)	1	-
Outlet gauge pressure (Pa)	-	0
Outlet turbulent intensity	-	0.0331
Relaxation factors		
Pressure	0.2	0.5
Turbulent kinetic energy	0.5	0.75
Turbulent dissipation rate	0.5	0.75

5.4 Results

5.4.1 Mesh convergence analysis

Table 8 below tabulates the absolute percentage changes for the tracked variables. Convergence analysis shows a large deviation for all three variables at lower mesh resolution. Velocity magnitude observed the largest fluctuations (41.4 %) while velocity angle remained approximately the same. The percentage difference observes a decrease from 1.6 million cells onwards, while further mesh refinement resulted in diminishing returns. Difference in velocity magnitude were all lower than 10% despite much longer computational times. For this reason, 1640699 elements were used for the final model.

Table 8 Pressure, velocity magnitude, and velocity angle differences were compared for the volute casing. Best fit regression gradients for shear stress were plotted and compared for the discs.

Volute casing			
Elements	Absolute percentage difference		
	Pressure	Velocity magnitude	Velocity angle
486733 - 892335	1.81611	41.40666	0.28695
892335 - 1640699	3.783938	28.8819	0.269785
1640699 - 1909415	0.356973	6.710937	0.410348
1909415 - 2355353	0.11478	5.392684	0.35958
Disc			
Elements	Regression gradient	Elements	Gradient absolute percentage difference
244500	6.5152e+03	244500 - 590400	15.06
590400	7.4967e+03	590400 - 894600	14.19
894600	8.5604e+03	894600 - 1197600	2.25
1197600	8.7532e+03	1197600 - 2208000	0.13
2208000	8.7414e+03		

The percentage changes reported were compared between the two subsequent points only. However, from Figure 25(a, b), we observe that pressure and velocity angle for 1640699 and 2355353 elements are approximately the same. Further justifying the use of 1640699 elements.

For the inter-disc mesh, a larger deviation was observed for cases with less refined cells, similar to that observed for the volute casing. From Table 8, 894600 onwards, the gradient difference only varied by around 2.25% with a 200,000-element increase. At 2.2 million elements, the gradient difference only amounted to a



diminishing return of 0.13%. Figure 25 (d) clearly shows the similarity in shear stress variation despite the large element number increase.

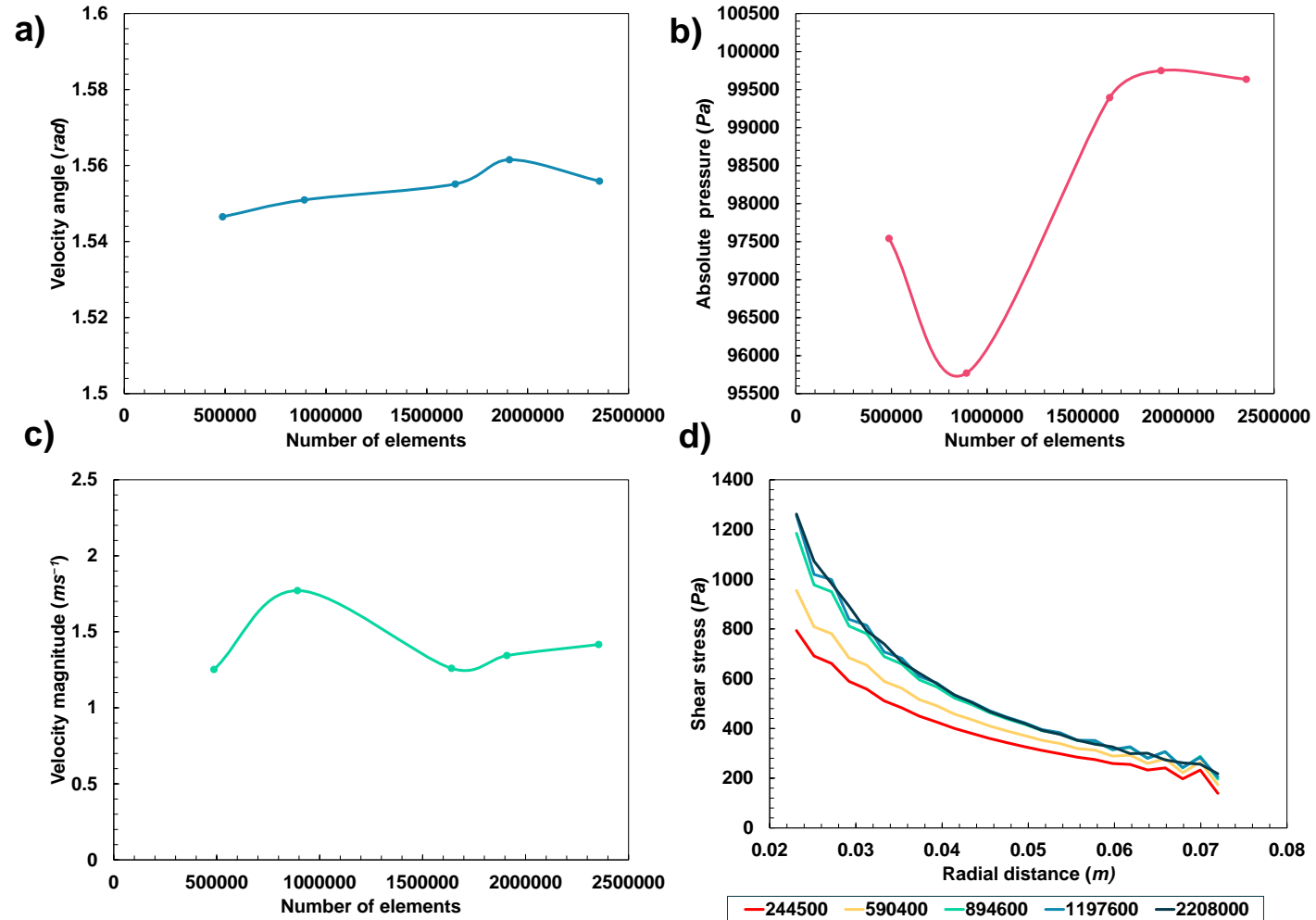


Figure 25 (a), (b), and (c) represent the azimuthally averaged pressure, velocity magnitude, and velocity angle respectively at the volute casing outlet. (d) shows the azimuthally averaged shear stress variation in the radial direction for the disc simulation, an average of all four discs were taken into account. Different colors represent variation in the total element number by changing the number of interdisc elements.

5.4.2 Performance evaluation using CFD

5.4.2.1 Volute casing

The usual industrial practice when deciding the volute cross-sectional shape is to find the best compromise between the desired performance and installation requirements. In most cases, installation takes precedence and performance is sacrificed. Therefore, understanding the volute influence on turbine performance is paramount [1]. For instance, by changing the volute area-to-radius ratio, Yang et al demonstrated an improved cycled average volute efficiency under pulsating flow conditions [75]. However, only steady state solutions were conducted in this analysis, therefore pulsating flows were not optimised for. In this study, the volute was designed to converge the flow into the disc region while keeping the volute-disc interface pressure as stagnant as possible. Because the main source of losses for Tesla Turbines usually occur at the inlet supply system (due to shock waves, overexpansion, overcompression, nozzle efficiency drop) [76], [77], much consideration was given when working towards the final design.

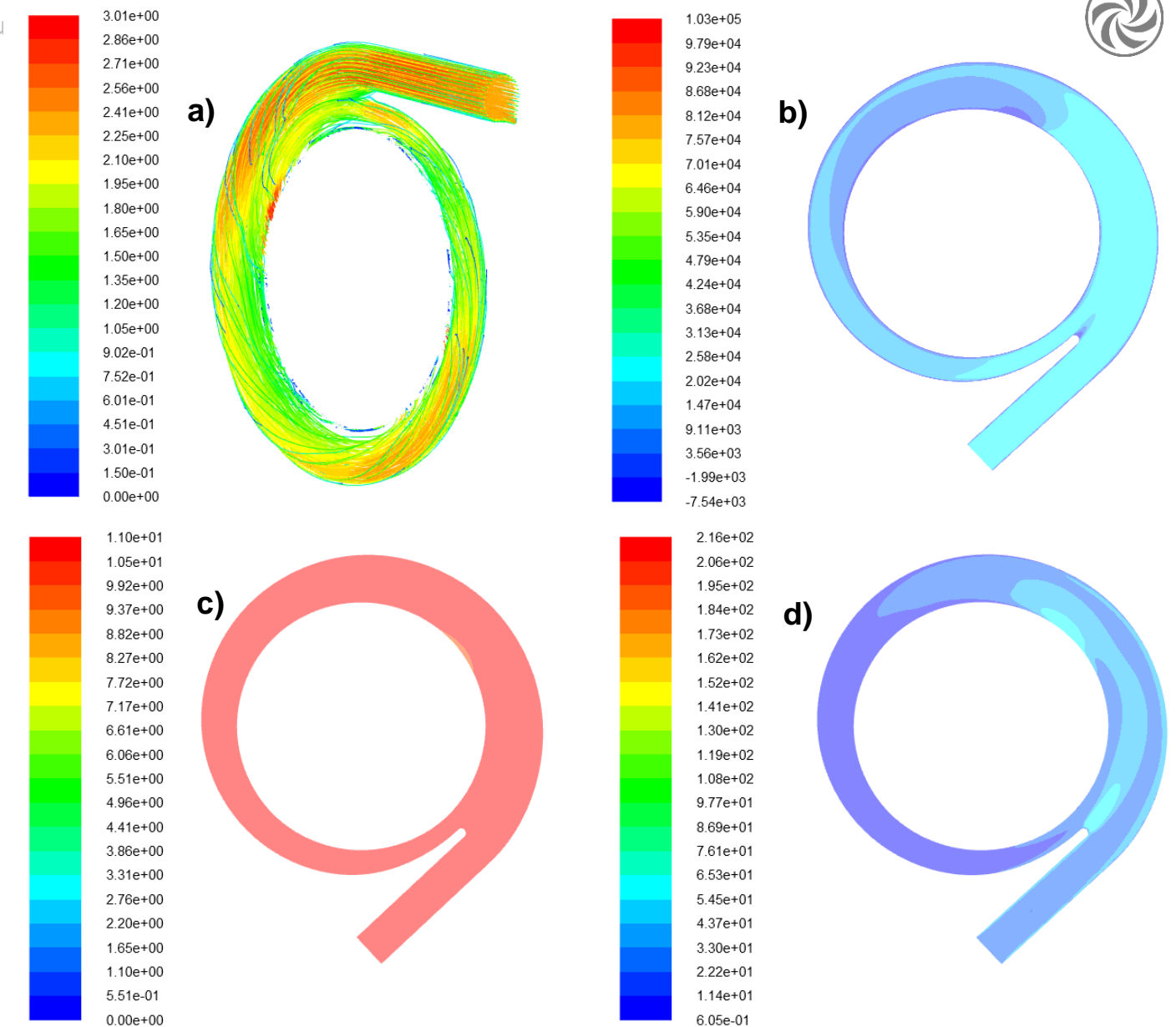


Figure 26 (a - d) show plots for the final volute casing model. (a) shows a 3D velocity pathline plot within the volute casing. (b - d) shows contour plots for velocity magnitude ($m s^{-1}$) absolute pressure (Pa), and turbulent intensity respectively. Contour plots were extracted along the central plane of the volute casing.

The volute casing design was optimised to ensure uniform pressure and velocity distribution. Figure 26(c) shows a relatively equal distribution of pressure, extracting pressure data directly from the inlet and outlet, the absolute pressure was found to be 1 and 0.957 bar (gauge) respectively, resulting in a pressure drop of 4.3% across the volute casing. In addition to this, the overall volute geometry was optimised numerous times using Equation 31 -33 to achieve a more tangential velocity angle at the outlet. From the outlet profile, the final volute casing was directing fluid at an average angle of 88.702°; close to that of being exactly tangential.

Several changes were made to the volute casing since the first iteration. The inner taper angle was changed to direct flow into the inter-disc spacing with less impingement onto the side walls (therefore reduced frictional losses). The tongue section of the volute was made shaper to prevent the formation of adverse pressure gradients as much as possible. Miller et al. showed that highest pressure losses were recorded at the tongue, with a loss coefficient value of 0.56 [78]. However, due to constraints imposed by the volute equation, the tongue width could only be reduced to a minimum before losing the volute geometry.

However, it was observed that just after the inlet, a small region near the outlet experiences lower pressures. Comparing this finding with data obtained from the velocity magnitude plot in Figure 26(b), we found a small recirculation zone near the tongue region of the volute despite numerous design corrections. Directly upstream of the region where low pressure was detected, a transitional region from high to low velocity was observed; fluid velocity decreased from 2.3 – 0.3 m/s over a short distance. The turbulent intensity (ratio of



standard deviation of fluctuating fluid velocity to mean fluid velocity, representing the intensity of velocity fluctuations) plot from Figure 26(d) shows larger velocity fluctuations downstream of the volute tongue and nearing the low-pressure region. For simulations taking both volute and discs into account, this sudden decrease in velocity was not observed. This may be attributed by an inaccurate representation of the outlet boundary, but the use of alternatives such as pressure outlets and outflow boundaries still did not result in convergence.

It was hypothesised that the increased mass flow rate when the flow field converges at the tongue region forces fluid into the volute outlet. This sharp pressure gradient affects instantaneously the rest of the thermodynamic parameters as well as the structure of the free vortex flow into the outlet. Similar results were reported by Meghnine et al, showing flow accelerations in the tangential and radial direction downstream of the tongue, producing non-uniform acceleration at the outlet in the radial direction [74]. From Figure 26(a) the occurrence of swirl within the volute can be observed. Tangential inlets have been shown to present more uniform inlet velocity profiles in the axial and circumferential direction but experience slightly larger swirl. That being said, the increase in swirl goes with a more uniform flow with vortices [79]. Future designs could implement vanes to better distribute the flow field, while having a higher tolerance and robustness towards pulsating and non-uniform flows [80].

5.4.2.2 Disc – Performance, flow characterisation and validation

Disc performance was quantified by investigating the flow profiles in the radial and tangential direction. Because the simulation inlet boundary was an average of that from the volute outlet, the velocity and pressure profile were radially uniform as shown in Figure 27(a) below. The outlet was set at zero gauge to simulate flow under atmospheric conditions. Despite not modelling the entire outlet geometry, previous simulations testing for outlet geometry effects still show zero gauge nearing the inner disc radius, justifying this geometry simplification. Figure 27(b) shows that velocity magnitude decreases at a higher rate near the outer radius while observing a slow linear increase at the middle disc region.

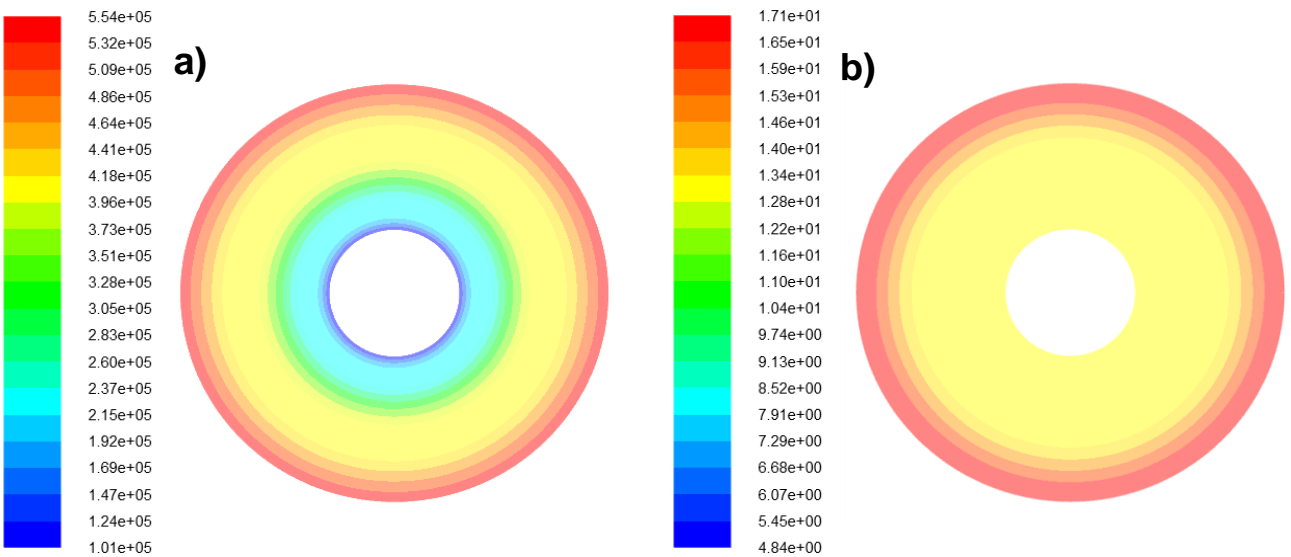


Figure 27 Contour plots were taken from the second inter-disc spacing. (a) shows the absolute pressure plot in Pa while (b) shows the velocity magnitude in ms^{-1} .

Pressure drop plot

The pressure drop across the rotor discs was evaluated to be similar in shape to that of the numerical model. The pressure was uniform in the azimuthal direction and in the axial direction. XY-plots, shown in Figure 28 were obtained by averaging the pressure across the surface in the azimuthal direction so that the pressure drop could be studied against the radius of the disc.

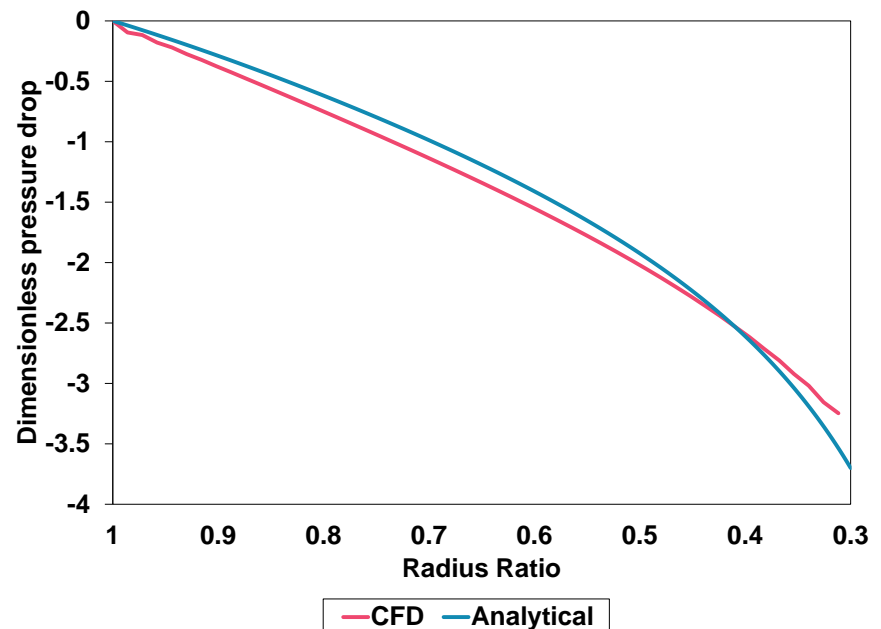


Figure 28 Relative tangential velocity comparison for both the analytical and computational case. Radius ratio of 1 signifies the outer radius of the turbine, relative tangential velocity was made relative to disc speed at a specified radius.

that towards the middle section of the gap, pressure drop becomes fairly linear [50].

Power vs RPM

The uniform flow field simplified the flow variable extraction process. For instance, disc shear stresses to evaluate power was extracted by specifying a radial rake line (from inner to outer radius) within FLUENT. The shear stress plot was integrated along the disc and power estimated using Equation (26, 27). A Power vs RPM plot was used to analyse the disc performance. As shown in Figure 29, the simulated case was capable of higher power output as compared to the analytical for all velocity profiles ($n = 2, 4, 6, 8$). The RPM simulated was set to 2000, resulting in a maximum power output of 216.373 W.

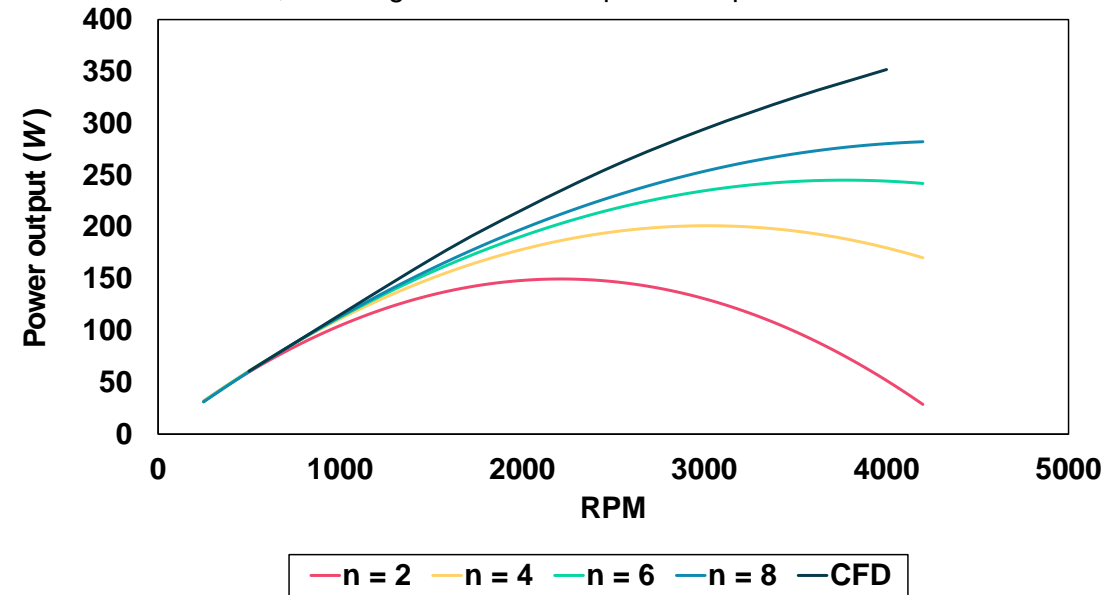


Figure 29 The simulation was repeated for RPM of 500, 1000, 1500, 2000, 2500, 3000, 3500, and 400. The simulated maximum power output was calculated by integrating shear stresses across all discs. The CFD power curve was compared with varying theoretical flow profile power outputs.

5.4.3 Flow characteristics at the inter-disc region

To determine the simulations' degree of accuracy, it was validated against the numerical model for assessing data reliability. Velocity profile plots, pressure contours, pathlines, and shear profiles in the radial direction were extracted from CFD case files and compared with analytical data.

CFD results exhibit a larger decrease in pressure until approximately 0.4 radius ratio, approaching the outlet region. After which the analytical case observes a larger pressure drop. This discrepancy may be caused by numerical models flaws for the turbulent model, with the biggest challenge being flow rotation. Tucker has shown that when flow rotation interacts with turbulence, it may lead to a poor prediction of the eddy viscosities [81]. Results from analytical models by Rusin et al. showing radial pressure distribution and circumferential velocity closely correspond to results reported in this study, arguing that the rotor inlet and outlets are more susceptible to rapid changes in the flow field. Previous studies by Rusin et al. also showed

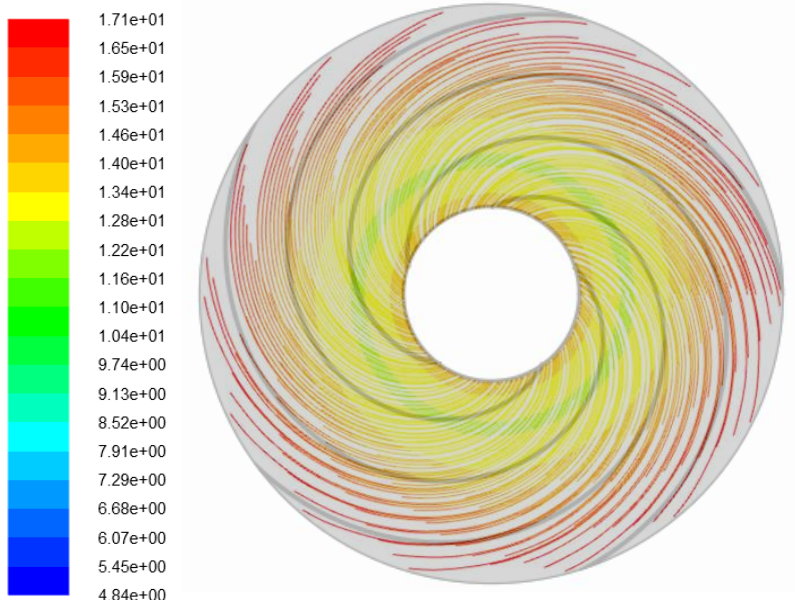


Figure 30 Pathline plot in between the discs. Pathlines extracted from CFD (coloured lines) were superposed with analytical pathlines (coloured black).

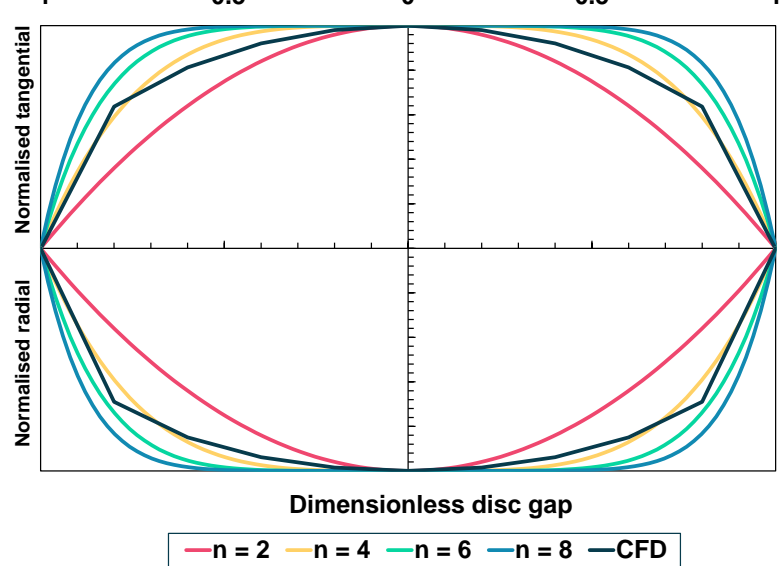


Figure 31 Velocity data was recorded for all 24 inter-disc mesh nodes and averaged. The simulated velocity profile was compared with analytical profiles with exponents of 2, 4, 6, and 8.

This occurrence corresponds to the lower increase in tangential velocity in the radial direction for the CFD case. Similarly, comparing this result with the velocity profile shown in Figure 31, the tangential velocity decrease can be explained by considering characteristics of high shear profile ($n > 8$). Higher shear forces decrease fluid velocity more rapidly, in turn leading to higher power output, agreeing with simulated power output results in Figure 29. Velocities in their respective components were extracted for surface averages at the middle of the gaps.

Figure 33 shows a comparison between radial velocity magnitudes extracted from the inter-disc spacing midpoint. The general trend for both CFD and analytical results closely agree with each other, with maximum deviation of 21% at radius ratio nearing 0.3 (near outlet). For larger radius ratio's, the results are similar, percentage difference between both cases increase nearer the outlet. Average radial velocity validation was integral to ensure mass flow conservation was adhered to. Based on Equation 12, mass flow rate per channel is solely dependent on the radial velocity (assuming a constant flow geometry). This difference may be due to the constantly evolving velocity profile, peak velocities at all points are lower than the analytical as shear forces are higher near wall.

Figure 30 on the left shows shorter simulated pathlines as compared to the analytical case. Fluid particles were observed to accelerate much faster towards the outlet for the simulation. For a more in depth analysis into the flow field, the inter-disc velocity profile was plotted in Figure 31 for both the radial and tangential direction.

The velocity profile computed using CFD closely corresponded to $n = 8$ near the wall, but eventually deviates to one more closely represented by $n = 4$. The simulated profile does not directly match any of the analytical plots in both the tangential and radial direction. It is inferred that due to the continually rotating discs, the flow profile did not fully develop in between. The figure on the right is a bit off.

From Figure 32, the average relative tangential velocity was plotted against radius ratio for both CFD and analytical. Relative tangential velocity for the CFD simulation was observed to be higher than the analytical near the outer radius of the disc. At approximately 0.9 radius ratio, the analytical increases to a value higher than the simulated case. Variation in the tangential velocity agrees with the pathline plot shown in Figure 30 where pathlines for the CFD simulation was initialised at an angle that is close to the analytical case. Shortly after, CFD pathlines start to move faster towards the outlet.

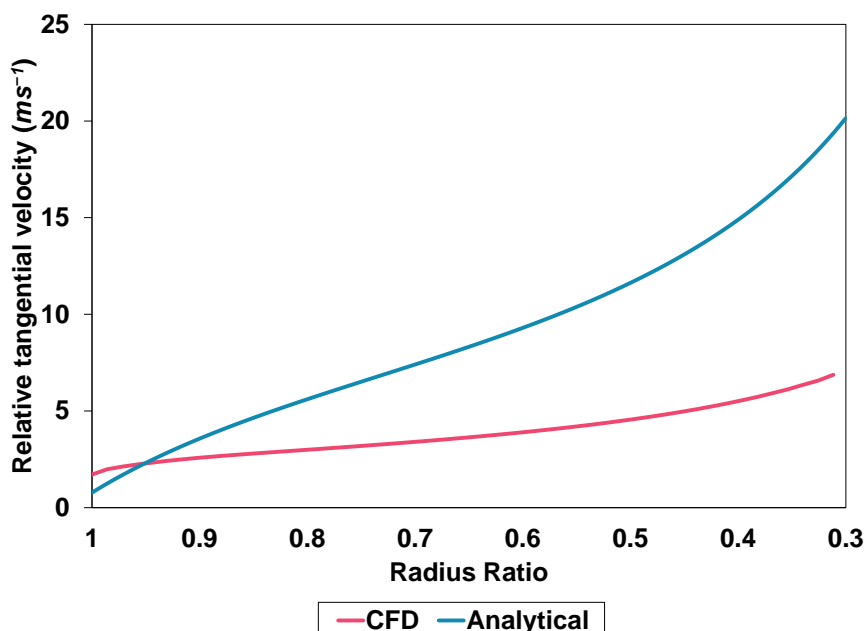


Figure 32 Relative tangential velocity comparison for both the analytical and computational case. Radius ratio of 1 signifies the outer radius of the turbine, relative tangential velocity was made relative to disc speed at a specified radius.

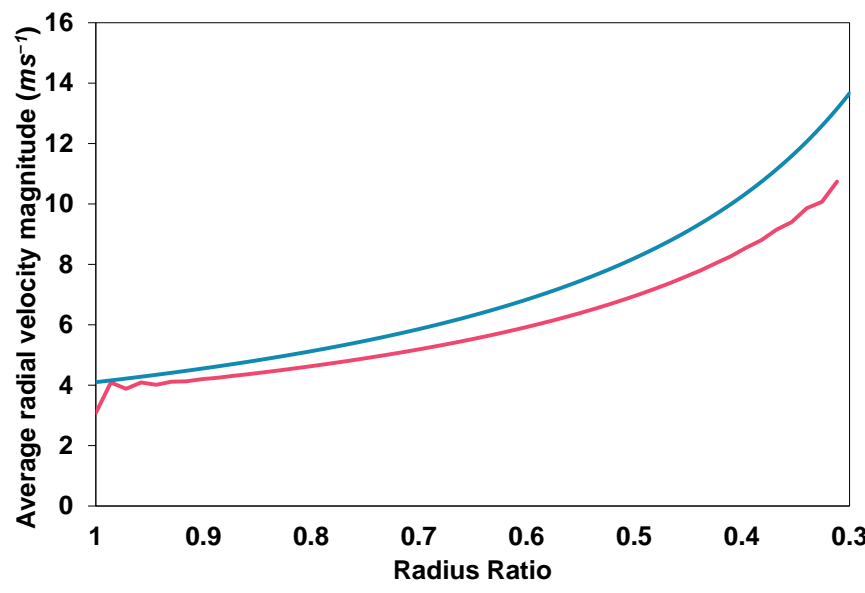


Figure 33 Average radial velocity comparison for both the analytical and computational case. Radius ratio of 1 signifies the outer radius of the turbine.

field (no axial changes). It has been established that a wide range of flow can occur between corotating discs with even turbulent flows proceeding through “reverse transition” to laminar flow [42]. The flow regime for corotating discs can best be characterized by the viscogeometric number, α where the flow is laminar if $\alpha < 1$, transition for $10 < \alpha < 20$ and turbulent for alpha $\alpha > 20$ [82]. The equation for α is shown below (Equation 40) where b is the interdisc spacing, V_r the radial velocity, v the kinematic viscosity, and r the radian position.

$$\alpha = \frac{b^2 V_r}{v r} \quad (40)$$

Following from this, rake lines were used extract the velocity profile along radial segments. Figure 34 shows the radial velocity profile evolution with radius ratio. Upon initial contact with the disc at the outer radius, the change was abrupt, resulting in a jagged velocity profile (radius ratio of 0.993). The simulated profile evolves steadily (without reaching a fully developed state) towards the analytical profile characterized by $n = 2$ as the radial distance decreases. However, at radius ratio of 0.316, the velocity profile shape changes dramatically to resemble that closer to $n = 8$. The initial jagged profile may be attributed by insufficient mesh resolution to represent the rapid changes, resulting in deviations from the analytical case near the inlet. Similarly, the sudden change in profile shape near the outlet suggests more turbulent flow, agreeing with the data discussed below.

Disparity between the CFD and analytical results may also be due to a laminar model being used to characterize the flow for the analytical case. For viscous, axially symmetric flow between two parallel or standing walls, the flow may also experience three-dimensional instabilities that are either laminar-stable, laminar-unstable, or turbulent [82]. The analytical case only takes into account 2D variations in the flow

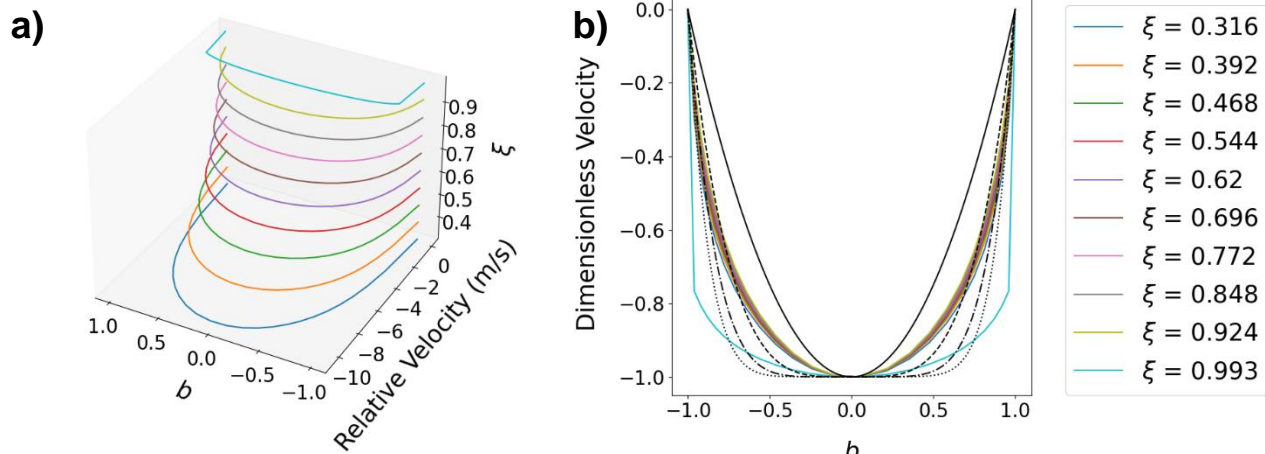
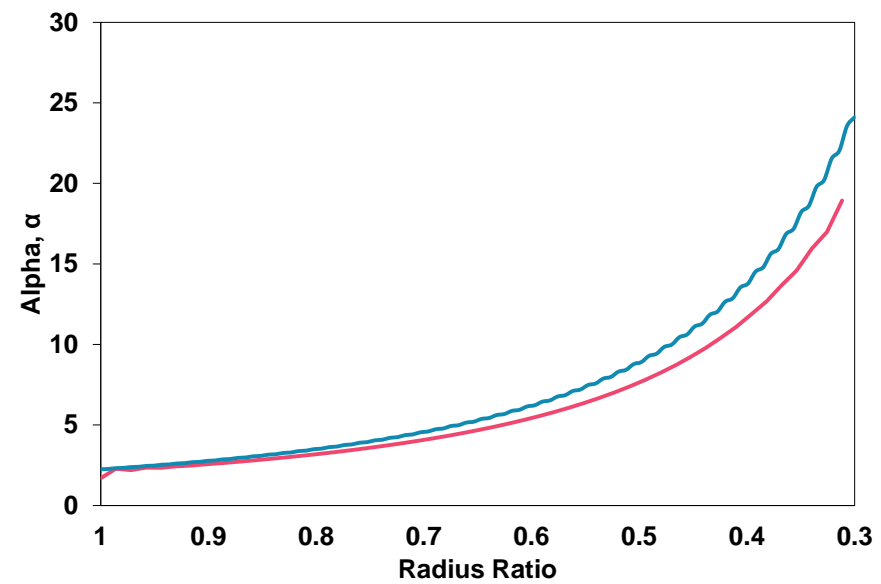


Figure 34 (a) and (b) shows 3D and 2D plots for the radial profiles for different radius ratios.

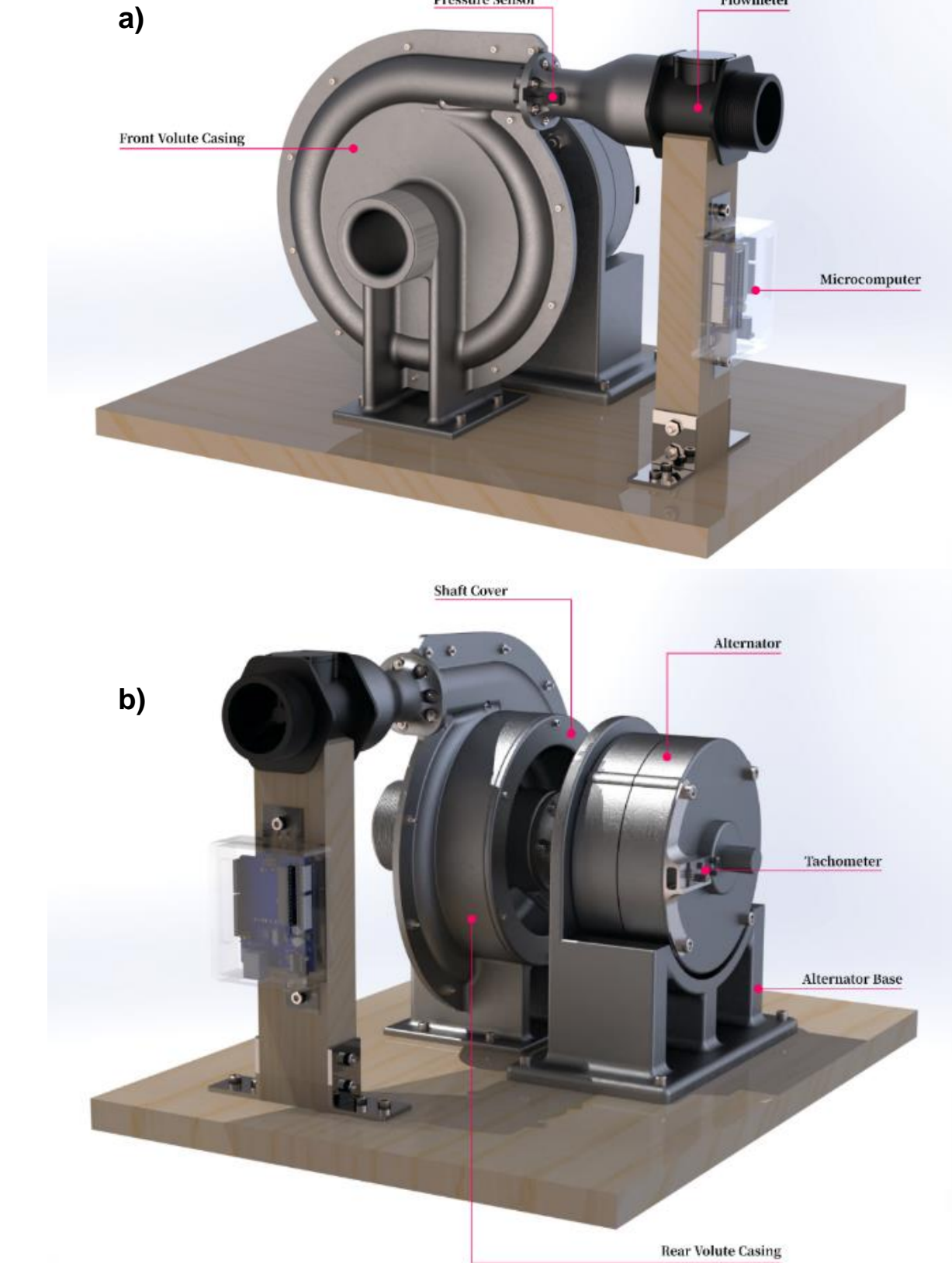
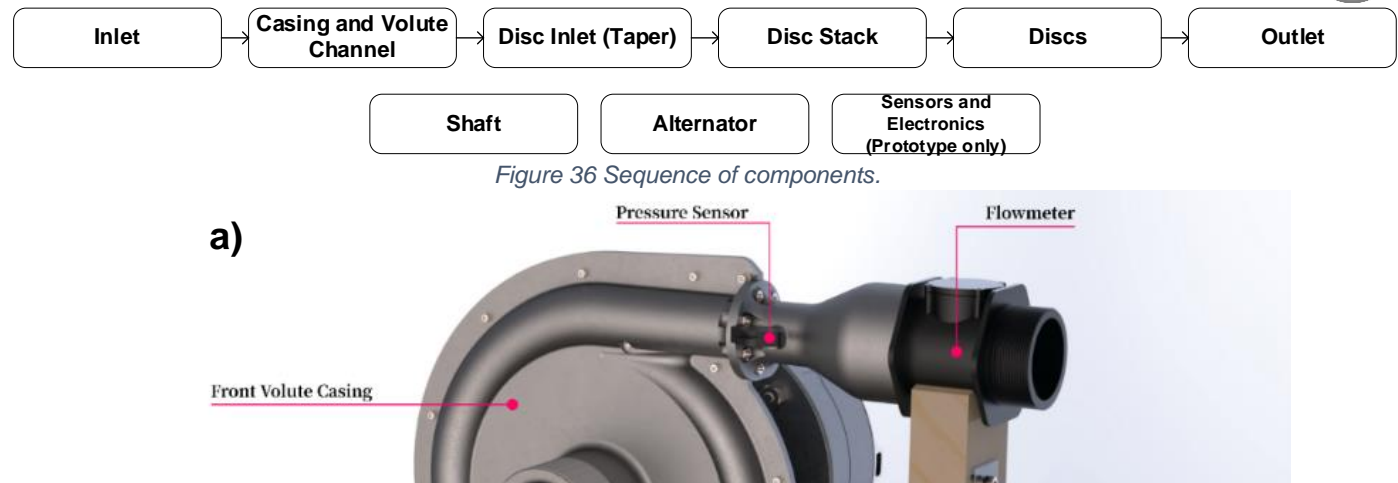
Figure 35 shows α plotted along the radial line, showing that the simulated and analytical flow were laminar near the inlet region from radius ratio of 1 up to approximately 0.45, after which the flow is characterized better as laminar-unstable (transition zone). Due to the lower radial velocities for the CFD case, the laminar to laminar-unstable transition occurred nearer the outlet than the analytical. Despite the increase in α for both cases, only the analytical achieves turbulent flow at radius ratio of 0.32. Analytical studies only considered laminar flow across the entire domain, leading to an inaccurate representation of the actual flow profile nearing the outlet. Similarly, this finding was in line with that fact that initial simulations using the laminar model did not yield convergence, this may be due to the inability to solve for a more complex flow field evolution near the outlet.

This study presents a CFD methodology that works well in validating the analytical results. Key discrepancies between the simulated and analytical data have been discussed, as is suspected to result from a continually evolving flow profile at the interdisc region while the analytical simulation was initialized assuming steady flow profile will be achieved. The analytical results also did not account for turbulence. Future studies should account for these limitations while running a simulation that includes both the casing and disc for an improved representation of the flow conditions in a fully assembled system.

Figure 35 a comparison for both the analytical and computational case. $\alpha < 10$ signify laminar flow while $10 < \alpha < 20$ signify transition flow. Radius ratio of 1 signifies the outer radius of the turbine.

6 Final Design Description and Component Selection

This section describes the finalised design detail and justifications for the component choices to our Tesla Turbine. There are two intended configurations for the Tesla Turbine: an experimental prototype and a commercial design. Differences between these configurations were explained in their respective report sections. A render of the prototype assembly is shown in Figure 37. As shown in the figure, the assembly consists of the Tesla Turbine, alternator and support structures intended for experimentation in the Boldrewood fluids laboratory. The design specifications of respective components are delved into in the later sections. The sequence of which is loosely based on the perspective of a fluid particle and its path as it flows through the turbine. An illustration of the sequence is shown in Figure 36.



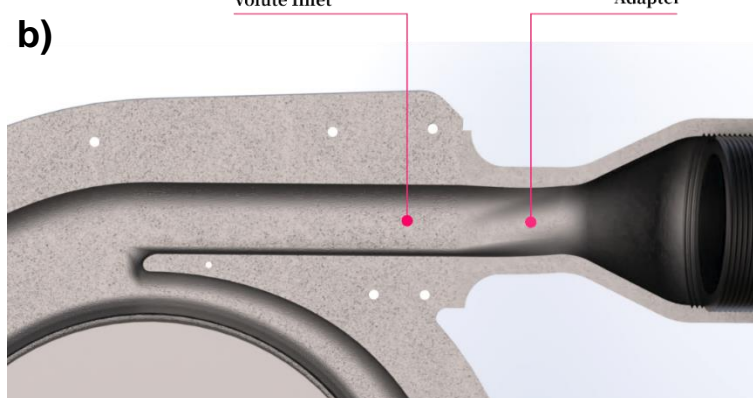
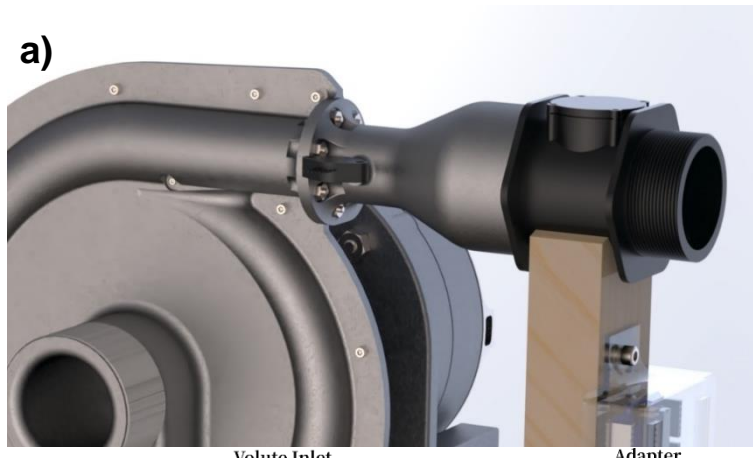


Figure 38 (a) External perspective of the inlet. b) Cross-sectional view of inlet.

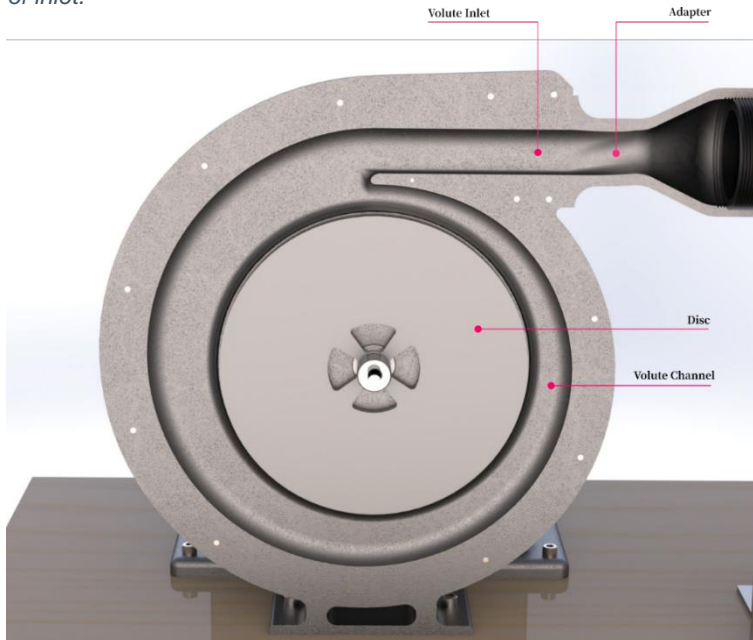


Figure 39 Cross-sectional view of prototype volute casing.

Volute Profile

The channel within the casing is based on circular cross-section with a tangential inlet as shown in Figure 40(c). The variation of cross-sectional area and radius of the centre of the volute passage along the azimuthal angle is based on the profiles plotted in Figure 40(a),(b). Table 9 details the definitions of annotations used for this section.

6.1 Inlet

First, fluid enters the turbine through the inlet located at the top of the casing. The inlet serves as to guide incoming flow into the volute channel located within the casing. A gradual profile was used to create smooth streamlines when guiding incoming flow into the volute channel within the casing. A render of the inlet profile is shown in Figure 38.

Also shown is an additional adapter component only found on the prototype which serves three purposes:

- Reinforcing clamping of the two half volute casings together
- Transitional piece between volute inlet and incoming flow from the upstream flowmeter
- Location used for mounting a pressure sensor to measure inlet head pressure.

6.2 Casing and Volute Channel

Our Tesla Turbine specially features a volute channel as part of the casing geometry which serves to accelerate flow leading up to the disc stack and thus, improving power extraction and the overall performance. The casing also features the biggest difference between prototype and commercial designs. For the prototype, the decision was made to have the casing constitute of two halves, allowing ease of access into the internals of the turbine. As such, an additional rim of material was allocated around the surrounding edges of the casing with holes for nut and bolts fittings. Sealant was applied on contact surfaces to ensure leakage protection. For the commercial implementation, the casing was intended to be a single hollow 3D-shape. A cross-section of the volute casing is shown in Figure 39.

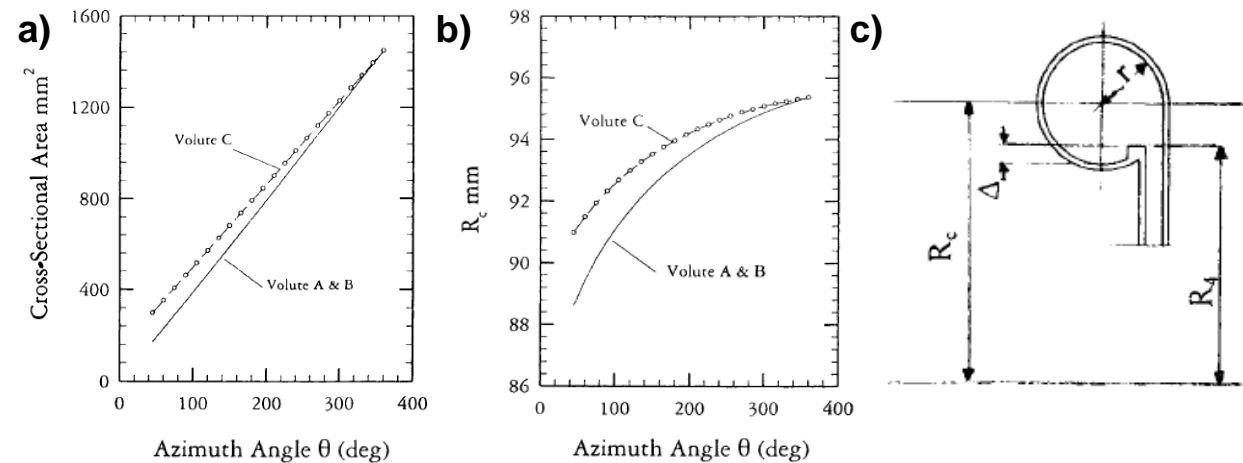


Figure 40 (a) Cross-sectional area variation (b) Variation of R_c (c) Circular cross-section with tangential inlet.

Table 9 Definitions of terms used for volute definition.

Description	Description
α_1 Inlet flow angle between absolute velocity, v_1 and radial velocity, v_r	R Radius from volute centre to any arbitrary position in volute passage
ρ_1 Density of water at taper	C_θ Tangential velocity component
A_1 Taper inlet area	R_4 Radius from volute centre to volute inlet/edge
r_1 Distance from center to taper	$C_{\theta 4}$ Tangential velocity component at volute inlet/edge
ρ_0 Density of water at main inlet	R_c Radius from volute centre to centroid of volute passage
A_0 Main inlet area	r Radius of volute passage sectional circle
r_0 Distance from center to main inlet center	R Radius from volute centre to any arbitrary position in volute passage
w Taper inlet width	C_θ Tangential velocity component
h Main inlet radius	R_4 Radius from volute centre to volute inlet/edge

R , C_θ , R_4 , $C_{\theta 4}$, R_c , and r are inter-related via Equations 41 and 42 [83].

$$RC_\theta = R_4C_{\theta 4} \quad (41)$$

$$R_c - r = R_4 \quad (42)$$

Volute types

There were several volute inlet geometries investigated with reference to the study done by Zheng et al. In their study, three inlet geometries were considered:

- A circular volute with symmetrical inlet which performed the worst as two vortices formed within the volute.
- A circular volute with tangential inlets, which exhibited a more uniform velocity distribution, decent operating range, decent peak efficiency, one vortex.
- A semi-circular volute with tangential inlet, which demonstrated the highest peak efficiency, widest operating range, one vortex.

The second inlet geometry was used in our design as it achieved a uniform velocity distribution which served to deliver equal flow along the entire edge of the discs [84].



Comparison between Plenum and Volute Casings

As detailed in Section 3.1, a plenum chamber design was considered instead of the volute case. Keep *et al.*'s study into comparing plenum and volute casings highlights the superior performance of the plenum chamber designs with 16 times lesser entropy rise and overall pressure loss. However, it does not deliver tangential velocity with the volute casing delivering a more sustained variation along the azimuth angle. Also the desired geometry of the inner ring of the plenum chamber is expensive to manufacture as a high level of precision is required for the nozzles. With further advice from Dr. Davide, we proceeded with the use of the volute instead of the plenum chamber. Keep *et al.*'s study also details the equations to determine the inlet angle and volute size, as shown in Equations 31 – 33.

In conclusion, w , r_0 and h are variables of α_1 . These variables are adjusted to accordingly in Section 4.3 to achieve compact overall size, optimal power generation, sufficiently high inlet flow angle and flow rate [66].

6.3 Disc Inlet (Taper)

Next, the fluid exits the volute channel and is channelled into the disc stack by the taper shown in Figure 41. Unlike a conventional Tesla Turbine, our design incorporates this taper along the volute as to provide a uniform distribution of flow along the entire discs' edge. The taper design ended with a tongue section which is mainly responsible for guiding the remaining fluid from the volute into the disc stack. The initial taper geometry is shown in Figure 41(a), after analysing the CFD results, the taper angle was changed to that in Figure 41(b). The new taper results in a smaller flow angle change when channelling fluid into the inter-disc region. With this variation, frictional losses were reduced and flow angle into the discs were more tangential. In previous nozzle studies, it was shown that a tangential inlet gives the best performance as it provides the highest torque and efficiency [34]. Krishnan *et al.* notes that smaller exhaust area, smaller inlets used in a circular array with multiple nozzles also improve performance [85]. Nevertheless, the specifics of the taper are based on nozzle studies done on the Tesla Turbine. The optimal angle of the taper was found by adjusting it for highest power extraction [24].

Volute Tongue

In search of the optimal geometry and angle for the volute tongue, Alemi *et al.* evaluated the performance of different tongue configurations in a double volute centrifugal pump using CFD. It was found that sharp tongue profiles with low cutwater gap performed the best [86]. We implemented their findings into our own design by minimising the distance between the distance and the tongue while still remaining within manufacturing capability. A cross-sectional view of the volute tongue is shown in Figure 42.

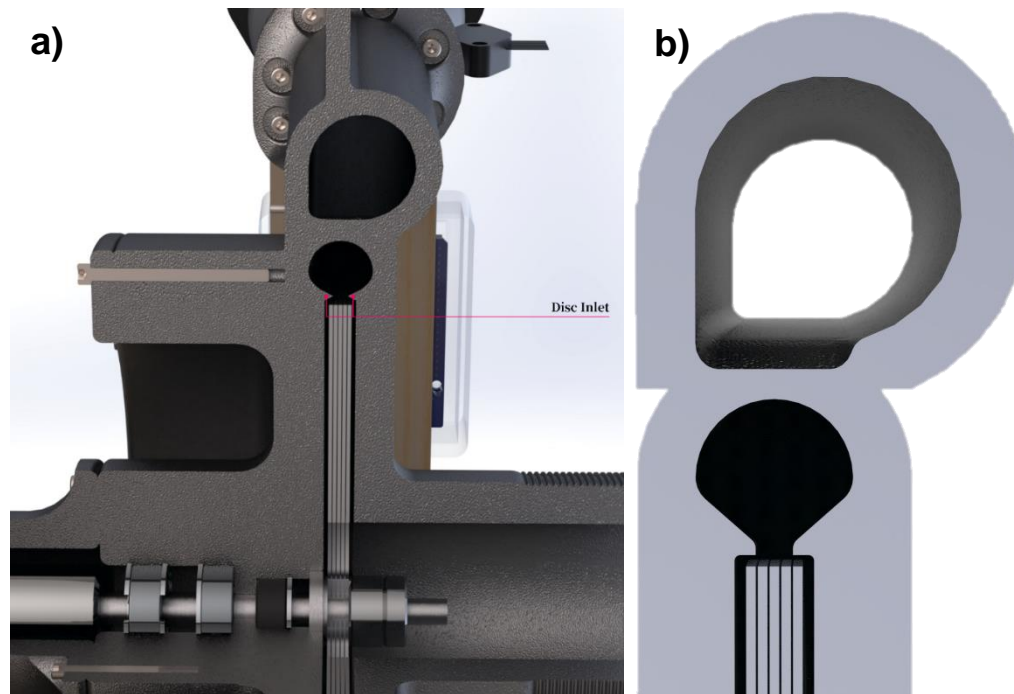


Figure 41 (a) Older taper model shown with the assembly system. (b) New taper model, shown with just the volute casing

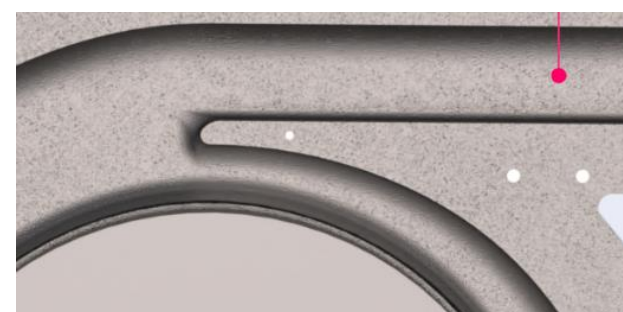


Figure 42 Cross-sectional view of the volute tongue.

6.4 Disc Stack

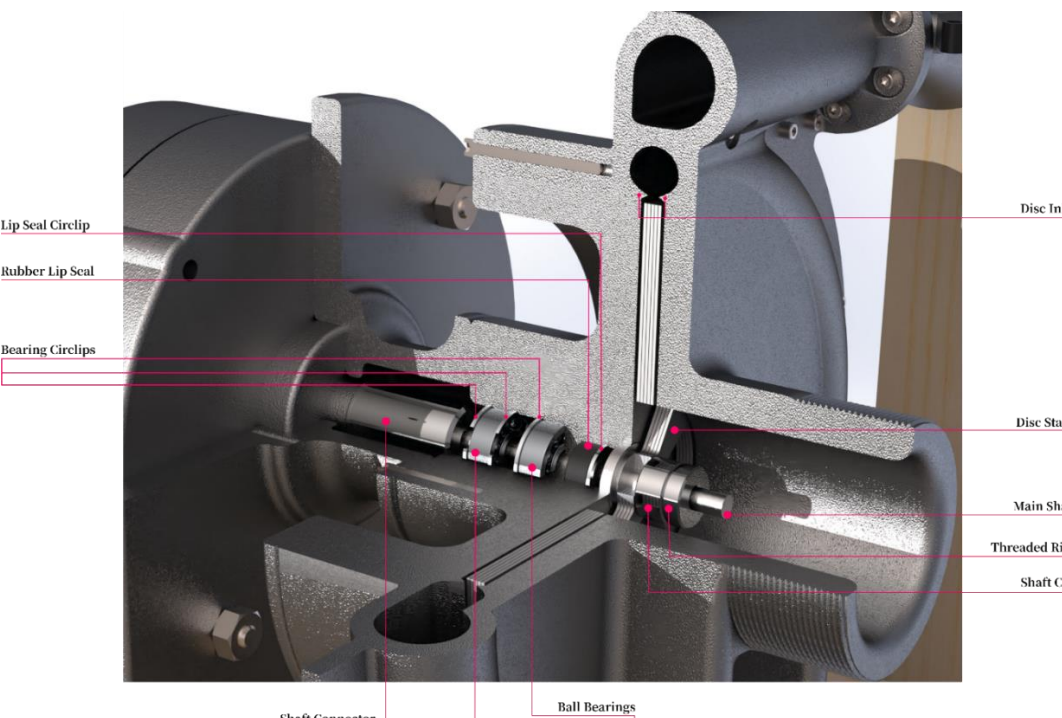


Figure 43 Isometric view of the disc stack assembly.

Figure 43 shows the disc stack as an assembly of five discs stacked atop one another with spacers onto the slot of the shaft. It was secured by an additional threaded ring and shaft cap which aims to distribute clamping pressure evenly onto the roots of the discs. The inter-disc spacing was determined based on available shims at 0.2 mm thick.

Bearing Hub

The casing cover works as a bearing hub that houses two ball bearings that are separated by a safe distance. The distance was determined by the potential generated torque and the maximum radial load of the mentioned bearings. The bearings were fixed into their respective positions using internal grooves and circlips.

All bearings within the bearing hub were set to conventional single-row deep groove bearings. The bearings used were chosen based on their working specification of axial and radial loads and cost-effectiveness. In our turbine, the radial load was determined from the combined weight of the shaft, disc stack, and spacer assembly. Axial loads were assumed to be low due to negligible external forces acting in this direction.

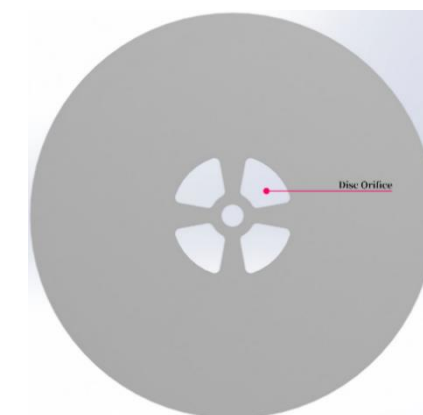


Figure 44 Perpendicular view of the disc.

6.5 Discs

The main disk parameters were determined analytically using numerical methods based on specified inputs as shown in Section 4.

The orifice geometry, shown in Figure 44 was implemented as a compromise between the support and the orifice are for fluid escape. This ensured that the disc maintained its shape under different operating conditions. We arrived at our final design after studying Rusin *et al.*'s investigation on three types of outlet systems. They compared the original outlet from the patent with a spacer-type, which incorporated star-shaped spacers for guiding flow; and a choker-type which consisted of a choking chamber that merged fluid from the disc orifices into the outlet. Their study analysed the designs using CFD and concluded that the spacer type



extracted the most power due to the formation of large swirled regions in the other two designs. Also, the spacers acted as an additional source of torque for the fluid to act upon [43].

6.6 Outlet

Finally, fluid exits the turbine through the outlet located about the centre of the casing. The outlet consists of an extrusion with a threaded outer wall for pipe attachments, shown in Figure 45.

6.7 Shaft

The shaft features slots on both ends to be used with the disc stack and shaft connector respectively. The shaft and shaft connector are shown in Figure 46.

The shaft connector was used to directly link the main shaft of the Tesla Turbine to the shaft of the alternator. It serves as a removable piece as to allow easy turbine detachment without the need for disassembling the alternator shaft. A simplified slotted joint was used instead of the conventional spline shaft as square joints can provide enough grip for torque transmission in addition to its ease of manufacture.



Figure 47 Alternator.

cast aluminum alloy case.

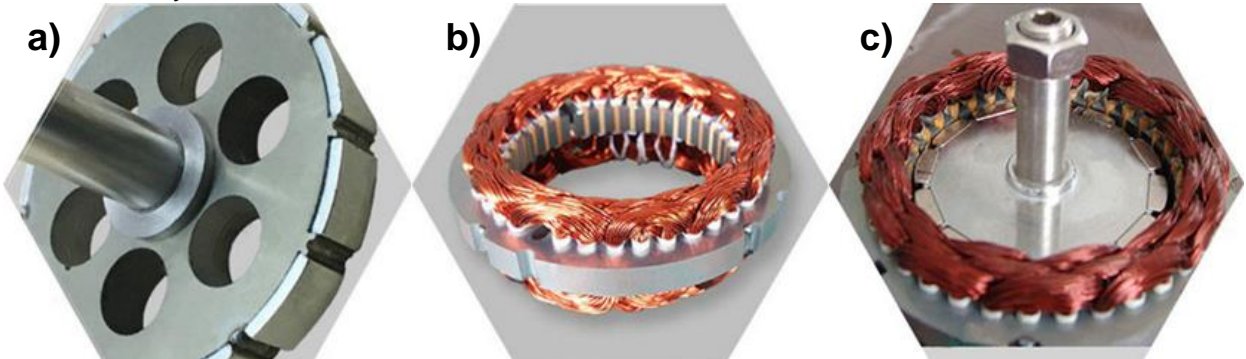


Figure 48 a) NdFeB permanent magnets attached to the rotor. b) Copper windings on the stator. c) Internal assembly of rotor and stator.



Figure 45 Outlet.

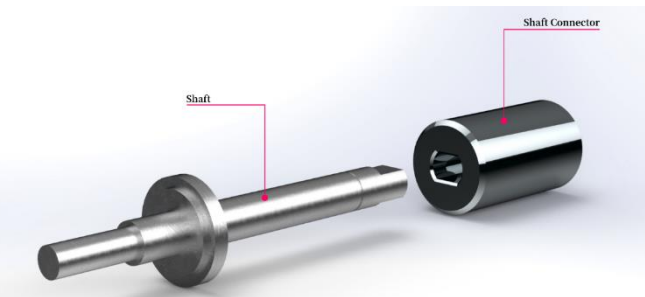


Figure 46 Shaft and shaft connector.

6.8 Alternator

During the early phases of design, considerations were made for modifying a brushless DC motor into an alternator as motors were considerably cheaper and would easily meet our cost specification. However, with limited lab times, we instead opted for off-the-shelf alternators. The models available did not meet our speed ratings, hence this section proposes a modified alternator which suits our use cases.

The alternator design shown in Figure 47 was based off researched commercial products used in small wind turbines and was determined to be a 100 W 12 V permanent earth magnet AC alternator. The three-phase generator will consist of an aluminum-iron-boron permanent magnet (Figure 48(a)) and copper windings stators (Figure 48(b)) encased in a die

It is rated for speeds of 2700 rpm, output frequency of 50 Hz, and operating temperatures of -40°C and 80°C . We chose this alternator design based on common three-phase stator and rotor configurations.

7 Production & Commercialisation

7.1 Prototype Manufacture

We initially had the intention of proceeding with the manufacture of a Tesla Turbine prototype used for experiments. Unfortunately, access to EDMC was limited due to national lockdown. Instead, we shifted focus to a more computational-heavy study for this project, further optimising our turbine design and its performance.

Nevertheless, we believe that our drawings (Appendices) provide enough information for manufacturing the Tesla Turbine prototype. The following plans have been drafted for the prototype manufacture stage using materials and equipment available from the EDMC or Our manufacturing plan consists of three separate stages, characterised by the method of manufacture i.e. subtractive, additive and the final assembly. This separation was planned as categories can be carried out concurrently. Components are assigned to their respective categories based on their respective geometries and materials.

Additive Manufacturing

Table 10 Component list under additive manufacturing.

Part	Equipment	Material	Infill	Estimated Time
Front Casing	FDM	ABS	-	-
Rear Casing	FDM	ABS	-	-
Shaft Cover	FDM	ABS	-	-
Alternator Base	FDM	ABS	-	-
Shaft Cap	FDM	ABS	80%	30 minutes
Tacho Extension	FDM	ABS	10%	1.5 hours
Adapter	FDM	ABS	90%	16 hours

The specific infill densities were allocated with respect to the rigidity and strength required of the component, with high load bearing parts printed with more infill and vice versa. Once the two half volute casings are additively manufactured, secondary manufacturing will take place to incorporate suitable polishing techniques to remove irregularities on the internal surfaces for smoother flow.

Subtractive Manufacturing

Table 11 Component list under subtractive manufacturing.

Part	Drawing No.	Quantity	Equipment	Base Material	Estimated Time
Shaft	GDP45_SH	1	Lathe, CNC Mill	Stainless steel rod (20 mm)	2 hours
Threaded Ring	GDP45_TR	1	Bore, CNC Mill	Stainless steel rod (16 mm)	1 hour
Disc	GDP45_D	5	Waterjet Cutter (MAXIEM 1515)	Stainless steel sheet (0.8 mm)	2 hours
Spacers	GDP45_Spacer	4	Waterjet Cutter (MAXIEM 1515)	Stainless steel shims (0.2 mm)	1 hour
Shaft Connector	GDP45_SCON	1	Bore, CNC Mill	Stainless steel rod (20 mm)	2 hours
Main Platform	GDP45_P	1	Pillar drill, Saw	Plank wood (recycled)	1 hour
Flowmeter Support	GDP45_SU	1	Pillar drill, Saw	Wood block (recycled)	1 hour



7.2 Experimentation

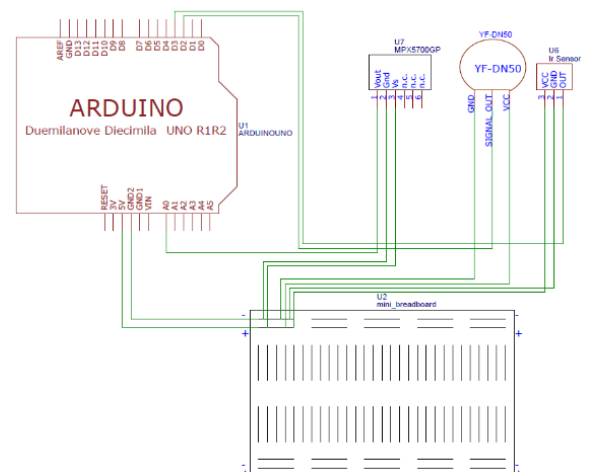


Figure 49 Schematic of electronics setup.

measured and the sensor used for it.

Table 12 Physical quantities measured and the sensors employed.

Physical Quantity	Sensor	Sensor Model ID.
Inlet absolute pressure (Pa)	Absolute Pressure Sensor	MPX4250AP/MPX5700GP
Flow rate (m^3/s)	Flowmeter	YF-DN50
RPM of turbine	Tachometer / Infrared (IR) Sensor	YF-S201
Power extracted from alternator	Resistor circuit + Multimeter	-

An absolute pressure sensor was chosen as it could be assumed that the inlet absolute pressure would be equal to the pressure drop across the turbine. The pressure sensor would be fitted via a pressure tap method at the entrance into the volute casing. The flowmeter chosen would be able to measure the flow rate of water into the turbine and withstand the water pressure through it. This flowmeter has a rotor that rotates at different speeds depending on the speed of water flowing through it. A Hall effect sensor inside the flowmeter would record the changes in the speed of rotor to determine the flow rate. An infrared sensor was to be used in tandem with reflective tape placed on the shaft to act as a make-shift tachometer for measuring RPM. This infrared sensor would be aimed towards a reflective tape that is placed on the turbine shaft to detect the RPM. In addition, a tachometer was also purchased to validate the measurements from the Hall effect sensor. Lastly, a multimeter was obtained to measure the current across a resistor circuit to obtain the power extracted from the alternator. This reading would be manually done without the need of connecting to our Arduino. The power extracted would be using the formula below.

$$P, (\text{Power}) = I^2 (\text{measured Current}) \times R (\text{Resistance of resistor})$$

Before the shift towards computational work, arrangements have been made with lab technicians in securing the test site, a jacuzzi pump capable of producing the required mass flow rates, and test bench.

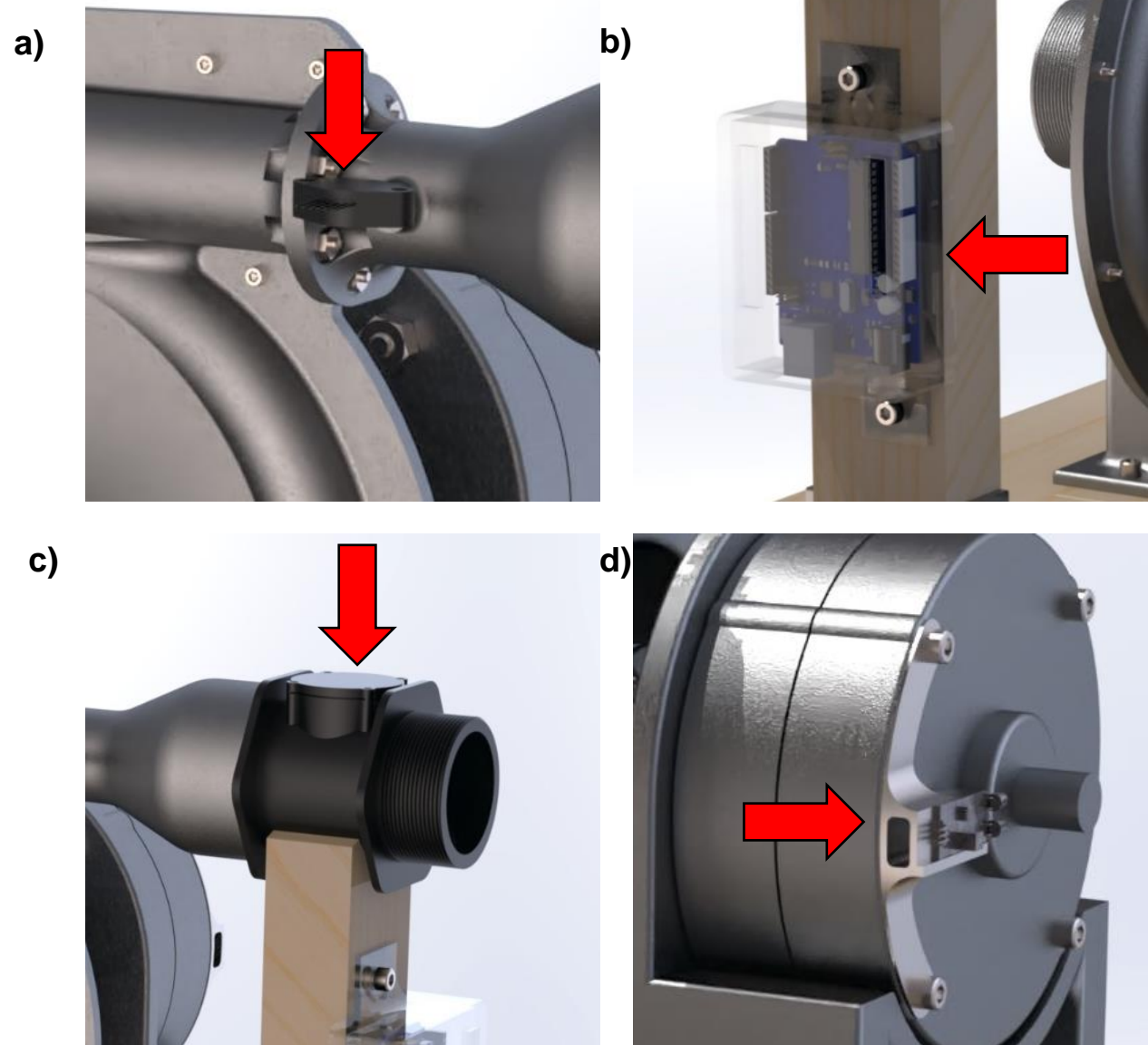


Figure 50 (a) Flowmeter attachment to the adaptor. (b) Arduino Uno. (c) Pressure probe embedded in the inlet. (d) Tachometer on the outside of the alternator.

7.3 Material Selection

This section covers the proposed material choices and justifications for the various components in a commercial Tesla Turbine.

A review was conducted into the materials used for hydropower applications to determine the underlying characteristics and their implications on the performance and lifespan of turbines. Kumar *et al.* investigated the mechanical properties and corrosion behaviour in stainless steels for hydroelectric plant applications and recommends the use of Nitronic 60 due to its desirable pitting resistance, tensile strength, and yield strength. Its attractiveness is further compounded by its weldability which allows for ad hoc repairs and replacements without the need for scrapping large components [87].

However, it was noted that the stresses observed in large hydroelectric applications are far from those at a pico-hydro scale. Hence, other studies prioritising smaller scale turbines were reviewed as well. It was also noted that there are limited studies in materials performance of such hydropower scale, lesser so for the Tesla Turbine. Many testing setups are designed for experimental use only and not suitable for commercial applications. Nevertheless, it can be useful to review previous studies for their choice in materials as a basic guideline. The strongest case found for aluminium was presented by Ishola *et al.*, where stress analysis was



done on pico-scale Pelton wheel buckets [88]. Other studies have also employed the use of brass [89], stainless steel [90] [91], cast iron, cast steel and bronze [92].

The core attributes of materials for our Tesla Turbine are listed below:

- Capable of being shaped into **hollow 3D** structure.
- **Density** specification for major components: casing and shaft cover to remain within weight limit (30 kg). At the current casing and shaft cover volume of 550'000 mm³, this equates to less than 5,500 kg/m³.
- **Weldability** to allow for easy offhand maintenance without the need for complicated processes or complete replacement of parts.
- Durability in **freshwater** and **saltwater**.
- **Galling resistance** against wear.
- **Recyclable** during end of life treatment.

There are two primary groups of metal alloys that fall under the specifications listed above, that is aluminium and magnesium. Aluminium was prioritised as it was less costly overall. Under the limitations specified, the following materials are shortlisted in Table 13.

Table 13 Shortlisted materials for volute casing.

Material	Density, kg m ⁻³	Fatigue Strength at 10 ⁷ cycles, MPa
Aluminium, 383	2740	145.5
Aluminium, EN AC-46000	2760	87.5
Aluminium, EN AC-47100	2650	87.5

It was assumed that the forces within the casing would not exceed the yield strength of the metals, hence all options listed are considered feasible in this regard. Aluminium 383 was determined to be the alloy of choice as it had high fatigue strength while remaining cost effective and well within weight limits.

Disc Stress Analysis

The stress in a rotating disc was evaluated according to the following equation. Using parameters from Section 4.2, the stress evaluates to:

$$\sigma_z = \frac{\omega^2 \rho (r_i^2 + r_i r_o + r_o^2)}{3} = 0.79 \text{ MPa}$$

Therefore, it was concluded that stainless steel is sufficiently strong for enduring the stresses arising from rotation under normal operating conditions.

Shaft Stress Analysis

The shaft stress consists of two main components:

- Bending moment based on cantilevered distance from radial load of the disc stack, shaft cap, and threaded ring, shown in Figure 51 and summarised in Table 14.
- Torque exerted by the disc stack while shaft is stationary.

Masses are estimated based on the reported volumes of components in SolidWorks and their assigned material density.

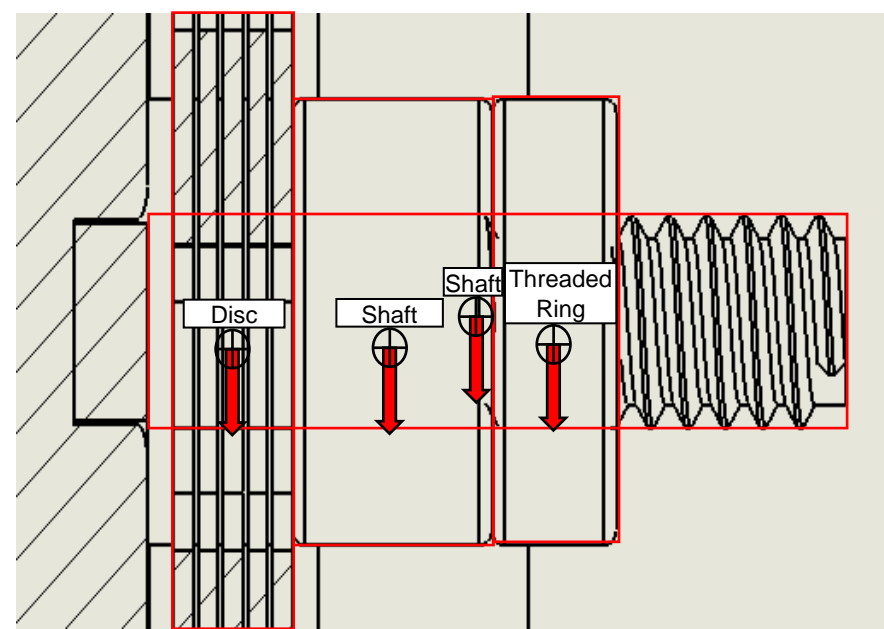


Figure 51 Radial loads acting on the shaft.

Table 14 Calculation of radial load bending moments.

Component	Load, N	Distance, mm	Moment, N m
Disc Stack	0.4g	9.70	0.03839
Shaft Cap	0.01g	12.68	0.00119
Shaft	27 mm * π * 4 mm ² * g * ρ	13.50	0.00519
Threaded Ring	0.01g	16.00	0.00103
		Total	0.04580

The maximum torque is experienced by the shaft in the scenario where the full force of water is acting on the disc stack whilst the shaft is stationary. An initial arbitrary mass flow rate at double the rated baseline was taken as a reference calculation, shown below. It was noted that majority of the shear stress experienced is a result of torsion from the discs rather than internal radial loads.

Bending Moment	Maximum torsional shear stress	Definitions
$\sigma_{bending} = \frac{Mr}{I}$	$\tau_{max} = \frac{Tr}{J}$	g Gravitational acceleration
$\sigma_{bending} = \frac{Mr}{\frac{1}{4}\pi r^4}$	$\tau_{max} = \frac{Tr}{\frac{1}{2}\pi r^4}$	ρ Material density
$\sigma_{bending} = 0.91 \text{ MPa}$	$\tau_{max} = 39.79 \text{ MPa}$	M Moment
		r Shaft radius
		I Polar moment of inertia
		T Torque
		J Area moment of inertia

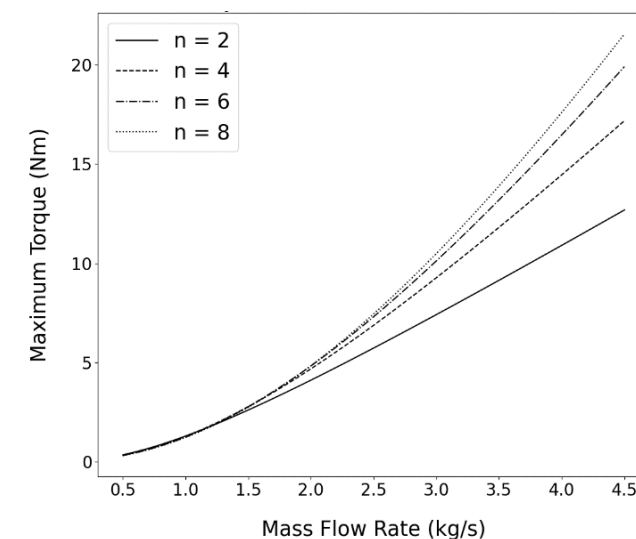


Figure 52 Torque variation along mass flow rate at 0 rpm.

Stainless steel 316 is justified as the shaft material as its yield strength is more than 200 MPa, allowing a safety factor of more than four following this reference calculation. It is also common material used for many applications which makes it easy to attain in most cases, especially in the desired rod form for machining.

With the shaft made of stainless steel 316 and a safety factor of 2, the maximum allowable torque on the discs is 9.96 Nm. Based on Figure 52, it is expected to only occur at a mass flow rates above 3 kg/s⁻¹.

Table 15 Component list of material and manufacturing choices shows a shortened component list for the commercial Tesla Turbine. Auxiliary components used only for prototype testing are omitted. The total mass of turbine and alternator is estimated to be 7.68 kg, making it well within weight specifications and thus easily portable and deployable.

Table 15 Component list of material and manufacturing choices.

Turbine Material			
Component	Material	Manufacturing Method	Estimated Mass, kg
Casing	Aluminium	Casting	2.62
Shaft Cover	Aluminium	Casting	1.42
Shaft Cap	Stainless Steel	Machined from rod	0.01
Shaft	Stainless Steel 316	Machined from rod	0.04
Threaded Ring	Stainless Steel	Machined from rod	0.01
Disc	Stainless Steel	Stamped	0.40
Spacers	Stainless Steel	Stamped	Negligible
Shaft Connector	Stainless Steel	Machined from rod	0.14
		Subtotal	4.65



Externally Sourced		
Bearings		0.03
Lip Circlip	Stainless Steel	Negligible
Lip Seal	-	Negligible
Bearing Circlip	Stainless Steel	Negligible
Shaft Circlip	Stainless Steel	Negligible
Alternator	Aluminium Alloy	3.00
Subtotal		3.03

7.4 Market Analysis & Financial Aspects

This section details the arguments presented for and against the marketability of the Tesla Turbine.

The key factors supporting the marketability of the Tesla Turbine are:

- Climate awareness, accounting for the need to displace energy sources from fossil fuel.
- Increase in rural communities' production and industry capability.

The barriers against the marketability of the Tesla Turbine are:

- Other small-scale renewable sources available commercially, e.g. solar and wind.

Climate Action and Energy Decarbonisation

According to the Intended Nationally Determined Contribution (INDC) submitted by Malaysia to the UNFCCC, Malaysia intends to reduce its greenhouse gas emissions intensity of GDP by 45% by 2030 relative to 2005 levels. In lieu of this, Malaysia has targeted 20% renewable energy in the generation mix by 2025. Policies emerged promoting the use of non-fossil fuel energy with the Ninth Malaysia Plan introducing programmes for adapting biodiesel into the domestic blend of consumer diesel. In the Tenth Malaysia Plan, financial tools were introduced such as the Feed-in Tariff (FiT) mechanism as a fiscal incentive for renewable energy generation [93]. Current progress shows that emissions have gone down by at least 16% in 2014 [94].

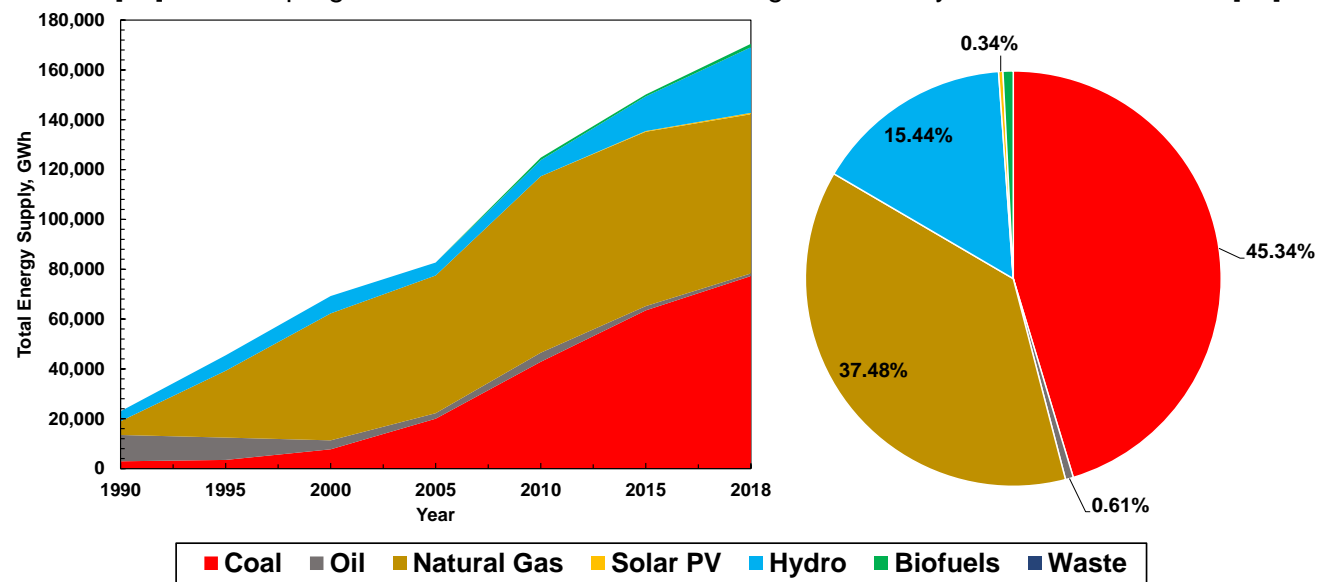


Figure 53 (a) Malaysian Energy Generation by source since 1990 (b) Malaysian Energy Generation by source for 2018 [95].

Figure 53 shows that Malaysia is still heavily reliant on fossil fuels as of 2018, with more than 80% of energy generated from coal, natural gas and oil. As of 2018, Malaysia still remains short of its 2025 goal, thus presents further opportunity for renewables to displace the current fossil fuel dominance in Malaysia, especially with further hydropower developments as the current leading renewable source.

In a survey conducted by Zakaria *et al.*, more than 90% of 83 respondents have heard and knew about renewable energy, indicating public knowledge of renewable energy is high amongst both urban and rural populations [96].

Alam *et al.* also discussed their findings that indicate 79% of 200 respondents demonstrated average to high level of interest in renewable energy. Their study also shows that 9.5% of respondents were opposed or

strongly opposed to hydroelectric generation through dams whilst only 8.5% felt the same way about small hydroelectric on streams. However, a larger percentage (61%) were supportive or strongly supportive towards dam hydroelectricity than small hydroelectric (53.5%) reflecting a more neutral consensus. It is theorised that this is due in part to the lack of information and awareness on renewable energy among the populace, even more so affecting niche sectors such as small hydro [97].

Rural Communities' Productivity

Figure 54 shows a growth in the working age population amongst rural communities which could usher in productivity and industry growth as technological advancement within these communities give rise to more specialised work.

Under the Tenth Malaysia Plan, focus was put on the provision of infrastructure such as water and electricity to rural communities. The Economic Transformation Programme (ETP) launched in 2010 details a comprehensive effort for transforming Malaysia into a high-income nation. Out of the 16 entry point projects identified for the transformation of agriculture sectors, projects such as commercial scale seaweed farming, upgrading premium fruit and vegetable capabilities could benefit from the use of small hydro [4].

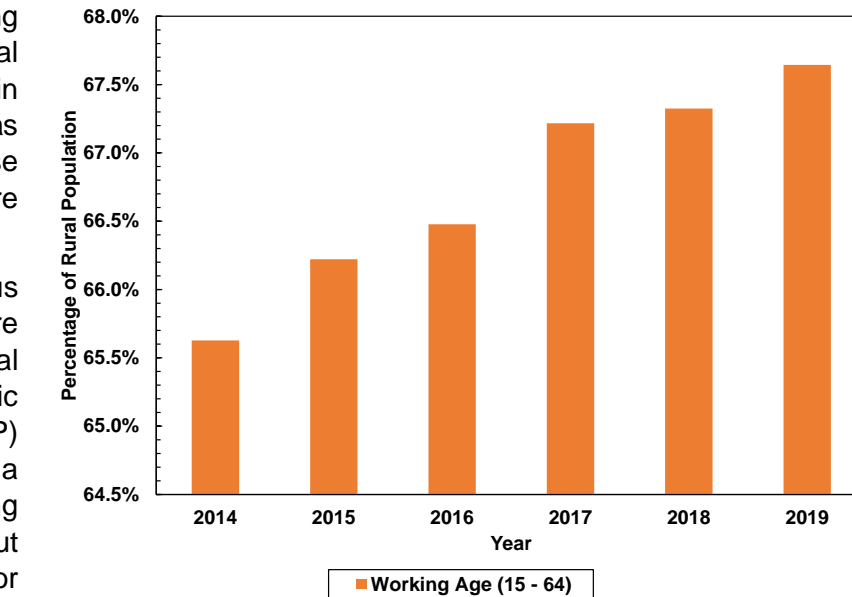


Figure 54 Working age (15 - 64) population percentage of rural communities in Malaysia.

Challenges for other renewables in rural regions

Amongst other forms of renewable generation are solar and wind energy which are widely known amongst the general populace as low-carbon alternatives to fossil fuels. A compilation of commercially available solutions is summarised in Table 16.

Table 16 Comparison of different renewable generation products.

	Tesla Turbine	Solar Panel Kit [100][101]	Wind Turbine Kit [102][103]
Rating, W	100	100	100
Price, £	200	139	110
Rated Speed	-	-	11.2 ms ⁻¹
Accessories	Alternator	Battery, controller	Small tower, alternator

In Malaysia, solar energy is seeing rising interest due to high solar irradiance throughout the country [98]. The local energy commission recognises this advantage and seeks to promote the solar industry by organising Large Scale Solar Farm competitive bidding cycles in an effort to increase the country's photovoltaic generation and lessen reliance on fossil fuels [99].

As shown in Figure 55, Malaysia represents a dense region of tropical forest, characterised by jungle canopies consisting of tall tropical trees.

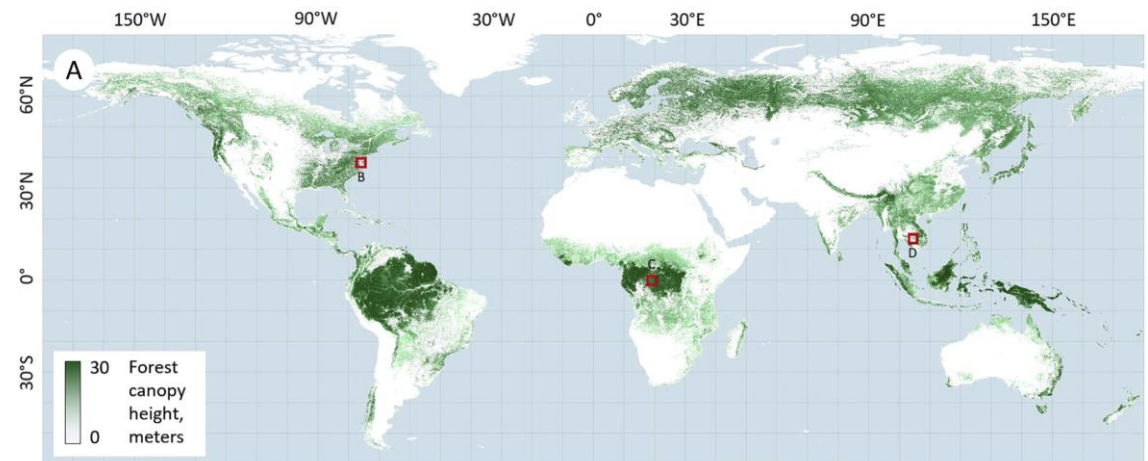


Figure 55 Forest canopy height across the world [104].

In Sabah specifically shown in Figure 56, canopy elevation reaches as high as 40 m with major regions having canopies of greater than 20 m high.

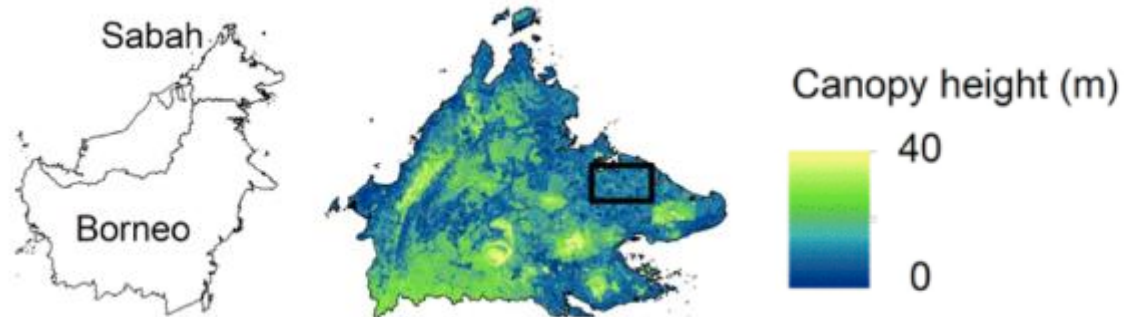
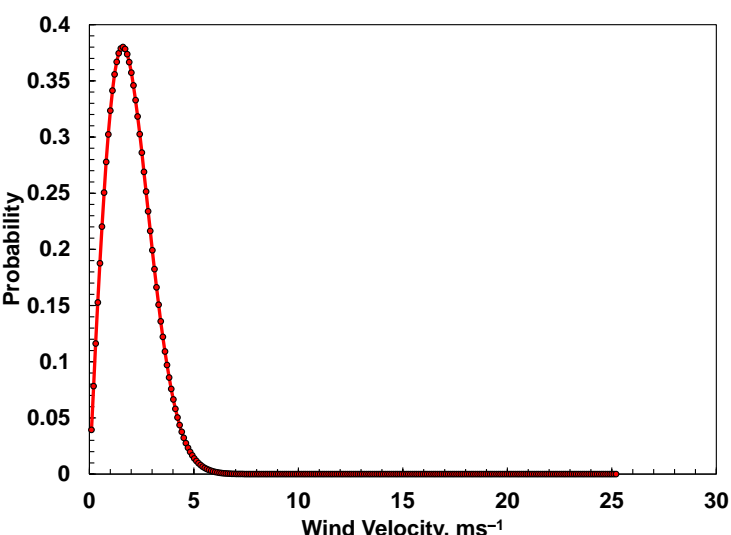


Figure 56 Canopy elevation map in Sabah [105].

This unavailability of clear open spaces poses a challenge for effective solar implementations as providing a challenge for effective solar installations due to the required support infrastructure and clearances needed for overcoming shading issues.

The main challenge against wind turbine implementations in Malaysia are the low average wind speed in tropical regions, which only measure to about 2 ms^{-1} [106]. Figure 57 shows the distribution of wind speeds throughout the year based on a Weibull distribution with a shape factor of 2, aka Rayleigh distribution [107]. The wind turbines listed in Table 16 will rarely reach their rated speeds and it is expected that the energy gained from small wind turbine implementations is minimal and erratic.

Figure 57 Rayleigh distribution of annual wind speeds for the average wind speed of 2 ms^{-1} .

7.5 Environmental Impact and End-of-Life

This section details an environmental impact analysis of the Tesla Turbine with comparisons against other renewables. This preliminary assessment is conducted through evaluating the embodied energy of materials used to provide an estimate of the environmental impact associated with the creation of the product [108].

Admittedly, a comprehensive Life Cycle Analysis (LCA) would be highly speculative for our Tesla Turbine as the product is not in market and has never been tested in the field. This would lead to the use of many assumptions in the turbine performance parameters such as the variation in energy capture return which are

characteristic to individual sites and streams. We believe that such findings would be easily scrutinised hence the adherence to simpler methodologies.

Instead, this preliminary assessment in energy of raw materials could be used as a comparison against other renewables in terms of their cradle environmental impacts.

Assumptions:

- Material primary production energy embodied values (Table A7.1) are the same for all renewable generation products.
- Accessories not included (alternator, battery, support structure).

For the Tesla Turbine, the material values are taken as-is. A general value for PCBs is used for the Arduino Uno. The energy spent on processing is based on the associated energy cost of traditional investment casting of aluminum at 257 MJ per kg [109]. An uncertainty factor of 20% was added on.

A per-meter-squared evaluation was used for the solar panel kit based on prior studies evaluating the life cycle of photovoltaics [110], [111]. Embodied energy for the wind turbine kit is based on that of the Air X 400, which has a similar swept area to the 100 W commercial products shown [112].

Table 17 Total embodied energy of raw materials used in product.

Embody Energy (MJ)			
	Tesla Turbine	Solar Panel Kit	Wind Turbine Kit
Total	2,094	13,150	2,290

As seen in Table 17, the wind turbine kit and Tesla Turbine have similar embodied energy in their products whereas the solar panel kit is estimated to have a much higher value. This is due in course due to the energy intensity of processing monocrystalline silicon cells used in photovoltaics manufacturing [110]. The high energy costs could lead to higher environmental impact due to the embodied energy required to attain the final product. A major limitation in this evaluation is the omission of the impact of implementation, i.e. support structures required for the Tesla Turbine and impact on ecosystem if used on streams, infrastructure for both solar panel and wind turbine.

Operation

The following are the various possible impacts that the turbine may exhibit during operation.

Noise – As a majority of the moving components are submerged during operation, it is expected that noise pollution generated from the turbine to be negligible.

Ecology – As the turbine itself is designed to occupy only a small footprint and does not require a reservoir, displacement of land-based ecology is not expected. In larger rivers where more sizable aquatic life are present, secluded perimeters can be setup for the Tesla Turbine as to prevent these faunas from approaching the turbine and getting trapped. As for smaller streams, aquatic fauna is small enough to pass through the turbine. Also, as the materials of choice are also resistant to pH changes in water, it is expected that minimal leaching occurs and the leached materials non-toxic.

Visual – The small footprint of the turbine allows it to leave minimal impact on its visual surroundings.

Water Quality – The current lubricants used in the bearings are non-toxic, combined with the materials properties as stated in Ecology, water quality is expected to experience negligible impact.

Air Quality – No significant air quality impacts are expected.

End-of-life

As mentioned in

7.3 Material Selection, the material choice for the main components of the Tesla Turbine, i.e. the casing and shaft cover was determined with recyclability as one of its characteristics. A majority of the internal components are constructed of widely recycled materials such as aluminum alloy and stainless steel. Nevertheless, components such as the bearings and alternator are only considered only mostly recyclable



due to the inclusion of various other materials. A summary of the end-of-life treatment for the components of the Tesla Turbine are detailed in Table 18.

Table 18 Individual components of the Tesla Turbine and their supposed end-of-life treatment.

Component	Material	End-of-life Treatment
Casing	Aluminium	Recycled
Shaft Cover	Aluminium	Recycled
Shaft Cap	Stainless Steel	Recycled
Shaft	Stainless Steel 316	Recycled
Threaded Ring	Stainless Steel	Recycled
Disc	Stainless Steel	Recycled
Spacers	Stainless Steel	Recycled
Shaft Connector	Stainless Steel	Recycled
Bearings		Recycled*
Lip Circlip	Stainless Steel	Recycled
Lip Seal	-	Landfill/Combustion
Bearing Circlip	Stainless Steel	Recycled
Shaft Circlip	Stainless Steel	Recycled
Alternator	Aluminium Alloy	Recycled*

According to the Malaysian Ministry of Health, only 6% of the waste composition from rural areas are metal in nature, with less recycling activities occurring in these regions as waste items are more likely to be reused before entering the waste stream. In addition, there is little market for recyclates [113]. One possible initiative is the collection of end-of-life Tesla Turbine components and selling to urban areas where recycling facilities and market for recyclates are more abundant.

8 Further Work

Design

During operation, there is a possibility of damage incurred from rocks and sediment entering the turbine. Bigger obstacles could end up trapped in the volute channel while small and heavy rocks could impact and damage the disc edge. More investigation has to be done into limiting the presence of especially boulders without compromising upstream flow.

Modal Analysis

Further work could be done in carrying out a modal analysis to determine resonant frequencies, ensure no resonance occurs as a result of operation which cause high amplitude of vibrations to occur in critical components such as fastenings.

Material Finishing

Further analysis could be done on the material finishing on various components. Specifically, important as microstructure heavily influences corrosion resistance, more so than hardness [114].

Detailed Costing Model

There was some venture made into attempting to accurately cost the model and determine a final commercial price. Work has done to identify the need to ascertain casting parameters such as clamping pressure, branch sizes, tolerances and roughness. These parameters affect the process specifications and thus both capital expenditure and operational expenditure.

Site Details and Detailed Life Cycle Analysis

With the specification of stream parameters and location, a detailed comparison can be made using site parameters to estimate lifetime generation of various renewable schemes.

Numerical Fitting

As shown in Figure 35, the profile difference between the CFD and that of numerical results at each radial instance can be attributed to entrance effect and flow transitions. These disparities combined led to a near 40% power distinction, which may raise alerts in terms of accuracies. One potential solution to this is to fit in

another profile modifier, e.g. entrance-effect modifier to account for initial flow field at varying Reynolds number. The most immediate solution would be to apply a Fourier analysis on the profile's variations, and to set it as a function dependent on the universal Reynolds number as well as the spatial property. Other methods could also involve simple graph fitting or the use of dimensional analysis.

Furthermore, numerical analysis on pipe flow's turbulence transition could also potentially resolve the above issue up to a significant degree. For this case, an Re -dependent blending function that synthesises both laminar Poiseuille flow and turbulence boundary layer may also be incorporated into the model for much accurate predictions.

Numerical Fitting

As shown in Figure 35, the profile difference between the CFD and that of numerical results at each radial instance can be attributed to entrance effect and flow transitions. These disparities combined led to a near 40% power distinction, which may raise alerts in terms of accuracies. One potential solution to this is to fit in another profile modifier, e.g. entrance-effect modifier to account for initial flow field at varying Reynolds number. The most immediate solution would be to apply a Fourier analysis on the profile's variations, and to set it as a function dependent on the universal Reynolds number as well as the spatial property. Other methods could also involve simple graph fitting or the use of dimensional analysis.

Furthermore, numerical analysis on pipe flow's turbulence transition could also potentially resolve the above issue up to a significant degree. For this case, an Re -dependent blending function that synthesises both laminar Poiseuille flow and turbulence boundary layer may also be incorporated into the model for much accurate predictions.

9 Conclusion

This report details the process and outcomes of Group Design Project 45 in designing and optimising a Tesla Turbine for pico-hydro applications in rural areas. The design aims to address the challenge of rural electrification by providing a means to generate reliable, clean hydropower which can be used to improve the general quality-of-life for rural residents. For this project, an extensive literature review was undertaken as the foundation for the design stages. The literature covered hydroelectricity and the nuances needed for a viable hydropower turbine, the various methodologies used to characterise flow within a Tesla Turbine, and numerous design features and their respective effects on turbine performance.

In pursuit of the goal, the design specification was drafted with consideration for direct and indirect stakeholders and their respective needs and interests taken into account. Other consumer factors were also considered.

In research of past studies, several design features and parameters were considered with findings and results evaluated for integration. This was narrowed down to three main concept designs for which advantages and disadvantages were weighed. A novel volute casing approach was chosen. Then, the core design surrounding rotor parameters were initialised based on inputs such as inlet conditions and rated power using an analytical model developed to characterise the flow between discs.

In this study, we used CFD as a tool for preliminary insight into the performance of turbines and validation against the analytical model. A detailed methodology is presented for the meshing process, ensuring sufficient resolution of the flow variables for validation. We also discussed key discrepancies between the simulated and analytical data, hypothesizing that these arise from a continually evolving flow field at the interdisc region while the analytical simulation was initialized assuming steady flow profile will be achieved. The analytical equation did not account for turbulence while the flow was calculated to be more turbulent near the outlet as the fluid velocity increases. Future studies should account for these limitations while running a simulation that includes both the casing and disc for an improved representation of the flow conditions in a fully assembled system. In conclusion, CFD results show a higher power output (216.4 W at 2000 RPM) than the analytical case due to a larger shearing effect (which agrees with the flow profile shape). The final volute casing performs well in providing a uniform pressure field at the interdisc inlet. However, for



the volute simulation, a slight increase in velocity into the volute outlet was observed upstream of the volute inlet. Further improvements to the volute geometry is paramount to ensure a more uniform velocity field.

Using the results from the analytical and CFD simulations, a final design for the Tesla Turbine was proposed with specifics outlined such as the description of the volute profile and tongue geometry, disc stack assembly employing the use of bearings and seals, arrangement with alternator, and the various auxiliary electronics proposed for use in experiments.

References

- [1] United Nations Statistics Division, "SDG 7: Affordable and Clean Energy," 2019. [Online]. Available: <https://unstats.un.org/sdgs/report/2019/goal-07/>. [Accessed: 27-Mar-2021].
- [2] World Bank Group, "Access to electricity (% of population) - Malaysia," 2019. [Online]. Available: <https://data.worldbank.org/indicator/EG.ELC.ACCS.ZS?locations=MY>.
- [3] Index Mundi, "Malaysia - Access to electricity, rural (% of rural population)," 2019. [Online]. Available: <https://www.indexmundi.com/facts/malaysia/indicator/EG.ELC.AC CS.RU.ZS>. [Accessed: 27-Mar-2021].
- [4] I. Ngah, "Rural Transformations Development : a review on Malaysia 's transformation program," *Int. Conf. Soc. Sci. Humanit. UKM 2012 (ICOSH- UKM 2012) 12-13 December 2012*, no. August, pp. 0–11, 2015.
- [5] J. M. Ngowi, L. Bångens, and E. O. Ahlgren, "Benefits and challenges to productive use of off-grid rural electrification: The case of mini-hydropower in Bulongwa-Tanzania," *Energy Sustain. Dev.*, vol. 53, pp. 97–103, 2019.
- [6] A. Harvey, A. Brown, P. Hettiarachi, and A. Inversin, *Micro-Hydro Design Manual*. Rugby: Practical Action Publishing, 2011.
- [7] B. Giddings and C. Underwood, "Renewable energy in remote communities," *J. Environ. Plan. Manag.*, vol. 50, no. 3, pp. 397–419, 2007.
- [8] A. Kadier, M. S. Kalil, M. Pudukudy, H. A. Hasan, A. Mohamed, and A. A. Hamid, "Pico hydropower (PHP) development in Malaysia: Potential, present status, barriers and future perspectives," *Renew. Sustain. Energy Rev.*, vol. 81, no. August 2016, pp. 2796–2805, 2018.
- [9] M. O. Bello, S. A. Solarin, and Y. Y. Yen, "Hydropower and potential for interfuel substitution: The case of electricity sector in Malaysia," *Energy*, vol. 151, pp. 966–983, 2018.
- [10] I. Hussein and N. Raman, "Reconnaissance studies of micro hydro potential in Malaysia," *Proc. Int. Conf. Energy Sustain. Dev. Issues Strateg. ESD 2010*, 2010.
- [11] M. Hossain *et al.*, "A state-of-the-art review of hydropower in Malaysia as renewable energy: Current status and future prospects," *Energy Strateg. Rev.*, vol. 22, no. November, pp. 426–437, 2018.
- [12] A. A. Lahimer, M. A. Alghoul, K. Sopian, N. Amin, N. Asim, and M. I. Fadhel, "Research and development aspects of pico-hydro power," *Renew. Sustain. Energy Rev.*, vol. 16, no. 8, pp. 5861–5878, 2012.
- [13] A. M. A. Haidar, M. F. M. Senan, A. Noman, and T. Radman, "Utilization of pico hydro generation in domestic and commercial loads," *Renew. Sustain. Energy Rev.*, vol. 16, no. 1, pp. 518–524, 2012.
- [14] S. J. Williamson, B. H. Stark, and J. D. Booker, "Low head pico hydro turbine selection using a multi-criteria analysis," *Renew. Energy*, vol. 61, pp. 43–50, 2014.
- [15] N. Tesla, "U.S. Patent No. 1,061,206," 1,061,206, 1913.
- [16] B. P. Ho-Yan, "Tesla Turbine for Pico Hydro Applications," *Guelph Eng. J.*, no. 4, p. 2, 2011.
- [17] V. G. Krishnan, V. Romanin, V. P. Carey, and M. M. Maharbiz, "Design and scaling of microscale Tesla Turbines," *J. Micromechanics Microengineering*, vol. 23, no. 12, 2013.
- [18] K. K. Srinivasan, P. J. Mago, and S. R. Krishnan, "Analysis of exhaust waste heat recovery from a dual fuel low temperature combustion engine using an Organic Rankine Cycle," *Energy*, vol. 35, no. 6, pp. 2387–2399, 2010.
- [19] N. Shokati, F. Ranjbar, and M. Yari, "Exergoeconomic analysis and optimization of basic, dual-pressure and dual-fluid ORCs and Kalina geothermal power plants: A comparative study," *Renew. Energy*, vol. 83, pp. 527–542, Nov. 2015.
- [20] H. Chen, D. Y. Goswami, and E. K. Stefanakos, "A review of thermodynamic cycles and working fluids for the conversion of low-grade heat," *Renew. Sustain. Energy Rev.*, vol. 14, no. 9, pp. 3059–3067, Dec. 2010.
- [21] J. Song, C. wei Gu, and X. song Li, "Performance estimation of Tesla Turbine applied in small scale Organic Rankine Cycle (ORC) system," *Appl. Therm. Eng.*, vol. 110, pp. 318–326, 2017.
- [22] L. Ciappi, D. Fiaschi, P. H. Niknam, and L. Talluri, "Computational investigation of the flow inside a Tesla Turbine rotor," *Energy*, vol. 173, pp. 207–217, 2019.
- [23] L. Pacini, L. Ciappi, L. Talluri, D. Fiaschi, G. Manfrida, and J. Smolka, "Computational investigation of partial admission effects on the flow field of a Tesla Turbine for ORC applications," *Energy*, vol. 212, p. 118687, Dec. 2020.
- [24] V. D. Romanin, "Theory and Performance of Tesla Turbines," p. 98, 2012.
- [25] V. Shah and S. Dhokai, "Tesla Turbine Experiment," *Int. J. Sci. Res.*, vol. 6, no. 7, pp. 113–116, 2017.
- [26] K. Holland, "Design , construction and testing of a Tesla Turbine by Kris Holland A thesis submitted in partial fulfillment Of the
- [27] G. P. Hoya and A. Guha, "The design of a test rig and study of the performance and efficiency of a Tesla disc turbine," *Proc. Inst. Mech. Eng. Part A J. Power Energy*, vol. 223, no. 4, pp. 451–465, 2009.
- [28] R. Li, H. Wang, E. Yao, M. Li, and W. Nan, "Experimental study on bladeless turbine using incompressible working medium," *Adv. Mech. Eng.*, vol. 9, no. 1, 2017.
- [29] W. Qi, Q. Deng, Z. Feng, and Q. Yuan, "Influence of disc spacing distance on the aerodynamic performance and flow field of Tesla Turbines," *Proc. ASME Turbo Expo*, vol. 8, 2016.
- [30] B. H. . P and M. N. D, "an Effect of Surface Finish and Spacing Between Discs on the Performance of Disc Turbine," *Int. J. Appl. Res. Mech. Eng.*, pp. 250–255, 2012.
- [31] E. William Beans, "Investigation into the performance characteristics of a friction turbine," *J. Spacecr. Rockets*, vol. 3, no. 1, pp. 131–134, 1966.
- [32] W. Qi, Q. Deng, Y. Jiang, Q. Yuan, and Z. Feng, "Disc thickness and spacing distance impacts on flow characteristics of multichannel Tesla Turbines," *Energies*, vol. 12, no. 1, 2019.
- [33] M. U. S. Khan, E. Ali, M. I. Maqsood, and H. Nawaz, "Modern improved and effective design of boundary layer turbine for robust control and efficient production of green energy," *J. Phys. Conf. Ser.*, vol. 439, no. 1, 2013.
- [34] J. F. Andres and M. E. Loretero, "Performance of Tesla Turbine using open flow water source," *Int. J. Eng. Res. Technol.*, vol. 12, no. 12, pp. 2191–2199, 2019.
- [35] A. Guha and B. Smiley, "Experiment and analysis for an improved design of the inlet and nozzle in Tesla disc turbines," *Proc. Inst. Mech. Eng. Part A J. Power Energy*, vol. 224, no. 2, pp. 261–277, 2010.
- [36] C. Soares, "Accessory Systems," in *Gas Turbines*, 2015, pp. 413–484.
- [37] V. Chandavari and S. Palekar, "Diffuser Angle Control To Avoid Flow Separation," *Tech. Res. Appl.*, vol. 2, no. 5, pp. 16–21, 2014.
- [38] E. M. Sparrow, J. P. Abraham, and W. J. Minkowycz, "Flow separation in a diverging conical duct: Effect of Reynolds number and divergence angle," *Int. J. Heat Mass Transf.*, vol. 52, no. 13–14, pp. 3079–3083, 2009.
- [39] R. M. C. So, "Inlet centerline turbulence effects on reattachment length in axisymmetric sudden-expansion flows," *Exp. Fluids*, vol.



- 5, no. 6, pp. 424–426, 1987.
- [40] X. Wang, Y. Zhu, W. Li, X. Zhang, and H. Chen, "Flow characteristics of an axial turbine with chamber and diffuser adopted in compressed air energy storage system," *Energy Reports*, vol. 6, pp. 45–57, Dec. 2020.
- [41] L. Talluri, O. Dumont, G. Manfrida, V. Lemort, and D. Fiaschi, "Geometry definition and performance assessment of Tesla Turbines for ORC," *Energy*, vol. 211, p. 118570, 2020.
- [42] W. Rice, "Tesla Turbomachinery," 1991.
- [43] K. Rusin, "The Influence of Outlet System Geometry on Tesla Turbine Working Parameters," *Acta Innovations*, no. 22, pp. 58–67, 2017.
- [44] W. Qi, Q. Deng, Y. Jiang, Z. Feng, and Q. Yuan, "Aerodynamic performance and flow characteristics analysis of Tesla Turbines with different nozzle and outlet geometries," *Proc. Inst. Mech. Eng. Part A J. Power Energy*, vol. 233, no. 3, pp. 358–378, 2019.
- [45] S. H. Hasinger and L. G. Kehrt, "Investigation of a Shear-Force Pump," *J. Eng. Power*, vol. 85, no. 3, pp. 201–206, Jul. 1963.
- [46] T. W. Choon, A. A. Rahman., F. S. Jer, and L. E. Aik, "Optimization of Tesla Turbine using Computational Fluid Dynamics approach," in *2011 IEEE Symposium on Industrial Electronics and Applications*, 2011, pp. 477–480.
- [47] V. D. Romanin, V. G. Krishnan, V. P. Carey, and M. M. Maharbiz, "Experimental and Analytical Study of Sub-Watt Scale Tesla Turbine Performance," in *Volume 7: Fluids and Heat Transfer, Parts A, B, C, and D*, 2012, pp. 1005–1014.
- [48] Y. Galindo, J. A. Reyes-Nava, Y. Hernández, G. Ibáñez, J. Moreira-Acosta, and A. Beltrán, "Effect of disc spacing and pressure flow on a modifiable Tesla Turbine: Experimental and numerical analysis," *Appl. Therm. Eng.*, vol. 192, 2021.
- [49] S. Sengupta and A. Guha, "Inflow-rotor interaction in Tesla disc turbines: Effects of discrete inflows, finite disc thickness, and radial clearance on the fluid dynamics and performance of the turbine," *Proc. Inst. Mech. Eng. Part A J. Power Energy*, vol. 232, no. 8, pp. 971–991, 2018.
- [50] K. Rusin, W. Wróblewski, and M. Strozik, "Comparison of methods for the determination of Tesla Turbine performance," *J. Theor. Appl. Mech.*, vol. 57, no. 3, pp. 563–575, 2019.
- [51] M. Zuber, A. Ramesh, and D. Bansal, "The Tesla Turbine - A comprehensive review," *J. Adv. Res. Fluid Mech. Therm. Sci.*, vol. 62, no. 1, pp. 122–137, 2019.
- [52] P. Lampart and Ł. Jedrzejewski, "Investigations of Aerodynamics of Tesla bladeless microturbines," *J. Theor. Appl. Mech.*, vol. 49, no. 2, pp. 477–499, 2011.
- [53] P. Lampart, K. Kosowski, M. Piwowarski, and L. Jedrzejewski, "Design analysis of Tesla micro-turbine operating on a low-boiling medium," *Polish Marit. Res.*, vol. 16, no. Special, pp. 28–33, 2009.
- [54] J. Peirs, D. Reynaerts, and F. Verplaetse, "A microturbine for electric power generation," *Sensors Actuators, A Phys.*, vol. 113, no. 1, pp. 86–93, 2004.
- [55] E. Lemma, R. T. Deam, D. Toncich, and R. Collins, "Characterisation of a small viscous flow turbine," *Exp. Therm. Fluid Sci.*, vol. 33, no. 1, pp. 96–105, 2008.
- [56] R. T. Deam, E. Lemma, B. Mace, and R. Collins, "On scaling down turbines to millimeter size," *J. Eng. Gas Turbines Power*, vol. 130, no. 5, 2008.
- [57] V. G. Krishnan, "Design and Fabrication of cm-scale Tesla Turbines," vol. 49, no. 23–6, pp. 22–23, 2015.
- [58] K. E. Boyd and W. Rice, "Laminar inward flow of an incompressible fluid between rotating disks, with full peripheral admission," *J. Appl. Mech. Trans. ASME*, vol. 35, no. 2, pp. 229–237, 1964.
- [59] A. Guha and S. Sengupta, "Similitude and scaling laws for the rotating flow between concentric discs," *Proc. Inst. Mech. Eng. Part A J. Power Energy*, vol. 228, no. 4, pp. 429–439, 2014.
- [60] A. Guha and S. Sengupta, "The physics of pressure variation in microchannels within corotating or static discs," *Phys. Fluids*, vol. 28, no. 10, 2016.
- [61] A. Guha and S. Sengupta, "The fluid dynamics of work transfer in the non-uniform viscous rotating flow within a Tesla disc turbomachine," *Phys. Fluids*, vol. 26, no. 3, 2014.
- [62] D. Zhao, C. Ji, C. Teo, and S. Li, "Performance of small-scale bladeless electromagnetic energy harvesters driven by water or air," *Energy*, vol. 74, no. C, pp. 99–108, 2014.
- [63] W. Rice, "An Analytical and Experimental Investigation of Multiple-Disk Turbines," *J. Eng. Power*, pp. 1–8, 1965.
- [64] S. Sengupta and A. Guha, "A theory of Tesla disc turbines," *Proc. Inst. Mech. Eng. Part A J. Power Energy*, vol. 226, no. 5, pp. 650–663, 2012.
- [65] V. D. Romanin and V. P. Carey, "An integral perturbation model of flow and momentum transport in rotating microchannels with smooth or microstructured wall surfaces," *Phys. Fluids*, vol. 23, no. 8, 2011.
- [66] J. A. Keep and I. J. Jahn, "Design method and performance comparison of plenum and volute delivery systems for radial inflow turbines," *Proc. 20th Australas. Fluid Mech. Conf. AFMC 2016*, no. December, 2016.
- [67] S. Yang, F. Kong, and B. Chen, "Research on Pump Volute Design Method Using CFD," *Int. J. Rotating Mach.*, vol. 2011, pp. 1–7, 2011.
- [68] H. Alemi, S. Ahmad Nourbakhsh, M. Raisee, and A. Farhad Najafi, "Development of new 'multivolute casing' geometries for radial force reduction in centrifugal pumps," *Eng. Appl. Comput. Fluid Mech.*, vol. 9, no. 1, pp. 1–11, Jan. 2015.
- [69] W. de OJEDA and R. D. FLACK, "Pressure Distributions in a Single and Two Versions of a double volute of a centrifugal pump," *Am. Soc. Mech. Eng.*, vol. 20, p. 8, 1992.
- [70] K. Diaelhag, "Simulation of an axial turbine runner's blade using CFD," *1st Annu. Int. Interdiscip. Conf.*, p. 7, 2013.
- [71] J. M. Variava, A. S. Bhavsar, and T. B. Patel, "Performance Analysis of Tesla Turbo Machine As Turbine Using Cfd," *Int. J. Adv. Res. Innov. Ideas Educ.*, vol. 3, no. 1, pp. 1429–1439, 2017.
- [72] R. J. Pandey, S. Pudasaini, S. Dhakal, and R. B. Uprety, "Design and Computational Analysis of 1 kW Tesla," *Int. J. Sci. Res. Publ.*, vol. 4, no. 11, pp. 1–5, 2014.
- [73] K. N. . Joshi, M. N. . Sanghvi, and T. D. . Dave, "Hybrid Tesla Pelton wheel turbine," *Int. J. Sci. Eng. Res.*, vol. 7, no. 9, p. 6, 2016.
- [74] M. A. Meghnine, M. K. Hamidou, and M. Hamel, "Influence of the volute cross-sectional shape on mixed inflow turbine performances," *Adv. Mech. Eng.*, vol. 9, no. 7, p. 168781401770817, Jul. 2017.
- [75] M. Yang, R. Martinez-Botas, S. Rajoo, T. Yokoyama, and S. Ibaraki, "An investigation of volute cross-sectional shape on turbocharger turbine under pulsating conditions in internal combustion engine," *Energy Convers. Manag.*, vol. 105, pp. 167–177, Nov. 2015.
- [76] D. Frączek, W. Wróblewski, and K. Bochon, "Influence of honeycomb rubbing on the labyrinth seal performance," *J. Eng. Gas Turbines Power*, vol. 139, no. 1, 2017.
- [77] W. Wróblewski, D. Frączek, and K. Marugi, "Leakage reduction by optimisation of the straight-through labyrinth seal with a honeycomb and alternative land configurations," *Int. J. Heat Mass Transf.*, vol. 126, pp. 725–739, Nov. 2018.
- [78] E. C. Miller, M. R. L'Ecuyer, and E. F. Benisek, "Flow field surveys at the rotor inlet of a radial inflow turbine," *J. Eng. Gas Turbines Power*, vol. 110, no. 3, pp. 552–561, 1988.
- [79] B. Neumann, *The interaction between geometry and performance of a centrifugal pump*. Mechanical Engineering Publications Limited, 1991.
- [80] A. T. Simpson, S. W. T. Spence, and J. K. Watterson, "A Comparison of the Flow Structures and Losses Within Vaned and Vaneless Stators for Radial Turbines," *J. Turbomach.*, vol. 131, no. 3, Jul. 2009.
- [81] P. G. Tucker, "Trends in turbomachinery turbulence treatments," *Prog. Aerosp. Sci.*, vol. 63, pp. 1–32, Nov. 2013.
- [82] D. Nendl, "Dreidimensionale laminare Instabilitäten bei ebenen Wänden," *ZAMM - J. Appl. Math. Mech. / Zeitschrift für Angew. Math. und Mech.*, vol. 56, no. S1, pp. 72–74, 1976.
- [83] D. Pan, A. Whitfield, and M. Wilson, "Design considerations for the volutes of centrifugal fans and compressors," *Proc. Inst. Mech. Eng. Part C J. Mech. Eng.*, vol. 213, no. 4, pp. 401–410, 1999.
- [84] X. Zheng, Y. Lin, and Z. Sun, "Effects of volute's asymmetry on the performance of a turbocharger centrifugal compressor," *Proc. Inst. Mech. Eng. Part G J. Aerosp. Eng.*, vol. 232, no. 7, pp. 1235–1246, 2018.
- [85] V. G. Krishnan, Z. Iqbal, and M. M. Maharbiz, "A micro Tesla Turbine for power generation from low pressure heads and evaporation driven flows," *2011 16th Int. Solid-State Sensors, Actuators Microsystems Conf. TRANSDUCERS'11*, no. June 2011,



Group 45 – Tesla Turbine Design

- pp. 1851–1854, 2011.
- [86] H. Alemi, S. A. Nourbakhsh, M. Raisee, and A. F. Najafi, "Effect of the volute tongue profile on the performance of a low specific speed centrifugal pump," *Proc. Inst. Mech. Eng. Part A J. Power Energy*, vol. 229, no. 2, pp. 210–220, 2015.
- [87] A. Kumar and A. A. Odeh, "Mechanical Properties and Corrosion Behavior of Stainless Steels for Locks, Dams, and Hydroelectric Plant Applications," 1989.
- [88] F. A. Ishola, J. Azeta, G. Agbi, O. O. Olatunji, and F. Oyawale, "Simulation for material selection for a pico pelton turbine's wheel and buckets," *Procedia Manuf.*, vol. 35, pp. 1172–1177, 2019.
- [89] I. Safdar, S. Sultan, H. A. Raza, M. Umer, and M. Ali, "Empirical analysis of turbine and generator efficiency of a pico hydro system," *Sustain. Energy Technol. Assessments*, vol. 37, no. August 2019, p. 100605, 2020.
- [90] H. Hoghooghi, M. Durali, and A. Kashef, "A new low-cost swirler for axial micro hydro turbines of low head potential," *Renew. Energy*, vol. 128, pp. 375–390, 2018.
- [91] A. Morabito, G. de Oliveira e Silva, and P. Hendrick, "Deriaz pump-turbine for pumped hydro energy storage and micro applications," *J. Energy Storage*, vol. 24, no. April, p. 100788, 2019.
- [92] S. Tilahun, V. Paramasivam, M. Tufa, A. kerebih, and S. K. Selvaraj, "Analytical investigation of Pelton turbine for mini hydro power: For the case of selected site in Ethiopia," *Mater. Today Proc.*, no. xxxx, pp. 1–5, 2021.
- [93] UNFCCC, "Intended Nationally Determined Contribution of the Government of Malaysia," *United Nations Framew. Conv. Clim. Chang.*, p. 6, 2015.
- [94] Government of Malaysia, *Malaysia Third National Communication and Second Biennial Update Report To the United Nations Framework Convention on Climate Change (NC3)*. 2018.
- [95] International Energy Agency, "Total energy supply by source, Malaysia 1990 - 2018," 2019. [Online]. Available: <https://www.iea.org/data-and-statistics?country=MALAYSIA&fuel=Energy supply&indicator=TPESbySource>. [Accessed: 22-Apr-2021].
- [96] S. U. Zakaria, S. Basri, S. K. Kamarudin, and N. A. A. Majid, "Public Awareness Analysis on Renewable Energy in Malaysia," *IOP Conf. Ser. Earth Environ. Sci.*, vol. 268, no. 1, 2019.
- [97] S. S. Alam, N. F. M. Nor, M. Ahmad, and N. H. N. Hashim, "A survey on renewable energy development in Malaysia: Current status, problems and prospects," *Environ. Clim. Technol.*, vol. 17, no. 1, pp. 5–17, 2016.
- [98] S. T. Mohammad, H. H. Al-Kayiem, M. A. Aurybi, and A. K. Khlief, "Measurement of global and direct normal solar energy radiation in Seri Iskandar and comparison with other cities of Malaysia," *Case Stud. Therm. Eng.*, vol. 18, no. January, p. 100591, 2020.
- [99] Malaysian Energy Comission, "Large Scale Solar Photovoltaic Bidding Cycle 1," 2020. [Online]. Available: <https://www.st.gov.my/en/web/industry/details/2/12>. [Accessed: 04-May-2021].
- [100] TP-solar Store, "TP-Solar Solar Panel Kit 100 Watt 12 Volt Monocrystalline Off Grid System." [Online]. Available: https://www.amazon.co.uk/Monocrystalline-Controller-Mounting-Brackets-Connector/dp/B07S2B2QGV/ref=sr_1_6?dchild=1&keywords=100+Watt+Solar+Panel+Kit&qid=1619195124&quartzVehicle=95-1833&replacementKeywords=watt+solar+panel+kit&sr=8-6. [Accessed: 23-Apr-2021].
- [101] Sun Solar, "SunSolar SW100M-32." [Online]. Available: <https://shopee.com.my/READY-STOCK-Solar-Panel-100W-100Watt-MONO-12V-MONOCrystalline-Cells-Solar-Panel-Module-TUV-Certified-Factory-Direct-i.13785177.2424140190>. [Accessed: 24-Apr-2021].
- [102] Lowenergie, "Lowenergie Wind Turbine 100W 12V Generator Kit," 2020.
- [103] Dioo, "Dioo Portable Compact Size Wind Turbine Generator 100W." [Online]. Available: <https://shopee.com.my/Dioo-Portable-Compact-Size-Wind-Turbine-Generator-100W-Small-Turbines-Simple-Installation-for-Homes-Power-Generation-Rate-Industrial-i.284693592.9023801359>.
- [104] P. Potapov *et al.*, "Mapping global forest canopy height through integration of GEDI and Landsat data," *Remote Sens. Environ.*, vol. 253, no. October 2020, p. 112165, 2021.
- [105] T. Okuda *et al.*, "Canopy height recovery after selective logging in a lowland tropical rain forest," *For. Ecol. Manage.*, vol. 442, no. January, pp. 117–123, 2019.
- [106] S. A. Salih, S. Mat, K. Sopian, E. Saleh, and M. Alkhair, "Simulation analysis of Venturi-Vertical Axis Wind Turbine (V-VAWT)," no. April, pp. 191–196, 2014.
- [107] T. Burton, N. Jenkins, D. Sharpe, and E. Bossanyi, *Wind Energy Handbook, Second Edition*. 2011.
- [108] K. Benton, "Digital Commons @ Montana Tech A LIFE CYCLE ASSESSMENT OF A DIESEL," *Mont. Tech Thesis*, 2016.
- [109] B. Zeng, M. Jolly, and K. Salonitis, "Investigating the energy consumption of casting process by multiple life cycle method," *Proceeding 1st Int. Conf. Sustain. Des. Manuf.*, no. April, pp. 28–30, 2014.
- [110] I. Nawaz and G. N. Tiwari, "Embodied energy analysis of photovoltaic (PV) system based on macro- and micro-level," *Energy Policy*, vol. 34, no. 17, pp. 3144–3152, 2006.
- [111] A. Anctil, C. W. Babbitt, R. P. Raffaelle, and B. J. Landi, "Cumulative energy demand for small molecule and polymer photovoltaics," *Prog. Photovoltaics Res. Appl.*, vol. 21, no. 7, pp. 1541–1554, 2013.
- [112] K. A. Glassbrook, A. H. Carr, M. L. Drosnes, T. R. Oakley, R. M. Kamens, and S. H. Gheewala, "Life cycle assessment and feasibility study of small wind power in Thailand," *Energy Sustain. Dev.*, vol. 22, no. 1, pp. 66–73, 2014.
- [113] E. S. Division, "Ministry of Health Guidelines on Solid Waste Management," 1999.
- [114] S. Weng, Y. H. Huang, F. Z. Xuan, and L. H. Luo, "Correlation between Microstructure, Hardness and Corrosion of Welded Joints of Disc Rotors," *Procedia Eng.*, vol. 130, pp. 1761–1769, 2015.
- [115] G. Manfrida, L. Pacini, and L. Talluri, "A revised Tesla Turbine Concept for ORC applications," *Energy Procedia*, vol. 129, pp. 1055–1062, 2017.



Appendices

A.4 Analytical

Simplified version:

Integral simplifications for phi:

$$\int_{-\frac{b}{2}}^{\frac{b}{2}} \phi(z) dz = 2 \int_0^{\frac{b}{2}} \phi(z) dz = b$$

$$\int_{-\frac{b}{2}}^{\frac{b}{2}} \phi(z)^2 dz = 2 \int_0^{\frac{b}{2}} \phi(z)^2 dz = \frac{2(n+1)}{2n+1} b$$

$$\int_{-\frac{b}{2}}^{\frac{b}{2}} \frac{d^2 \phi(z)}{dz^2} dz = 2 \int_0^{\frac{b}{2}} \frac{d^2 \phi(z)}{dz^2} dz = -\frac{4(n+1)}{b}$$

Mass Flow Rate:

$$\int_{-\frac{b}{2}}^{\frac{b}{2}} r v_r dz = \int_{-\frac{b}{2}}^{\frac{b}{2}} r \bar{v}_r(r) \phi(z) dz = r \bar{v}_r(r) b = b C_r$$

mass conservation requires that $-2\pi r_0 \rho \int_{-b/2}^{b/2} v_r dz = \dot{m}_c$, where \dot{m}_c is the mass flow rate per channel:

$$-2\pi r_0 \rho \int_{-b/2}^{b/2} v_r dz = -2\pi r_0 \rho \bar{v}_r(r_0) \int_{-b/2}^{b/2} \phi(z) dz = -2\pi r_0 \rho \bar{v}_r(r_0) b = \dot{m}_c$$

Note: $\bar{v}_r(r_0) = \bar{v}_{r0}$

$$\bar{v}_{r0} = \frac{\dot{m}_c}{2\pi r_0 b \rho}$$

$$\bar{v}_r = -\frac{r_0}{r} \bar{v}_{r0}$$

Relationship between n, Fpo and Po

$$f = \frac{2\mu \left[\frac{\partial(v_\theta(r, z) - U)}{\partial z} \right]_{z=\frac{b}{2}}}{\rho \bar{v}_\theta^2}$$

$$= \frac{2\mu \bar{v}_\theta \left[\frac{\partial \phi(z)}{\partial z} \right]_{z=\frac{b}{2}}}{\rho \bar{v}_\theta^2}$$

$$= \frac{2\mu}{\rho \bar{v}_\theta} \left[-\frac{n+1}{n} \left(\frac{2}{b} \right) \left(n \left(\frac{2z}{b} \right)^{n-1} \right) \right]_{z=\frac{b}{2}}$$

$$= \frac{2\mu}{\rho \bar{v}_\theta} \left[-\frac{2(n+1)}{b} \right]$$

$$\frac{Po}{Re_c} = \frac{2\mu}{\rho \bar{v}_\theta} \left[\frac{2(n+1)}{b} \right]$$

$$\frac{\mu Po}{\rho \bar{v}_\theta D_H} = \frac{2\mu}{\rho \bar{v}_\theta} \left[\frac{2(n+1)}{b} \right]$$

$$Po = D_H \left[\frac{4(n+1)}{b} \right]$$

$$Po = 8(n+1)$$

$$Po/8 = (n+1) = 3F_{Po}$$

Wall Shear Stress

$$\tau_w = f \frac{\rho \bar{v}_\theta^2}{2}$$

$$\tau_w = \frac{2\mu}{\rho \bar{v}_\theta} \left[-\frac{2(n+1)}{b} \right] \frac{\rho \bar{v}_\theta^2}{2}$$

$$\tau_w = -\frac{2\mu(n+1)\bar{v}_\theta}{b}$$

Wall Friction Term

$$f_\theta = \frac{F_\theta}{\rho V_e} = \frac{4\tau_w}{\rho D_H} = -\frac{4}{\rho D_H} \frac{2\mu(n+1)\bar{v}_\theta}{b} = -\frac{16\mu(n+1)\bar{v}_\theta}{\rho D_H^2}$$

Note:

From the above definitions:

$$v_r = -\frac{v\phi(z)Re_m^*}{D_H \xi \epsilon} = -\frac{r_0}{r} \phi(z) \bar{v}_{r0} = -\frac{r_0}{r} \phi(z) V_{r0} U_0$$

$$\frac{\partial}{\partial r} = \frac{\partial}{\partial \xi} \frac{\partial \xi}{\partial r} = \frac{1}{r_0} \frac{\partial}{\partial \xi}$$

Tangential ODE

$$v_r \frac{\partial v_\theta}{\partial r} + \frac{v_\theta v_r}{r} = -\frac{16\mu(n+1)\bar{v}_\theta}{\rho D_H^2}$$

$$\frac{\partial v_\theta}{\partial r} + \frac{v_\theta}{r} = -\frac{1}{v_r} \frac{16\mu(n+1)\bar{v}_\theta}{\rho D_H^2}$$

$$\frac{\partial v_\theta}{\partial r} + \frac{v_\theta}{r} = \frac{D_H \xi \epsilon}{v\phi(z) Re_m^*} \frac{16\mu(n+1)\bar{v}_\theta}{\rho D_H^2}$$

$$\frac{\partial v_\theta}{\partial r} + \frac{v_\theta}{r} = \frac{\xi \epsilon}{\phi(z) Re_m^*} \frac{16(n+1)\bar{v}_\theta}{D_H}$$

$$\phi(z) \left[\frac{\partial \bar{v}_\theta}{\partial r} + \frac{\bar{v}_\theta}{r} \right] + \frac{2U_0}{r_0} = \frac{\xi \epsilon}{\phi(z) Re_m^*} \frac{16(n+1)\bar{v}_\theta}{D_H}$$

$$\phi(z)^2 \left[\frac{\partial \bar{v}_\theta}{\partial r} + \frac{\bar{v}_\theta}{r} \right] + \phi(z) \frac{2U_0}{r_0} = \frac{\xi \epsilon}{Re_m^*} \frac{16(n+1)\bar{v}_\theta}{D_H}$$

Integrating both side across the channel ($\frac{1}{b} \int_{-b/2}^{b/2} dz$):

$$\frac{2(n+1)}{2n+1} \left[\frac{\partial \bar{v}_\theta}{\partial r} + \frac{\bar{v}_\theta}{r} \right] + \frac{2U_0}{r_0} = \frac{\xi \epsilon}{Re_m^*} \frac{16(n+1)\bar{v}_\theta}{D_H}$$

$$\frac{2(n+1)}{2n+1} U_0 \left[\frac{\partial \hat{W}}{\partial r} + \frac{\hat{W}}{r} \right] + \frac{2U_0}{r_0} = \frac{U_0 \epsilon}{Re_m^*} \frac{16\xi(n+1)\hat{W}}{D_H}$$

$$\frac{2(n+1)}{2n+1} \left(\frac{U_0}{r_0} \right) \left[\frac{\partial \hat{W}}{\partial \xi} + \frac{\hat{W}}{\xi} \right] + 2 \left(\frac{U_0}{r_0} \right) = \left(\frac{U_0}{r_0} \right) \frac{16\xi(n+1)\hat{W}}{Re_m^*}$$

Divide both side by $\left(\frac{U_0}{r_0} \right)$:

$$\frac{2(n+1)}{2n+1} \left[\frac{\partial \hat{W}}{\partial \xi} + \frac{\hat{W}}{\xi} \right] = \frac{16\xi(n+1)\hat{W}}{Re_m^*} - 2$$

$$\left[\frac{\partial \hat{W}}{\partial \xi} + \frac{\hat{W}}{\xi} \right] = \frac{2n+1}{n+1} \left(\frac{8\xi(n+1)\hat{W}}{Re_m^*} \right) - \frac{2n+1}{n+1}$$

$$\left[\frac{\partial \hat{W}}{\partial \xi} + \frac{\hat{W}}{\xi} \right] = \frac{8(2n+1)\xi\hat{W}}{Re_m^*} - \frac{2n+1}{n+1}$$

$$-\frac{2n+1}{n+1} = \left[\frac{1}{\xi} - \frac{8(2n+1)\xi}{Re_m^*} \right] \hat{W} + \frac{\partial \hat{W}}{\partial \xi}$$

Radial ODE

$$v_r \frac{\partial v_r}{\partial r} - \frac{v_\theta^2}{r} = -\frac{1}{\rho} \left(\frac{\partial P}{\partial r} \right) + v \left\{ \frac{\partial^2 v_r}{\partial z^2} + \frac{1}{r} \frac{\partial}{\partial r} \left(r \frac{\partial v_r}{\partial r} \right) - \frac{v_r}{r^2} \right\}$$

$$\frac{(r_0 \phi(z) V_{r0} U_0)^2}{r} \frac{\partial}{\partial r} \left(\frac{1}{r} \right) - \left[\frac{(\bar{v}_\theta(r) \phi(z) + U(r))^2}{r} \right]$$

$$= -\frac{1}{\rho} \left(\frac{\partial P}{\partial r} \right) + v \left[\frac{\partial^2}{\partial z^2} \left(-\frac{r_0}{r} \phi(z) V_{r0} U_0 \right) \right]$$

$$- (r_0 \phi(z) V_{r0} U_0) \left(\frac{1}{r} \frac{\partial}{\partial r} \left(r \frac{\partial}{\partial r} \left(\frac{1}{r} \right) \right) - \frac{1}{r^3} \right)$$

$$- \frac{(r_0 \phi(z) V_{r0} U_0)^2}{r^3} - \left[\frac{(\hat{W} U_0 \phi(z) + U(r))^2}{r} \right]$$

$$= -\frac{1}{\rho} \left(\frac{\partial P}{\partial r} \right) + v \left[- \left(\frac{r_0 V_{r0} U_0}{r} \right) \frac{\partial^2 \phi(z)}{\partial z^2} \right]$$

$$- (r_0 \phi(z) V_{r0} U_0) \left(\frac{1}{r} \frac{\partial}{\partial r} \left(-\frac{1}{r} \right) - \frac{1}{r^3} \right)$$

$$- \frac{(r_0 \phi(z) V_{r0} U_0)^2}{r^3} - \left[\frac{(\hat{W} U_0 \phi(z))^2 + 2\hat{W} U_0 U(r) \phi(z) + U(r)^2}{r} \right]$$

$$= -\frac{1}{\rho} \left(\frac{\partial P}{\partial r} \right) + v \left[- \left(\frac{r_0 V_{r0} U_0}{r} \right) \frac{\partial^2 \phi(z)}{\partial z^2} + 0 \right]$$

Integrating both side across the channel ($\frac{1}{b} \int_{-b/2}^{b/2} dz$):

$$-\frac{2(n+1)(r_0 V_{r0} U_0)^2}{2n+1} \frac{1}{r^3} - \left[\frac{2(n+1)(\hat{W} U_0)^2}{2n+1} \frac{1}{r} + \frac{2\hat{W} U_0 U(r)}{r} + \frac{U(r)^2}{r} \right]$$

$$= -\frac{1}{\rho} \left(\frac{\partial P}{\partial r} \right) + v \left(\frac{r_0 V_{r0} U_0}{r} \right) \left(\frac{4(n+1)}{b^2} \right)$$

$$-\frac{2(n+1)(V_{r0} U_0)^2}{r_0} \frac{1}{\xi^3} - \left[\frac{2(n+1)(\hat{W} U_0)^2}{2n+1} \frac{1}{r_0} + \frac{2\hat{W} U_0 U(r)}{r_0} + \frac{U(r)^2}{r_0} \right] \frac{1}{\xi}$$

$$= -\frac{1}{r_0 \rho} \left(\frac{\partial P}{\partial \xi} \right) + v \left(\frac{V_{r0} U_0}{\xi} \right) \left(\frac{4(n+1)}{b^2} \right)$$

$$\frac{1}{\rho} \left(\frac{\partial P}{\partial \xi} \right) = v \left(\frac{r_0 V_{r0} U_0}{\xi} \right) \left(\frac{4(n+1)}{b^2} \right) + \frac{2(n+1)}{2n+1} \left[\frac{(V_{r0} U_0)^2}{\xi^3} \right]$$

$$+ \left[\frac{2(n+1)(\hat{W} U_0)^2}{2n+1} + 2\hat{W} U_0 U(r) + U(r)^2 \right] \frac{1}{\xi}$$

$$\frac{1}{\rho} \left(\frac{\partial P}{\partial \xi} \right) = v \left(\frac{r_0 V_{r0} U_0}{\xi} \right) \left(\frac{4(n+1)}{b^2} \right) + \frac{2(n+1)}{2n+1} \left[\frac{(V_{r0} U_0)^2}{\xi^3} \right]$$

$$+ \left[\frac{2(n+1)(\hat{W} U_0)^2}{2n+1} + 2\hat{W} U_0^2 \xi + U_0^2 \xi^2 \right] \frac{1}{\xi}$$



$$\frac{U_0^2}{2} \left(\frac{\partial \hat{P}}{\partial \xi} \right) = \frac{2(n+1)}{2n+1} \left[\frac{(V_{r0}U_0)^2}{\xi^3} + \frac{(\hat{W}U_0)^2}{\xi} \right] + 2\hat{W}U_0^2 + U_0^2\xi + v \left(\frac{r_0V_{r0}U_0}{\xi} \right) \left(\frac{4(n+1)}{b^2} \right)$$

$$\frac{\partial \hat{P}}{\partial \xi} = \frac{4(n+1)}{(2n+1)\xi^3} [V_{r0}^2 + \xi^2\hat{W}^2] + 4\hat{W} + 2\xi + v \left(\frac{r_0V_{r0}}{\xi U_0} \right) \left(\frac{8(n+1)}{b^2} \right)$$

$$\frac{\partial \hat{P}}{\partial \xi} = \frac{4(n+1)}{(2n+1)\xi^3} [V_{r0}^2 + \xi^2\hat{W}^2] + 4\hat{W} + 2\xi + \left(\frac{1}{4V_{r0}} \right) \left(\frac{vr_0}{b^2U_0} \right) \left(\frac{32(n+1)V_{r0}^2}{\xi} \right)$$

$$\frac{\partial \hat{P}}{\partial \xi} = \frac{4(n+1)}{(2n+1)\xi^3} [V_{r0}^2 + \xi^2\hat{W}^2] + 4\hat{W} + 2\xi + \left(\frac{32(n+1)V_{r0}^2}{Re_m^*\xi} \right)$$

Power Generated Equation

From the definition of torque per rotor disc surface:

$$T = 2\pi \int_{r_i}^{r_0} \tau_w r^2 dr$$

$$T = 2\pi \int_{r_i}^{r_0} \left(\frac{2\mu(n+1)\bar{v}_\theta}{b} \right) r^2 dr$$

$$T = 2\pi \int_{\xi_i=1}^{\xi_0=1} \left(\frac{2\mu(n+1)\bar{v}_\theta}{b} \right) (r_0\xi)^2 r_0 d\xi$$

$$T = \left(\frac{4\pi\mu r_0^3(n+1)}{b} \right) \int_{\xi_i}^1 \bar{v}_\theta \xi^2 d\xi$$

$$T = \left(\frac{4\pi U_0 \mu r_0^3(n+1)}{b} \right) \int_{\xi_i}^1 \hat{W} \xi^2 d\xi$$

Mechanical Efficiency

$$\eta_{rm} = \frac{v_{\theta 0}U_0 - v_{\theta i}U_i}{v_{\theta 0}U_0} = 1 - \frac{(\bar{v}_{\theta i} + U_i)U_i}{(\bar{v}_{\theta 0} + U_0)U_0} = 1 - \frac{(\hat{W}_i + \xi_i)\xi_i}{(\hat{W}_0 + 1)}$$

Ideal Efficiency

$$\eta_i = \frac{v_{\theta 0}U_0 - v_{\theta i}U_i}{\Delta h_{isen}} = \frac{U_0^2(\hat{W}_0 + 1) - U_i(\hat{W}_i U_0 + U_i)}{\Delta h_{isen}}$$

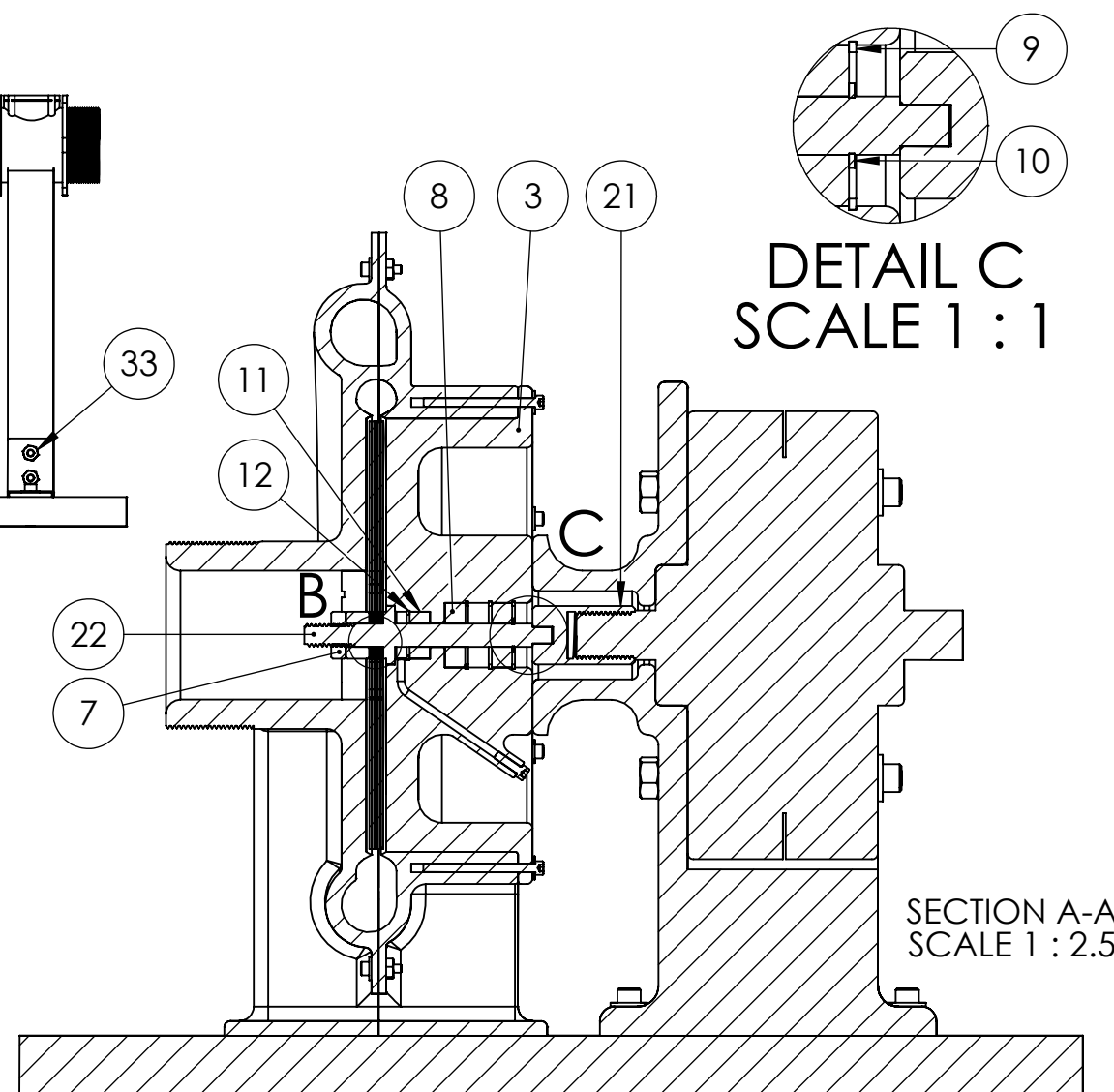
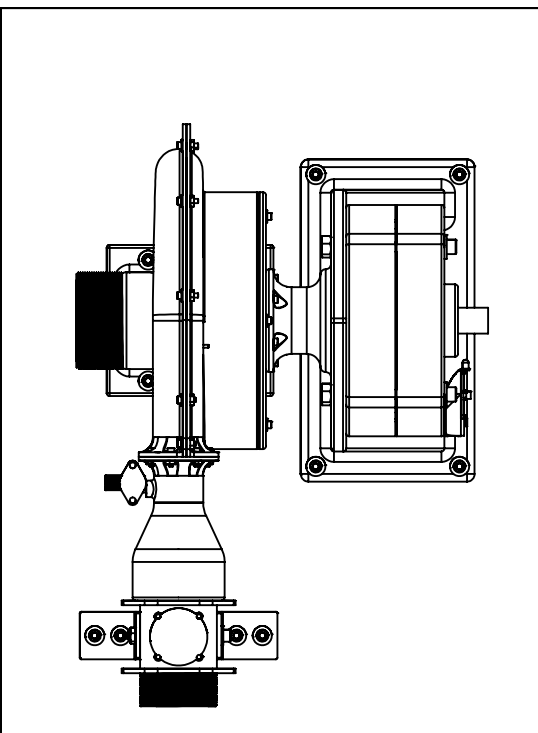
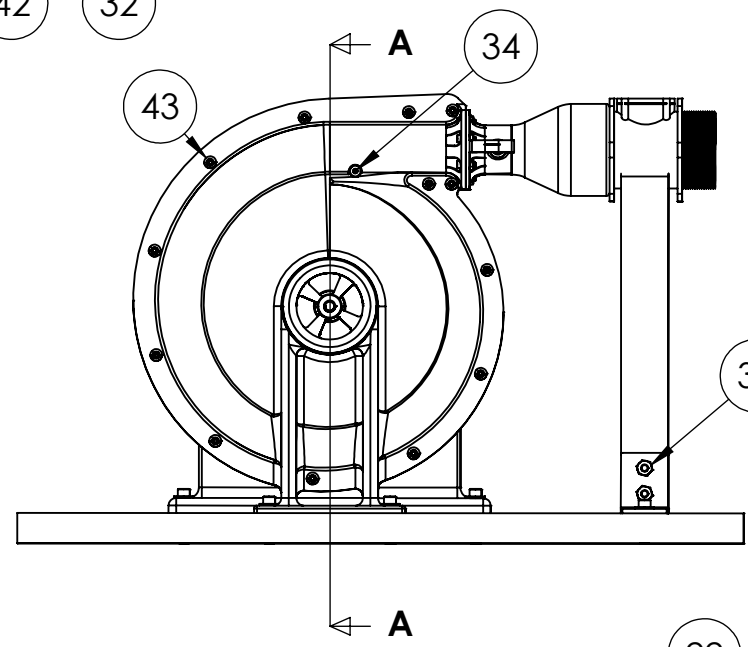
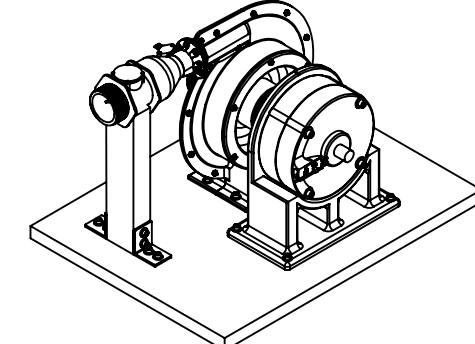
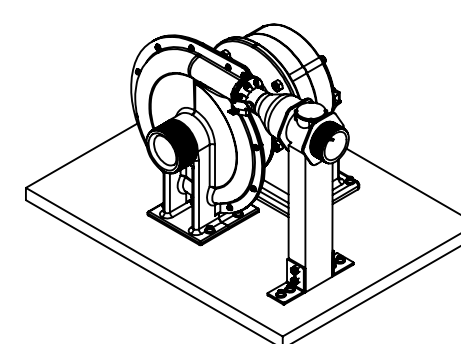
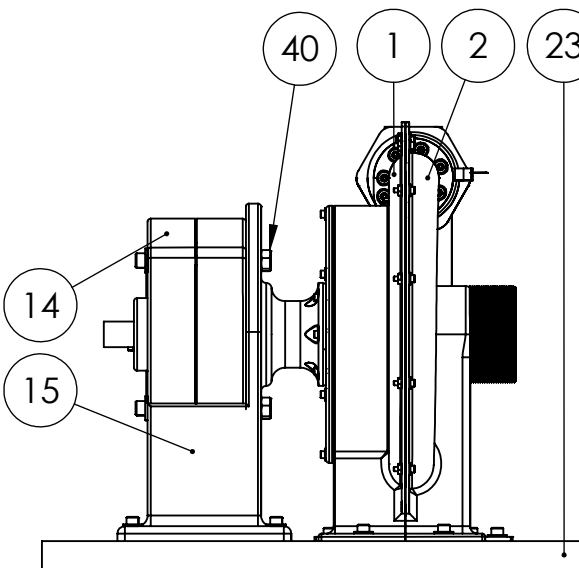
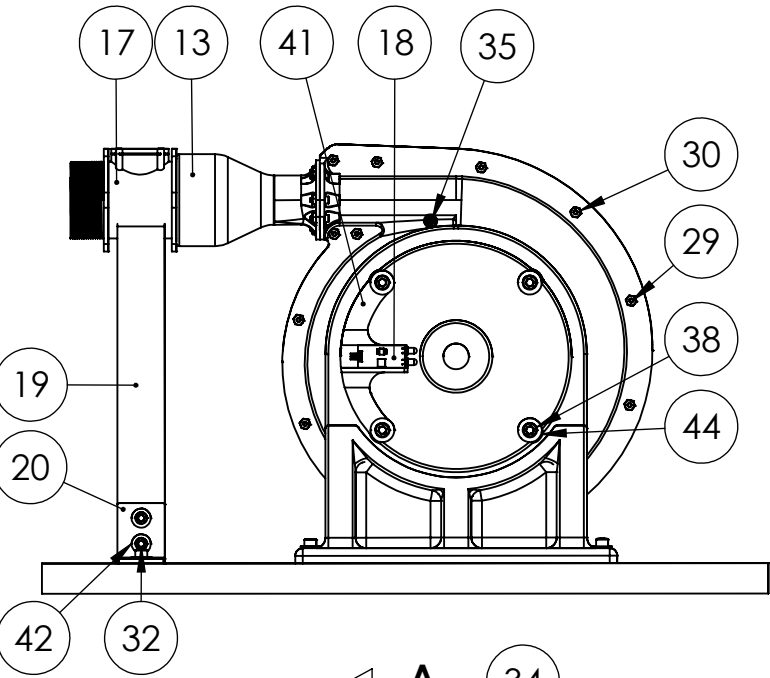
$$= \frac{(\hat{W}_0 + 1) - \xi_i(\hat{W}_i + \xi_i)}{\frac{\Delta h_{isen}}{U_0^2}}$$

A.7 Production and Commercialisation

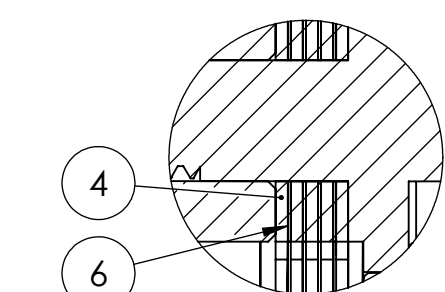
Table A7.1 Material primary production embodied energy values and corresponding sources [108].

Titanium	471	ICE, Titanium, general
Zinc	52	Ecoinvent, index #1156 zinc, primary, at regional storage

Material	Embodied Energy Value (MJ/kg)	Source
Aluminum Alloy	72	Ecoinvent, index #1045, aluminium alloy, AlMg3, at plant
Cast Aluminum	51	Ecoinvent, index #1057, aluminium, production mix, cast alloy, at plant
Cast Iron	25	ICE, Iron, General
Copper	34	Ecoinvent, index #1074, copper, at regional storage
Epoxies	133.5	Ashby, mean value, 127 and 140
Ferromanganese (Fe-Mn)	23	Ecoinvent, index #1097, ferromanganese, high-coal, 74.5% Mn, at regional storage
Ferrosilicon (Fe-Si)	15.88	Composite. 45% - Ecoinvent, index #321, silicon carbide, at plant. 55% - Ecoinvent, index #1132, pig iron, at plant.
Lead	16	Ecoinvent, index #1103 lead, at regional storage
Low Alloy Steel	28	Ecoinvent, index #1154, steel, low-alloyed, at plant
Low Carbon Steel	25	ICE, General Steel, World typical-world 39% recycled
Molybdenum	151	Ecoinvent, index #1116 molybdenum, at regional storage
Nickel	142	Recycled production mix. 74% Ecoinvent, index #1121 nickel, 99.5%, at plant. 26% Ecoinvent, index #8149 nickel, secondary, from electronic and electric scrap recycling, at refinery.
PCB, General	12,101	Ecoinvent
Stainless Steel	68	Ecoinvent, index #1152 steel, electric, chromium steel 18/8, at plant
Steel, 4140	33.5	Composite. 99% Ecoinvent, index #1154, steel, low-alloyed, at plant. 1% Ecoinvent, index #1073, chromium, at regional storage.
Steel, Bar & Rod	22	ICE, Bar & Rod - World typical 39%
Tin	321	Ecoinvent, index #1155 tin, at regional storage

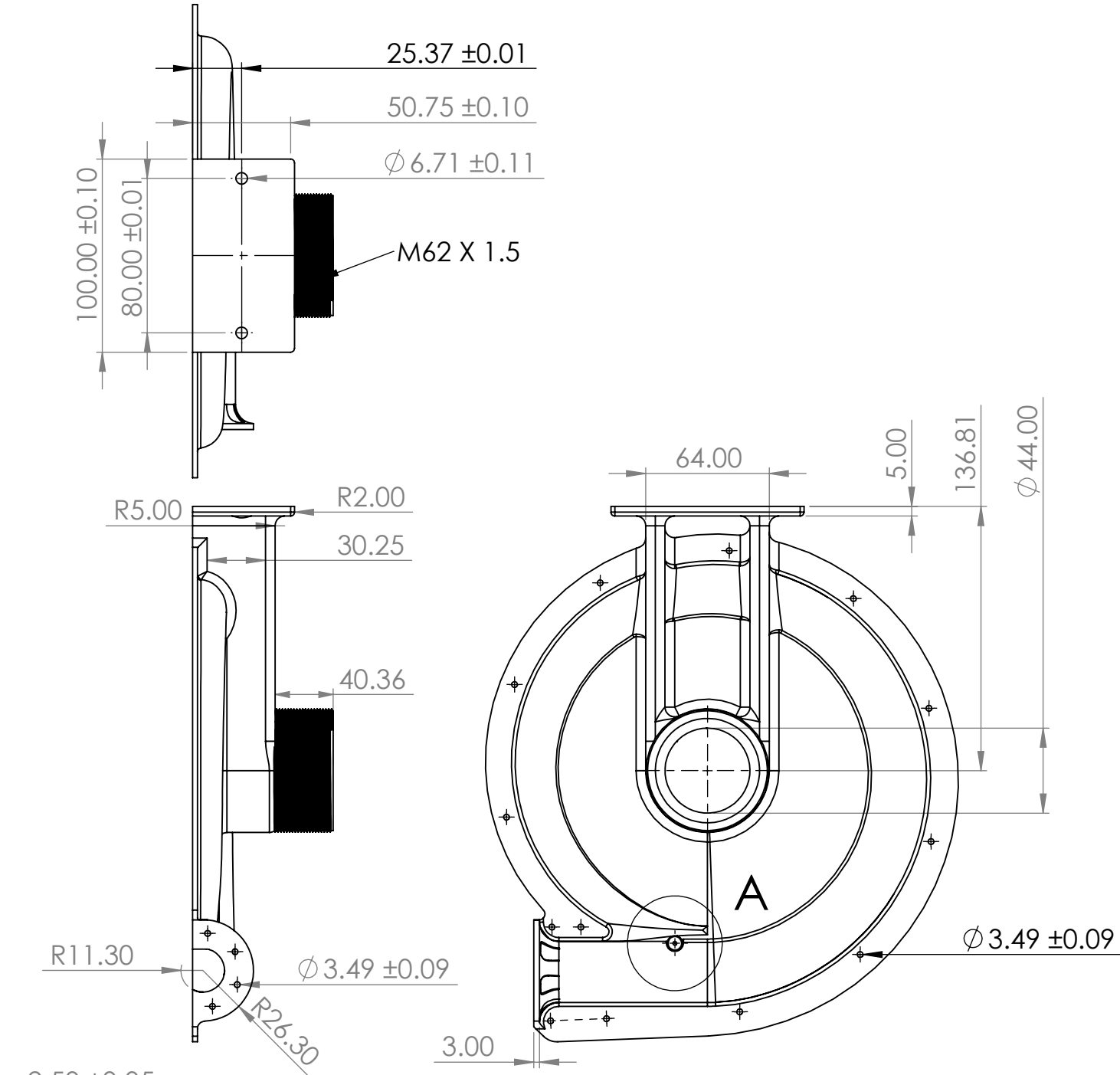
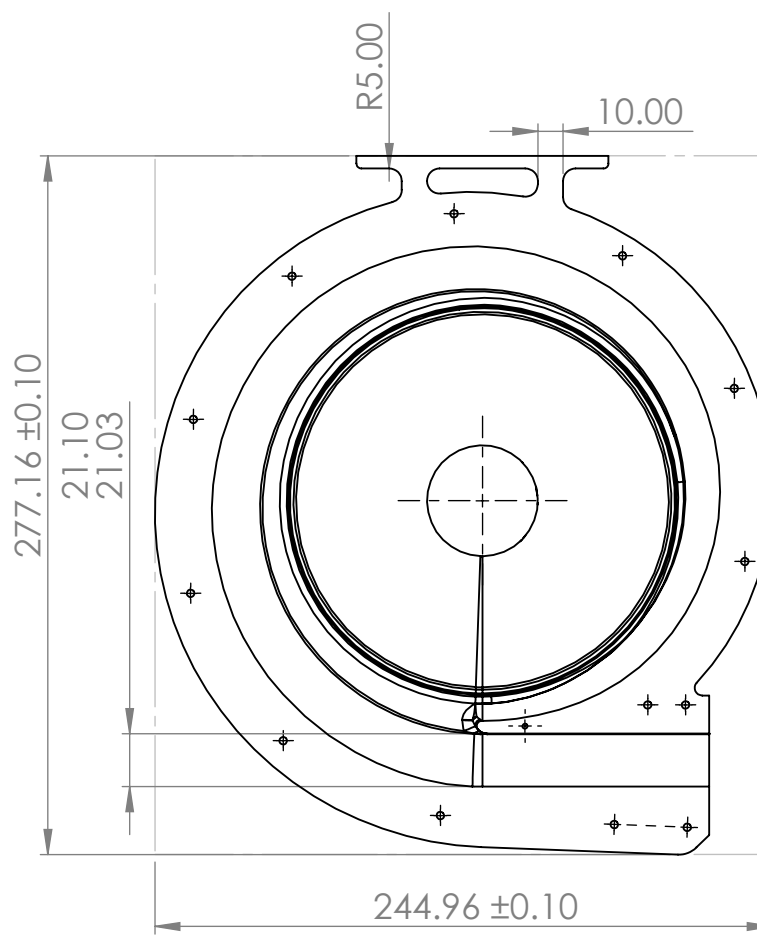


**DETAIL B
SCALE 2 : 1**



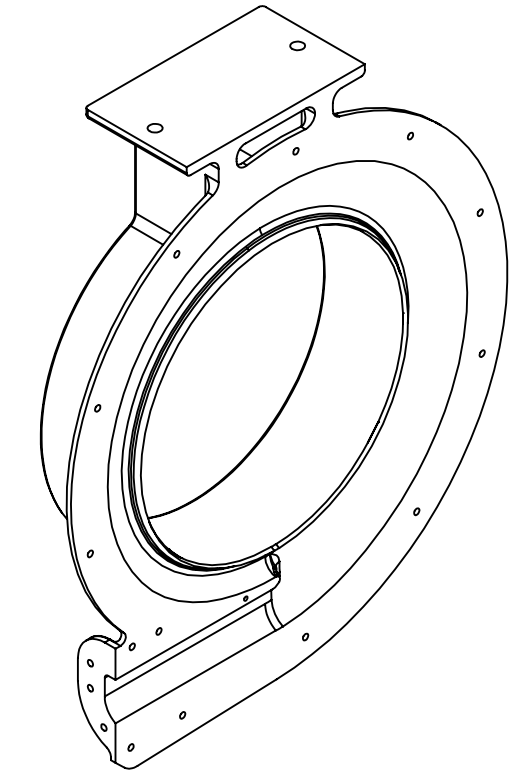
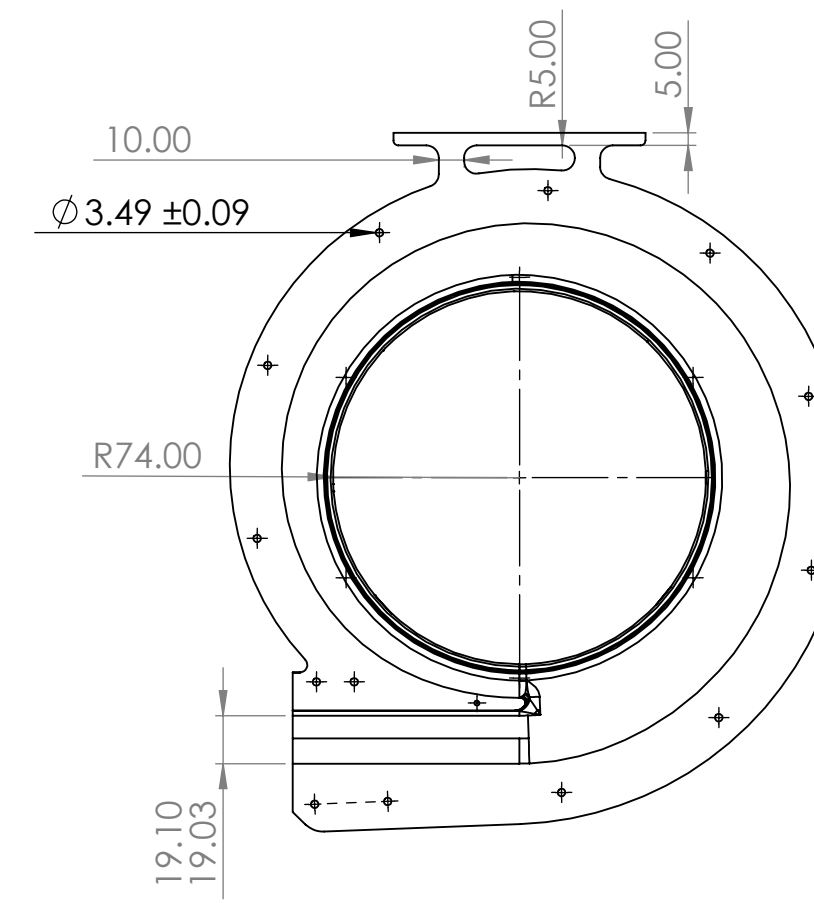
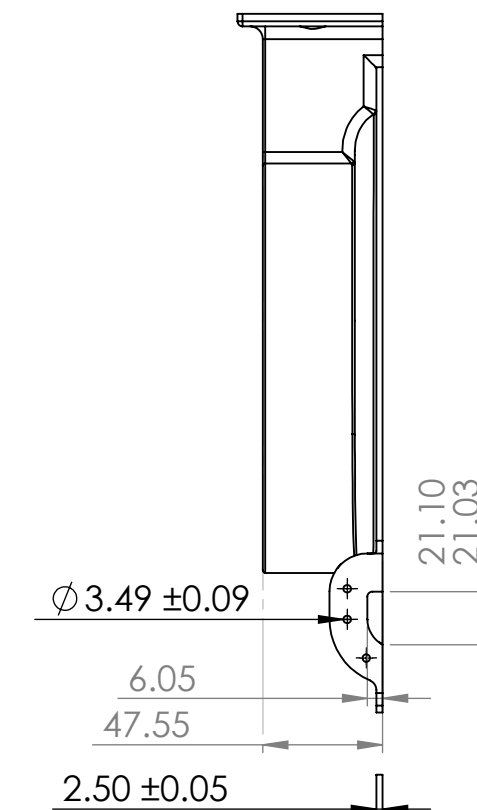
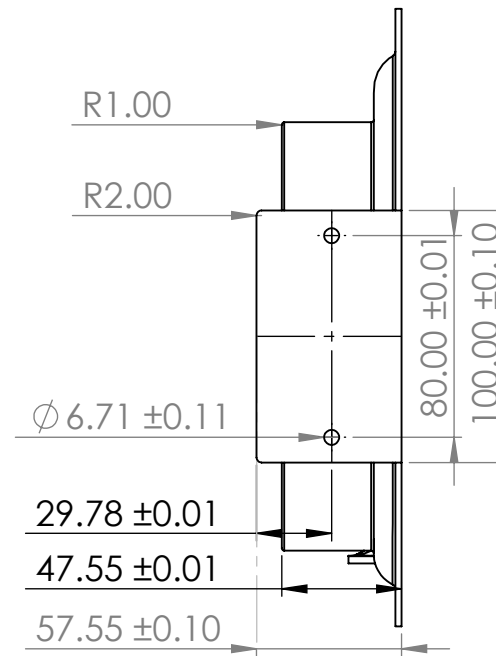
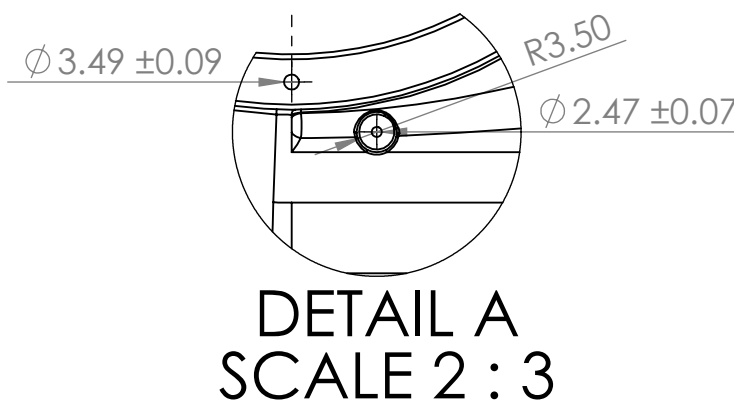
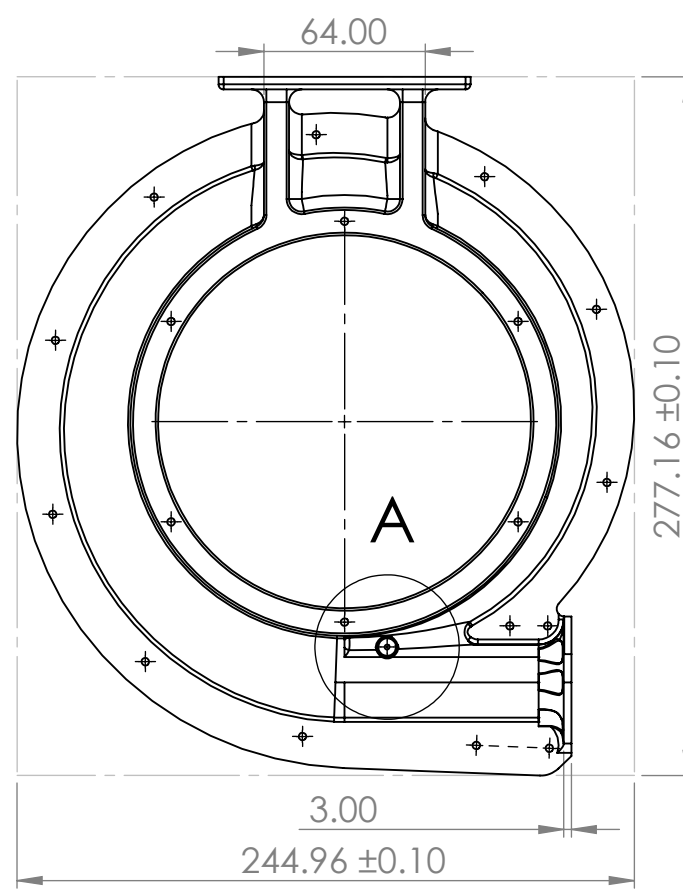
NO	PART NO	Description	ITEM NO	Remark	Quantity
1	GDP_45_T1	Turbine Front Casing	2	Additive	1
2	GDP_45_T2	Turbine Rear Casing	1	Additive	1
3	GDP_45_SCOV	Shaft Cover	3	Additive	1
4	GDP_45_AB	Alternator Base	15	Additive	1
5	GDP_45_SH	Shaft	22	Subtractive	1
6	GDP_45_D1,2,3,4,5	Discs	4	Subtractive	5
7	GDP_45_S1,2,3,4	Spacers	6	Subtractive	4
8	GDP_45_TR	Threaded Ring	7	Subtractive	1
9	GDP_45_SCA	Shaft Cap	5	Additive	1
10	GDP_45_SCON	Shaft Connector	21	Subtractive	1
11	GDP_45_AD	Adapter	13	Additive	1
12	GDP_45_TE	Tacho Extension	41	Additive	1
13	GDP_45_P	Main Platform	23	Subtractive	1
14	GDP_45_SU	Support	19	Subtractive	1
15		Alternator	14	Purchase	1
16		Tachometer	18	Purchase	1
17		Flowmeter	17	Purchase	1
18		Pressure Sensor	16	Purchase	1
19		L-brackets	20	Purchase	2
20		Rubber Lip Seal	11	Purchase	1
21		Circlip (S)	10	Purchase	1
22		Circlip (M)	12	Purchase	1
23		Circlip (L)	9	Purchase	3
24		Bearings	8	Purchase	2
25		M6 20mm Bolt	32		14
26		M6 Nut	33		2
27		M6 Washer	42		14
28		Alternator Bolt	38	Given	4
29		M5 Nut	40		4
30		M5 Washer	44		4
31		M3 10mm Bolt	29		32
32		M3 Nut	30		20
33		M3 Washer	43		19
34		M2 3mm Bolt	34		1
35		M2 Nut	35		1

DO NOT SCALE		DRAWN BY Frederick. W		TOLERANCES UNLESS OTHERWISE STATED	
A3		DESIGNED BY Frederick. W	LINEAR DIMENSIONS X = +/- 0.5mm XX = +/- 0.25mm XXX = +/- 0.1mm		
EDMC JOB No	DEPARTMENT Engineering	DATE 2/3/21	SCALE 1:5	ANGULAR DIMENSIONS X = +/- 0.5mm XX = +/- 0.25mm XXX = +/- 0.1mm ALL DIMENSIONS IN mm UNLESS OTHERWISE STATED	
PROJECT Tesla Turbine	SUPERVISOR Dr. Davide. L	MATERIAL Check Indi. Drawings	TEXTURE -	SURFACE FINISH ALL OVER UNLESS OTHERWISE STATED	
REMOVE ALL SHARP EDGES		THE INFORMATION CONTAINED IN THIS DOCUMENT IS THE PROPERTY OF THE UNIVERSITY OF SOUTHAMPTON DO NOT COPY WITHOUT WRITTEN PERMISSION.			
IF IN DOUBT PLEASE ASK		SHEET 1 of 15		No OFF 1	ASSEMBLY NUMBER ASS
				DRAWING NUMBER GDP_45_TTA	REVISION

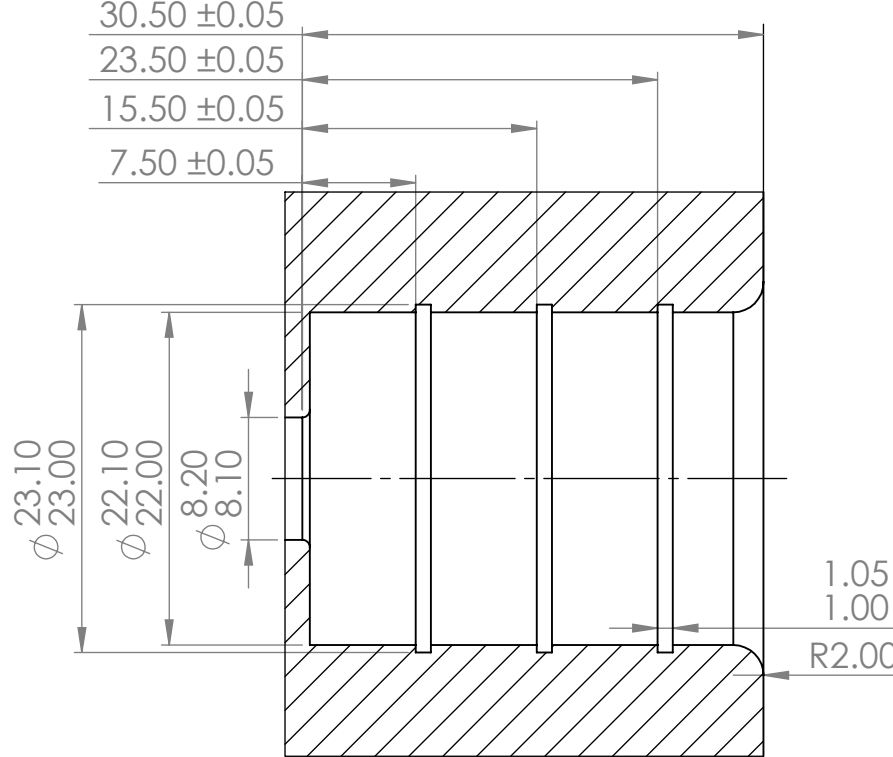


DETAIL A
SCALE 2 : 3

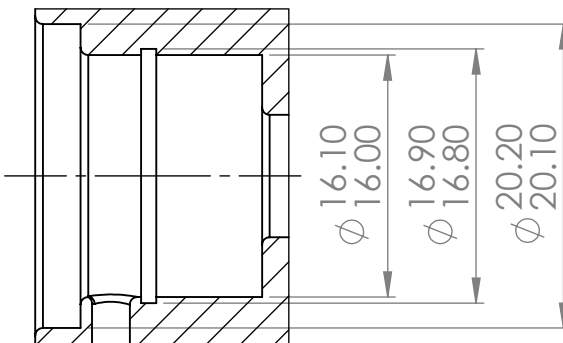
DO NOT SCALE A3		DRAWN BY Frederick. W		TOLERANCES UNLESS OTHERWISE STATED		UNIVERSITY OF Southampton Faculty of Engineering and the Environment TITLE Turbine Front Casing
EDMC JOB No	DEPARTMENT Engineering	DESIGNED BY Frederick. W	LINEAR DIMENSIONS	X = +/- 0.5mm XX = +/- 0.25mm XXX = +/- 0.1mm		
PROJECT Tesla Turbine	SUPERVISOR Dr. Davide. L	DATE 2/3/21	SCALE 1:3	ANGULAR DIMENSIONS X = +/- 0.5mm XX = +/- 0.25mm XXX = +/- 0.1mm ALL DIMENSIONS IN mm UNLESS OTHERWISE STATED		
MATERIAL ABS	TEXTURE -	SURFACE FINISH	<input checked="" type="checkbox"/> ALL OVER UNLESS OTHERWISE STATED			
REMOVE ALL SHARP EDGES	IF IN DOUBT PLEASE ASK	THE INFORMATION CONTAINED IN THIS DOCUMENT IS THE PROPERTY OF THE UNIVERSITY OF SOUTHAMPTON DO NOT COPY WITHOUT WRITTEN PERMISSION.	SHEET 1 of 15	No OFF 1	ASSEMBLY NUMBER 1	DRAWING NUMBER GDP_45_T1



DO NOT SCALE		DRAWN BY Frederick. W		TOLERANCES UNLESS OTHERWISE STATED		UNIVERSITY OF Southampton Faculty of Engineering and the Environment
A3		DESIGNED BY Frederick. W		LINEAR DIMENSIONS		
EDMC JOB No	DEPARTMENT Engineering	DATE 2/3/21	SCALE 1:3	X = +/- 0.5mm XX = +/- 0.25mm XXX = +/- 0.1mm		ANGULAR DIMENSIONS X = +/- 0.5mm XX = +/- 0.25mm XXX = +/- 0.1mm
PROJECT Tesla Turbine	SUPERVISOR Dr. Davide. L	MATERIAL ABS	TEXTURE -	SURFACE FINISH ALL OVER UNLESS OTHERWISE STATED		ALL OVER UNLESS OTHERWISE STATED
REMOVE ALL SHARP EDGES		THE INFORMATION CONTAINED IN THIS DOCUMENT IS THE PROPERTY OF THE UNIVERSITY OF SOUTHAMPTON DO NOT COPY WITHOUT WRITTEN PERMISSION.				
IF IN DOUBT PLEASE ASK						
SHEET 1 of 15		No OFF 1	ASSEMBLY NUMBER 2	DRAWING NUMBER GDP_45_T2	REVISION	

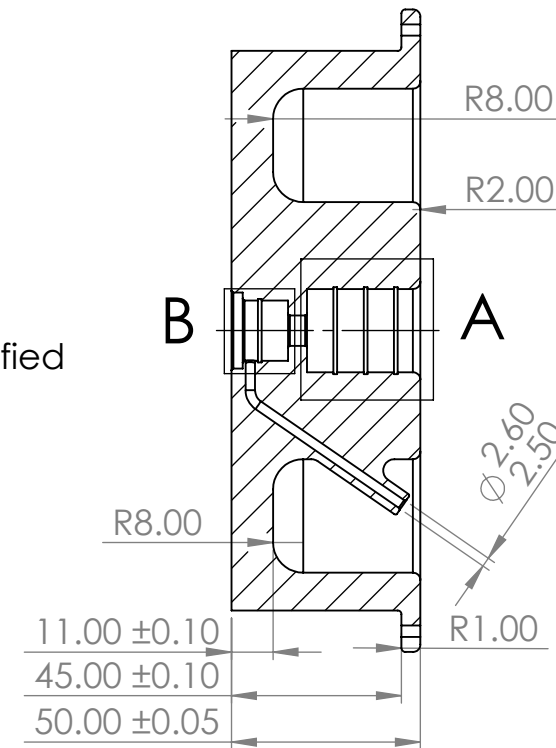


DETAIL A
SCALE 2 : 1

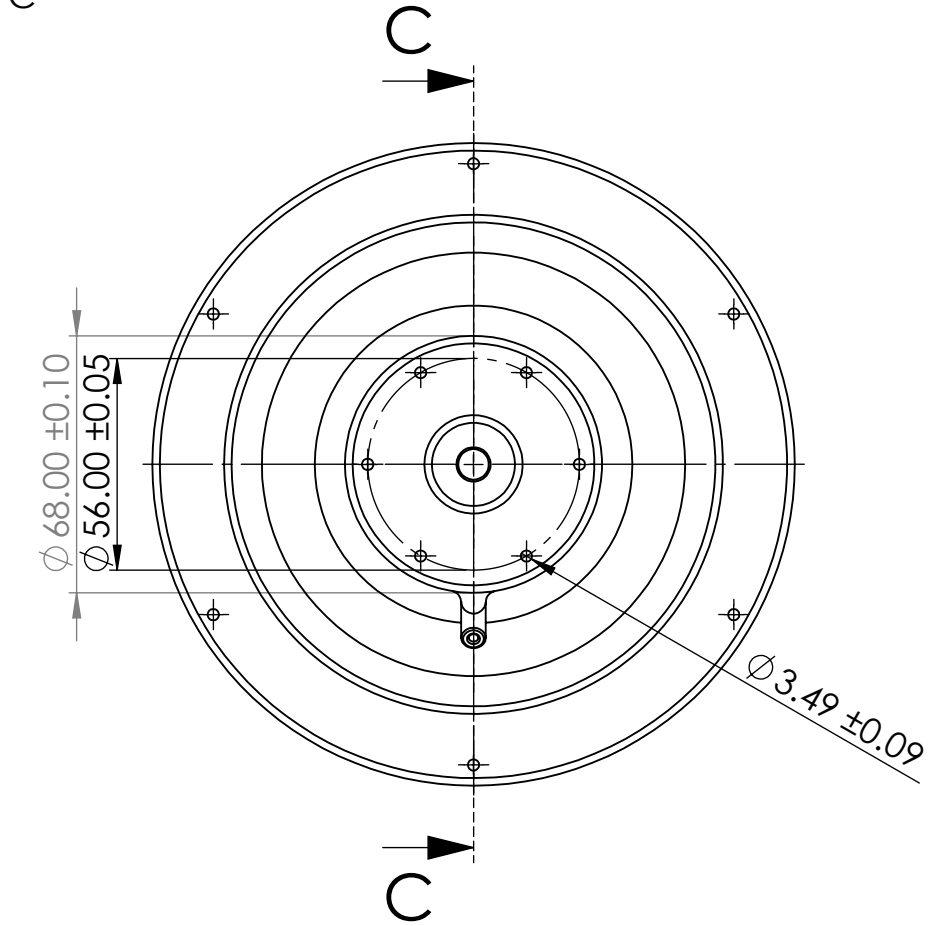
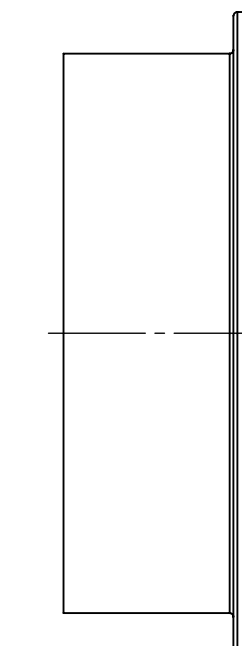
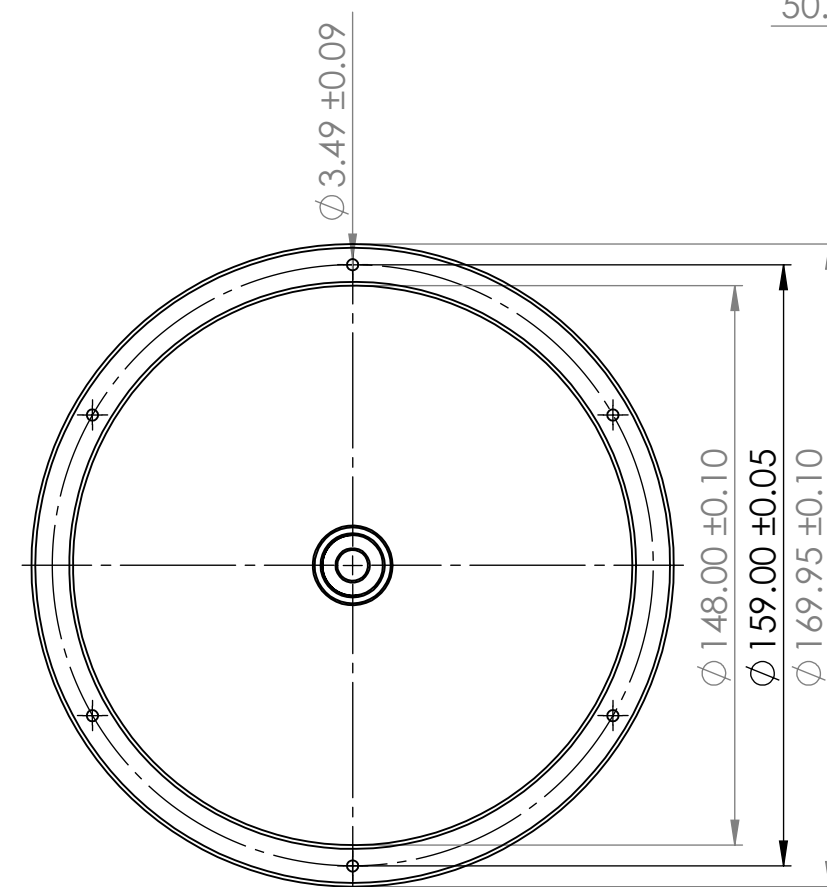


DETAIL B
SCALE 2 : 1

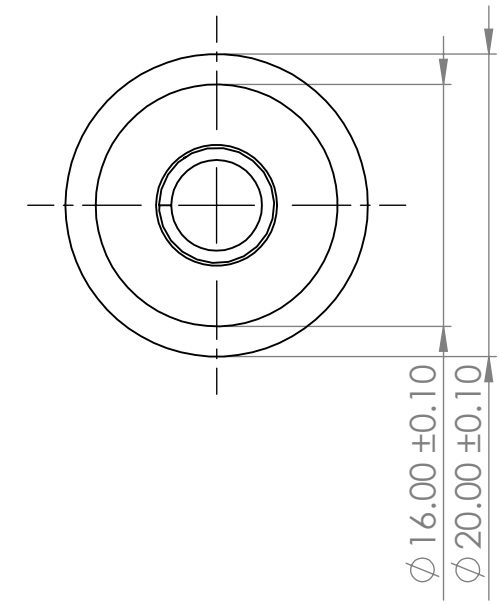
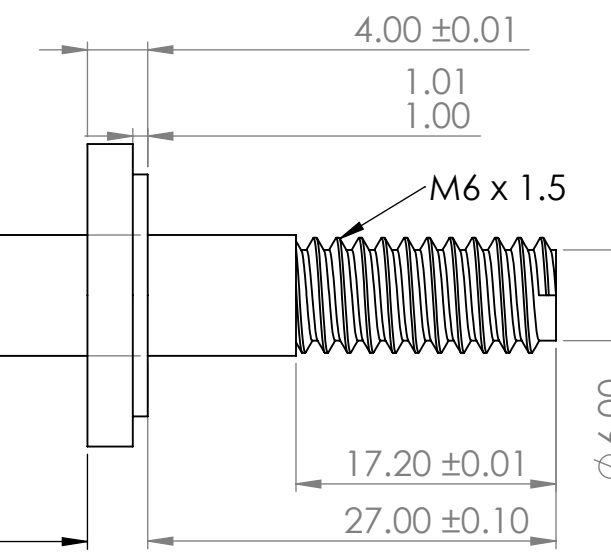
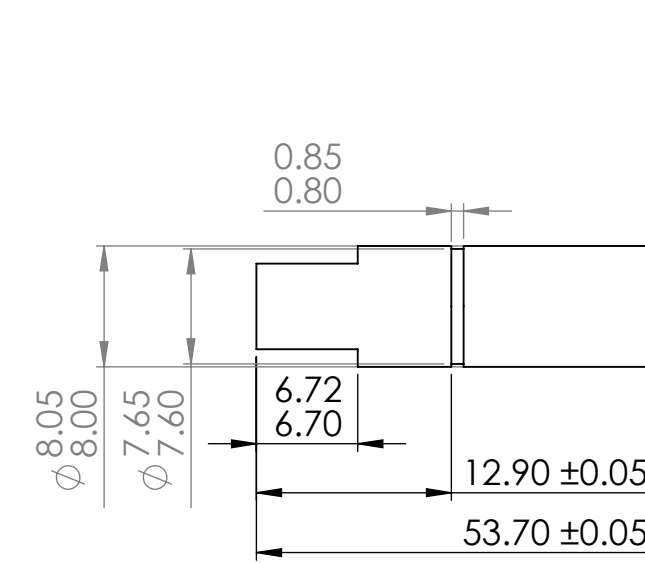
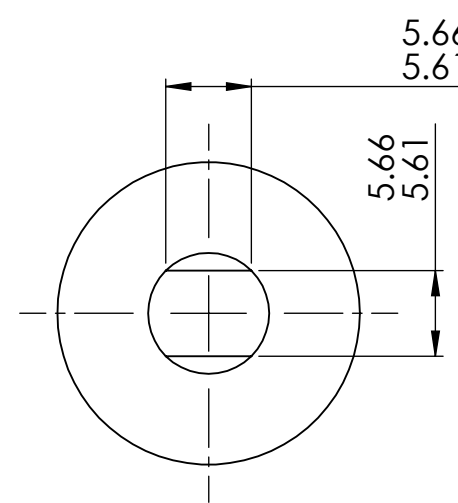
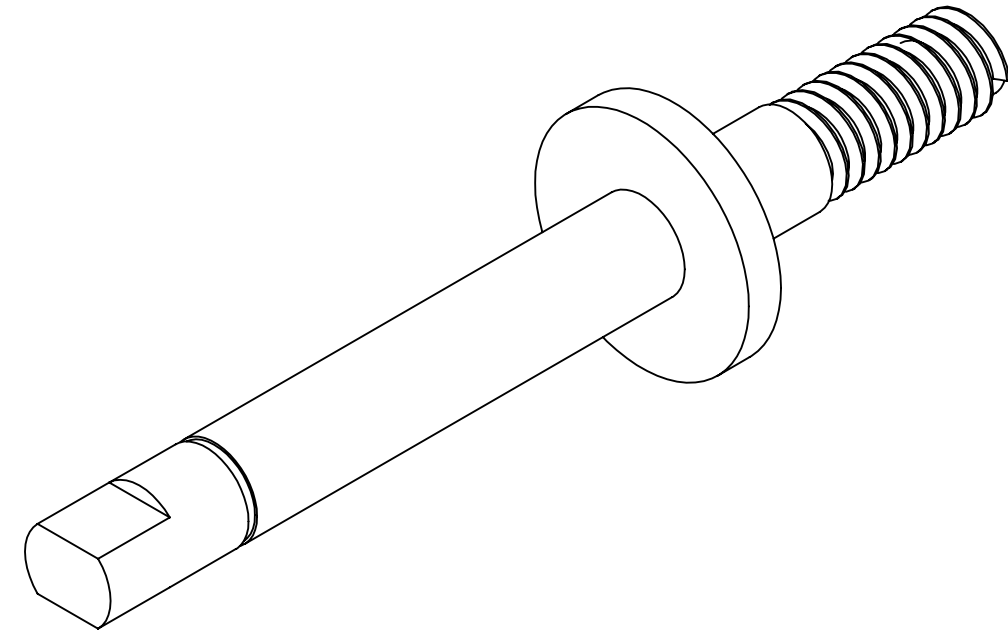
All fillets are of R0.5 unless specified
All grooves are of 1mm unless specified



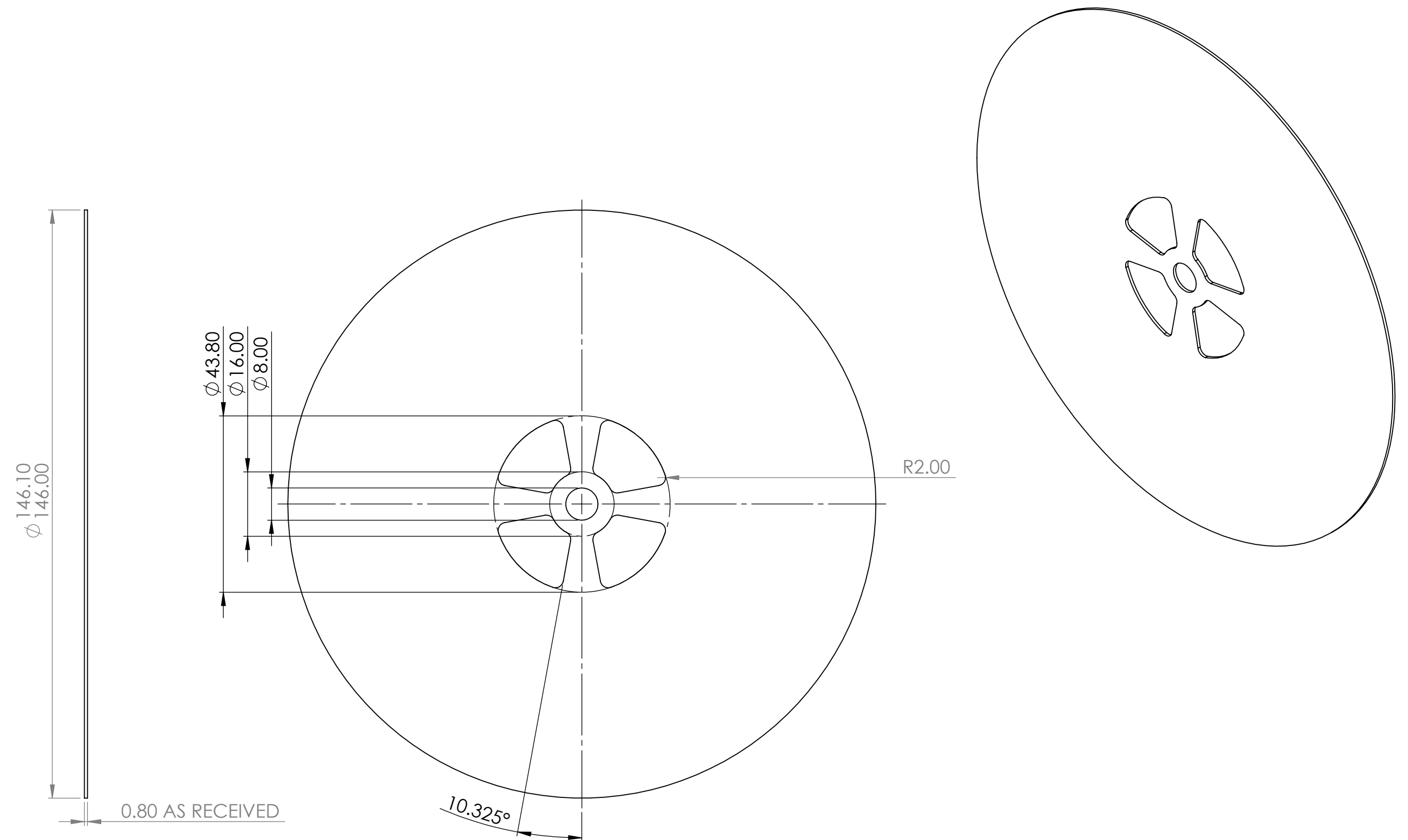
SECTION C-C



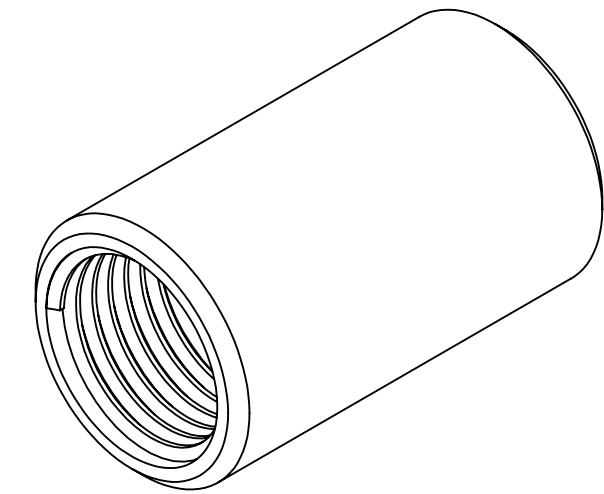
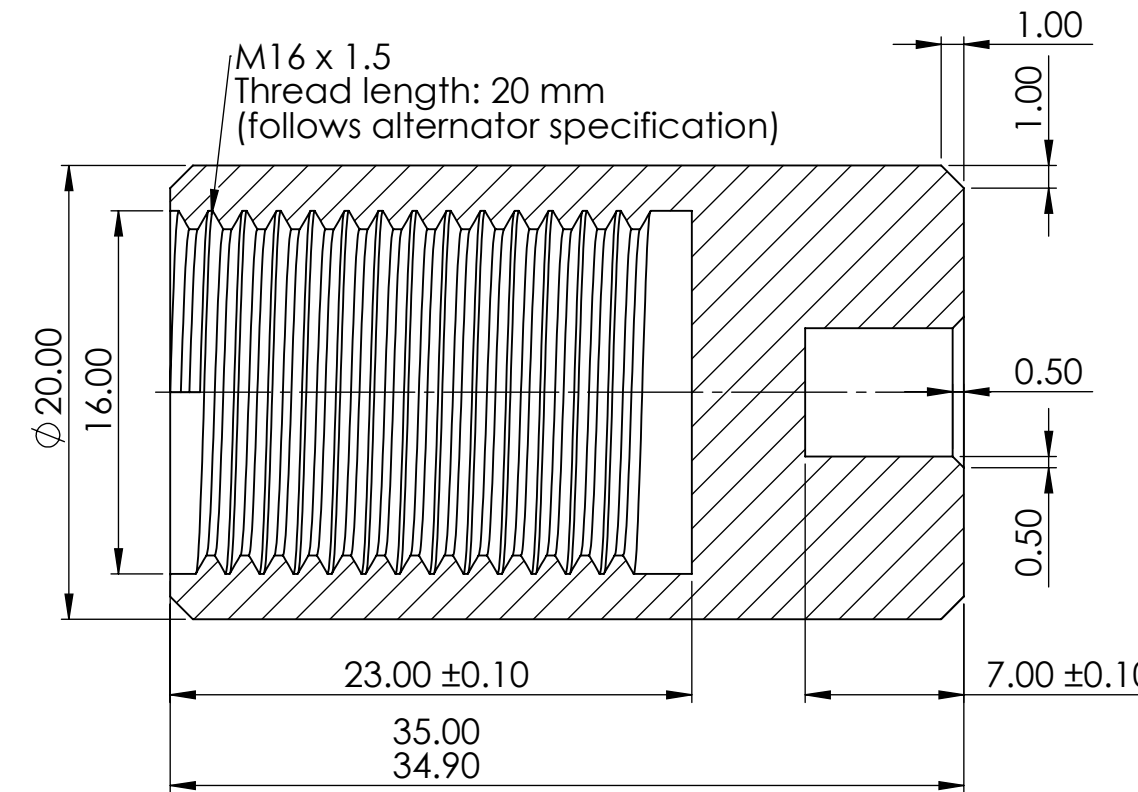
DO NOT SCALE		DRAWN BY Frederick. W		TOLERANCES UNLESS OTHERWISE STATED		UNIVERSITY OF Southampton Faculty of Engineering and the Environment
A3		DESIGNED BY Frederick. W	LINEAR DIMENSIONS	ANGULAR DIMENSIONS	TITLE	
EDMC JOB NO	DEPARTMENT Engineering	DATE 2/3/21	SCALE 1:2	X = +/- 0.5mm XX = +/- 0.25mm XXX = +/- 0.1mm	Shaft Cover	
PROJECT Tesla Turbine	SUPERVISOR Dr. Davide. L	MATERIAL Composite Powders	TEXTURE -	SURFACE FINISH ✓ ALL OVER UNLESS OTHERWISE STATED		
REMOVE ALL SHARP EDGES		THE INFORMATION CONTAINED IN THIS DOCUMENT IS THE PROPERTY OF THE UNIVERSITY OF SOUTHAMPTON DO NOT COPY WITHOUT WRITTEN PERMISSION.				
IF IN DOUBT PLEASE ASK						
SHEET 1 of 15		No OFF 1		ASSEMBLY NUMBER 3		DRAWING NUMBER GDP_45_SCON
REVISION						



DO NOT SCALE		DRAWN BY Frederick. W		TOLERANCES UNLESS OTHERWISE STATED		UNIVERSITY OF Southampton Faculty of Engineering and the Environment
A3		DESIGNED BY Frederick. W		LINER DIMENSIONS X = +/- 0.5mm XX = +/- 0.25mm XXX = +/- 0.1mm		
EDMC JOB No	DEPARTMENT Engineering	DATE 2/3/21	SCALE 2:1	ANGULAR DIMENSIONS X = +/- 0.5mm XX = +/- 0.25mm XXX = +/- 0.1mm ALL DIMENSIONS IN mm UNLESS OTHERWISE STATED		
PROJECT Tesla Turbine	SUPERVISOR Dr. Davide. L	MATERIAL 316 Stainless Steel	TEXTURE -	SURFACE FINISH ✓ ALL OVER UNLESS OTHERWISE STATED		
REMOVE ALL SHARP EDGES		THE INFORMATION CONTAINED IN THIS DOCUMENT IS THE PROPERTY OF THE UNIVERSITY OF SOUTHAMPTON DO NOT COPY WITHOUT WRITTEN PERMISSION.				
IF IN DOUBT PLEASE ASK		SHEET 1 of 15	No OFF 1	ASSEMBLY NUMBER 20	DRAWING NUMBER GDP_45_SH	REVISION

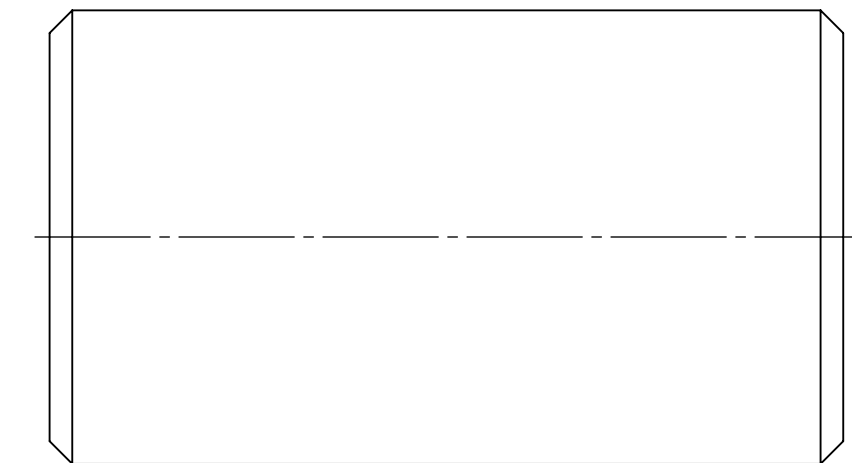
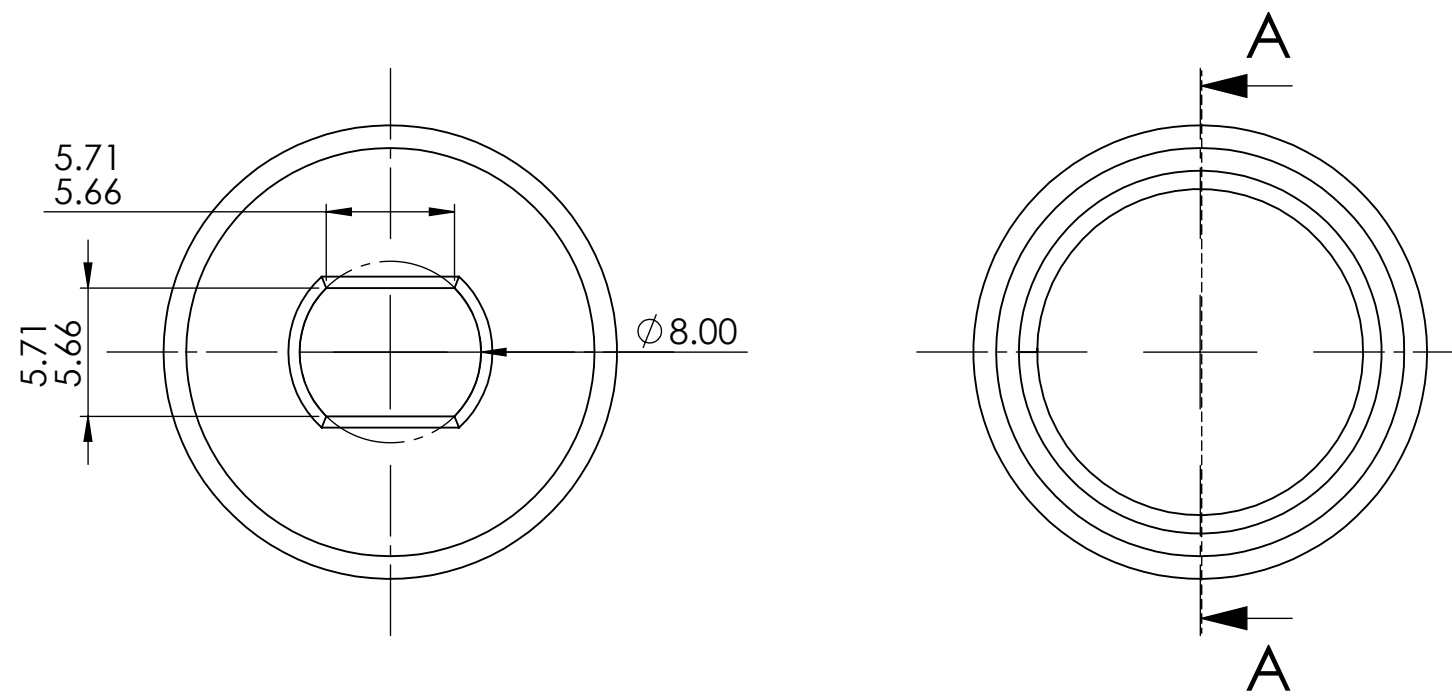


DO NOT SCALE		DRAWN BY Frederick. W		TOLERANCES UNLESS OTHERWISE STATED		UNIVERSITY OF Southampton Faculty of Engineering and the Environment
A3		DESIGNED BY Frederick. W		LINER DIMENSIONS		
EDMC JOB No	DEPARTMENT Engineering	DATE 2/3/21	SCALE 1:1	X = +/- 0.5mm XX = +/- 0.25mm XXX = +/- 0.1mm		
PROJECT Tesla Turbine	SUPERVISOR Dr. Davide. L	MATERIAL 316 Stainless Steel	TEXTURE -	ANGULAR DIMENSIONS X = +/- 0.5mm XX = +/- 0.25mm XXX = +/- 0.1mm		
REMOVE ALL SHARP EDGES		THE INFORMATION CONTAINED IN THIS DOCUMENT IS THE PROPERTY OF THE UNIVERSITY OF SOUTHAMPTON DO NOT COPY WITHOUT WRITTEN PERMISSION.				TITLE Disc
IF IN DOUBT PLEASE ASK		SHEET 1 of 15	No OFF 5	ASSEMBLY NUMBER 4	DRAWING NUMBER GDP_45_D	REVISION



SECTION A-A

SCALE 3 : 1



DO NOT SCALE		DRAWN BY Frederick. W		TOLERANCES UNLESS OTHERWISE STATED		UNIVERSITY OF Southampton Faculty of Engineering and the Environment
A3		DESIGNED BY Frederick. W		LINER DIMENSIONS X = +/- 0.5mm XX = +/- 0.25mm XXX = +/- 0.1mm		
EDMC JOB No	DEPARTMENT Engineering	DATE 2/3/21	SCALE 3:1	ANGULAR DIMENSIONS X = +/- 0.5mm XX = +/- 0.25mm XXX = +/- 0.1mm	ALL DIMENSIONS IN mm UNLESS OTHERWISE STATED	
PROJECT Tesla Turbine	SUPERVISOR Dr. Davide. L	MATERIAL 316 Stainless Steel	TEXTURE -	SURFACE FINISH ✓ ALL OVER UNLESS OTHERWISE STATED		
REMOVE ALL SHARP EDGES		THE INFORMATION CONTAINED IN THIS DOCUMENT IS THE PROPERTY OF THE UNIVERSITY OF SOUTHAMPTON DO NOT COPY WITHOUT WRITTEN PERMISSION.				
IF IN DOUBT PLEASE ASK		SHEET 1 of 15	No OFF 1	ASSEMBLY NUMBER 19	DRAWING NUMBER GDP_45_SCON	REVISION